FACTORS INFLUENCING HORIZONTAL CRACKING IN CONTINUOUSLY

REINFORCED CONCRETE PAVEMENTS (CRCP)

Elias K. Sudoi, HND., B.S.

Thesis Prepared for the Degree of

MASTER OF SCIENCE

UNIVERSITY OF NORTH TEXAS

August 2008

APPROVED:

Seifollah Nasrazadani, Major Professor
Nourredine Boubekri, Committee Member
Cheng Yu, Committee Member
Mike Kozak, Program Coordinator
Nourredine Boubekri, Chair of the Department of
        Engineering Technology
Costas Tsatsoulis, Dean of the College of
        Engineering
Sandra L. Terrell, Dean of the Robert B. Toulouse
        School of Graduate Studies

Sudoi, Elias K. <u>Factors influencing horizontal cracking in continuously reinforced concrete pavements (CRCP).</u> Master of Science (Engineering Systems), August 2008, 124 pp, 40 tables, 53 figures, references, 48 titles.

This research presents the results on an experimental investigation to identify the significant factors influencing horizontal cracking in continuously reinforced concrete pavements (CRCP). An in-depth analysis of the microstructure, morphological characteristics of the interfacial transition zone (ITZ) and the observation of cracking using the environmental scanning electron microscope (ESEM) was done. Characterization of oxides using Fourier transform infrared spectroscopy (FTIR) and electron dispersive x-ray spectroscopy (EDS) was also performed. Water to cement ratio (w/c) and rebar temperature had a significant influence on the rebar-concrete bond strength. The 28-day shear strength measurements showed an increase in rebar-concrete bond strength as the water to cement ratio (w/c) was reduced from 0.50 to 0.40. There was a reduction in the peak pullout load as the temperature increased from 14^oF to 252^oF for the corroded and non-corroded rebar experiments. The corroded rebar pullout test results showed a 20-50 % reduction in bond strength compared to the non-corroded rebars. FTIR measurements indicated a presence of lepidocrocite (γ –FeOOH) and maghemite (γ –Fe_2O_3) on the ITZ. ESEM images showed the existence of microcracks as early as three days after casting with the bridging of these cracks between coarse aggregate locations in the interfacial zone propagating through the mortar.

ACKNOWLEDGEMENTS

It is with heartfelt gratitude that I would like to express my appreciation to my committee chair, Dr. Seifollah Nasrazadani for his guidance and support throughout my graduate program and in the completion of this thesis project. I would also like to thank my committee members Dr. Nourredine Boubekri, Dr. Cheng Yu and Mr. Abbas Mehdibeigi, P.E for their assistance, careful reading and the suggestions they provided at all levels of this thesis project.

To my family, thank you for your support and encouragement throughout my studies in America. Thank you for your patience, confidence and for believing in me, words cannot express how much you are appreciated. I must acknowledge my parents Dr. and Mrs. Vincent Sudoi for encouraging us as family to always shoot for the stars, for their constant moral, spiritual and financial support. Thank you and God bless you abundantly. To my siblings, Larry, Gilbert, Raymond, Allan, Sylvia and Georges, you guys are the greatest and I am blessed to have you share and experience this wonderful life that we have been blessed to have.

Finally yet importantly, I would like to thank all my dear friends whose names cannot fit this space for all their support and encouragement; it has been a bumpy and rough ride, we neither lost our faith nor focus and we are finally making it! On a personal note, I would also like to express my gratitude to Evelyn for her confidence and never ending support.

TABLE OF CONTENTS

LIST OF TABLES

LIST OF FIGURES

CHAPTER I

INTRODUCTION

The power and ageless strength of concrete cannot be underestimated, as it is one of the most durable compounds known to man. The dictionary meaning of concrete denotes a mixture of materials, pebbles, gravels and sand agglomerated by means of a hydraulic binder, cement, which sets only after being mixed with water, and imparts considerable hardness to the mixture. The forerunners of concrete pavements were the ones constructed by the Romans as early as the first century B.C. A binder consisting of '2 parts natural pozzolan and 1 part lime' was used to bind the stones of Roman pavements (Jeuffroy et al., 1996)

Today's use of concrete has taken many forms. It is one of the most widely used building materials in the world, a signature construction component in bridges, skyscrapers, superhighways, dams, houses and sidewalks. Portland cement is a required component in concrete mixes, which causes the concrete to act as an "artificial rock" protecting against fire in houses and public buildings. It also reduces damage caused by flooding compared to similar wooden structures. Concrete is also sound proof as is seen when used in the construction of high walls around buildings adjacent to roads to reduce the noise caused by traffic.

Significant technical and design developments in the construction of continuously reinforced concrete pavements (CRCP) has made concrete paving faster, less expensive, and more durable. Improved concrete placement and maintenance practices have been achieved due to continued research and development.

The need for concrete reinforcement arises because its tensile strength is only around one tenth of its compressive strength (Shah et al., 1995). The presence of continuous reinforcement makes it difficult for cracks to initiate and propagate. Distresses in CRCP has however been

observed in Texas, Illinois and Virginia due to horizontal cracking of the pavements (Kim and Won 2004). This does not only lead to the costly repairs of the roads but also results in the reduction of the useful life of the concrete pavements.

This research investigates the effect of using different water to cement (w/c) ratios (0.40, 0.45 and 0.50) and their influence on concrete bond strength. Rebar temperature effects at the pouring stage of concrete were studied using initial rebar temperatures of $14^{o}F$, $77^{o}F$ and $252^{o}F$. These temperatures allowed for the investigation of the rebar concrete bond strength. The microscopic study of the ITZ at the rebar-concrete interface was also done.

The effect of the rebar surface condition on the bond strength was studied by using corroded and non-corroded rebars. An in-depth analysis of the microstructure of ITZ and morphological characteristics of the concrete mix and steel rebar was also investigated facilitating the understanding of the microstructural factors responsible for horizontal cracking in CRCP.

Design and Construction of Rigid Pavements

The long-term performance of rigid pavement depends not only on proper pavement design and materials selection, but on good construction practices as well. The construction of a rigid pavement is a complex process involving many processes which include proper preparation of the subgrade and subbase, placing reinforcing bars or dowels, choice and handling of aggregates and other materials, development of concrete mix design, production and transport of the concrete, and placing, finishing, curing and joint sawing the concrete.

A rigid pavement structure is composed of a hydraulic cement concrete surface course, and underlying base and subbase courses (if used). Another term commonly used is Portland

cement concrete (PCC) pavement, although with today's pozzolanic additives, cements may no longer be technically classified as "Portland." The surface course (concrete slab) is the stiffest and provides the majority of strength. The base or subbase layers are orders of magnitude less stiff than the PCC surface but still make important contributions to pavement drainage, frost protection and provide a working platform for construction equipment. Rigid pavements are substantially 'stiffer' than flexible pavements due to the high modulus of elasticity of the PCC material resulting in very low deflections under loading. Rigid pavements can have reinforcing steel, which is generally used to handle thermal stresses to reduce or eliminate joints and maintain tight crack widths. Figure 1 shows a typical section for a rigid pavement (Pavement Design Guide 2006).
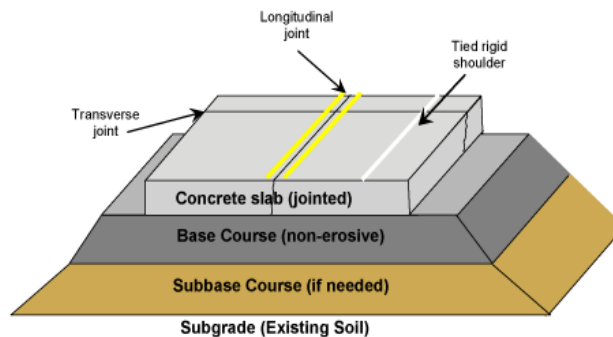
Figure 1. A typical section for a rigid pavement (Pavement Design Guide, 2006).

Continuously Reinforced Concrete Pavement (CRCP)

CRCP contains both longitudinal and transverse steel. CRCP does not contain transverse joints except at construction joints. The function of the longitudinal steel is not to strengthen the concrete slab, but to control concrete volume changes due to temperature and moisture variations and to keep transverse cracks tightly closed (Pavement Design Guide 2006). The function of the transverse steel is to keep longitudinal joints and cracks closed. If the steel serves its proper

function and keeps cracks from widening, aggregate interlock is preserved and concrete stresses in the concrete slab due to traffic loading are reduced.

The factors that influence the performance of CRCP include: (1) Portland cement concrete properties (tensile strength, elastic modulus, coefficient of thermal expansion and drying shrinkage); (2) slab and subbase resistance (vertical and horizontal stiffness); (3) steel properties (percent reinforcement, steel bar diameter and location); (4) environmental loads; (ambient air temperature, solar radiation, wind speed and relative humidity); (5) dimension and geometry of structure (pavement thickness and boundary conditions); (6) external wheel loads (static wheel load and moving dynamic load) (Jeong-Hee Nam, 2005). This study presents the factors that influence the horizontal cracking in CRCP; rebar temperature and its relationship with the concrete bond strength, influence of the water to cement ratio and the steel surface condition in terms of corroded vs. non-corroded rebar. Figure 2 shows a continuously reinforced concrete pavement under construction.

Figure 2. Continuously Reinforced Concrete Pavement (Pavement Design Guide, 2006).

Factors Affecting CRCP Behavior

Several factors influence the development of thermal stresses in CRCP. These include (1) the environmental conditions (ambient air temperature and solar radiations); (2) the thermal

properties of the concrete (heat of hydration and coefficient of thermal expansion); (3) the

conditions at placement; (4) dimension and geometry of the structure (Jeong-Hee Nam, 2005).

Expansion and contraction of the concrete structure during early-age heating and the

subsequent cooling occurs in unrestrained concrete. This does not normally lead to stress

development. This however is not the case in practice; the concrete structure is nearly always

restrained to some degree, either externally by adjoining structures or internally by different

temperature in the components of the structure itself. These imposed restraint conditions and

temperature changes induces compressive and/or tensile stresses in the concrete (Cha, 1999).

Effect of Heat of Hydration and Curing Temperature

Hydration of the fresh concrete is accompanied by the release of energy in the form of

heat, with the actual rate of release varying with time. A typical pattern of heat generation

during the hydration of tricalcium silicate, the major component of cement is shown in Figure 3

(Mindess et al., 1981).
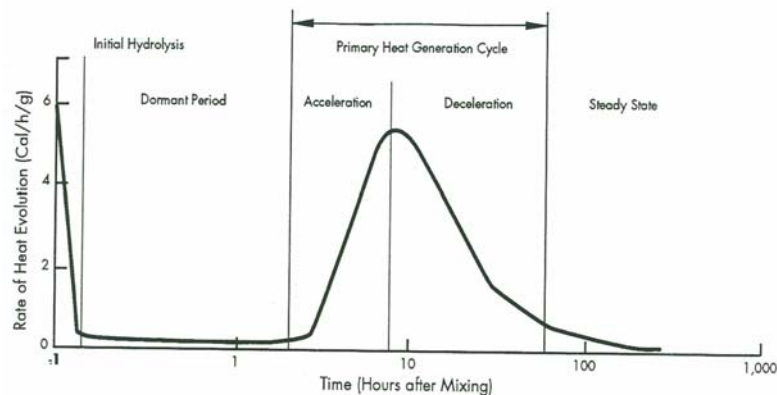
Figure 3. Typical pattern of heat generation during the hydration of tricalcium silicate (Mindess et al., 1981).

When Portland cement compounds are mixed with water, there is normally a rapid

release of heat. This reaction represents the heat of the solution of aluminates and sulfates and

ceases within about 15 minutes (Mehta, 1986). The primary heat generation cycle begins hours

after the cement compounds are mixed with water. Before this primary cycle, concrete is in a

plastic state and is relatively inactive chemically.

The peak of the primary cycle is reached several hours after concrete is mixed with water.

At this stage, the major hydration products crystallize from the solution of the mixture. This

stage includes the time of initial and/or final set of the concrete. As hydration products grow,

they form a barrier to the infiltration of additional water; the reaction slows and may eventually

stop when there is no room for further growth of crystals, or when hydration is theoretically

completed (Mindess et al., 1981). It should be noted that, because the reaction is chemically

controlled, the rate of hydration is chemically controlled.

The rate of hydration is very sensitive to temperature, especially during the primary cycle

(Mindess et al., 1981). Therefore, the temperature condition during construction is an important

factor affecting the rate of hydration. Figure 4 (Suh et al., 1992) shows the effect of curing

temperature on the hydration of tricalcium silicate. It can be seen that the higher the curing

temperature, the faster the heat release and the higher the peak.
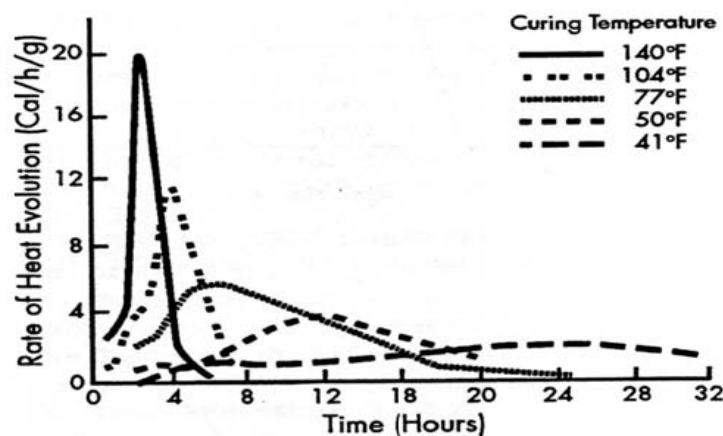
Figure 4. Effect of curing temperature on the hydration. (Suh et al., 1992).

Heat generation and buildup depend on many factors, including the chemical composition

of the cement, water-cement ratio, fineness of the cement, amount of cement, admixture, dimension of the concrete, ambient temperature, and fresh concrete temperature. Tricalcium silicate ($3CaO \cdot SiO_2$) and tricalcium aluminate ($3CaO \cdot Al_2O_3$) are the compounds of cement primarily responsible for the high heat generation. An increase in the water-cement ratio, fineness of cement, and/or curing temperature increases the heat of hydration (Kosmatka et al., 1988). Heat of hydration can be useful in cold weather placement: It often generates enough heat to provide a satisfactory curing temperature, obviating the need for other temporary heat sources (Kosmatka et al., 1988). In hot weather, however, heat of hydration can be detrimental to the concrete.

Environmental Conditions

High temperature in fresh concrete due to ambient air temperature and solar radiation may induce such undesirable effects as increased water demand, increased rate of slump loss, increased rate of setting, increased tendency for plastic shrinkage cracking, difficulties in controlling entrained air, and critical need for prompt curing. In hardened concrete, high temperature may result in decreased strength, increased shrinkage, increased creep and decreased durability (Kosmatka et al., 1988 and Samarai et al., 1983). Figure 5 shows that, for the summer construction, the peak concrete temperature was quite high (in excess of $140^{o}F$), an effect attributed to the high air temperature and to the high initial temperature of the fresh concrete.

Since the hydration of cement is a chemical process, a high ambient temperature will increase the rate at which the concrete hydrates. High solar radiation during construction also plays an important role in increasing the concrete temperature and the rate of hydration. This faster rate of hydration produces a higher and earlier peak concrete temperature during the

7

construction day (Suh et al., 1992).
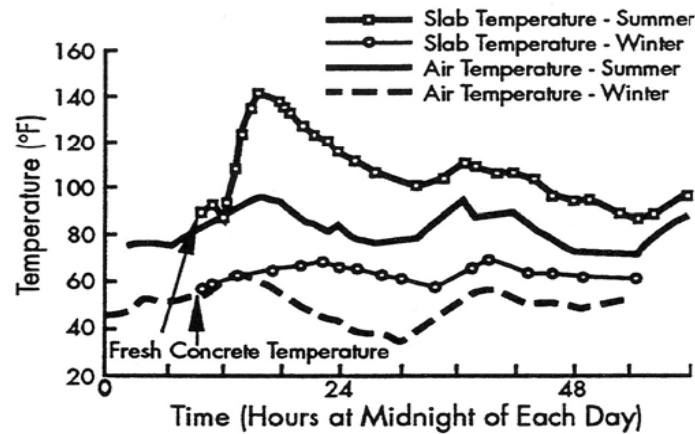
Figure 5. Ambient air temperature effects on the slab temperatures (Suh et al., 1992).

Horizontal Cracking in CRCP

The subject of horizontal cracking in CRCP has not been researched compared to other distress types. This is evidenced by the lack of information on this subject matter. Early age cracking due to the development of microcracks in CRCP ultimately leads to the deterioration of the pavements. The identification of the mechanisms responsible for the horizontal cracking in CRCP is crucial in the development of mitigation methodologies. This requires an accurate and in depth analysis of the CRCP responses at early ages due to environmental loading application, concrete preparation techniques and material condition.

In this study, two papers were identified on the subject of horizontal cracking in CRCP. One paper was prepared Elfino and Steele, (2001) and the other Kim and Won (2004). Elfino and Steele, (2001) describes distresses due to horizontal cracking in CRCP. Even though they did not specifically use the term "horizontal cracking," they depicted distresses due to horizontal cracking under localized areas of broken concrete. They did not perform any analysis or field evaluations but they described the distresses observed in the field due to horizontal cracking and provided their explanation on the possible causes.

8

They made several statements on horizontal cracking and resulting distresses as follows:

(a)   Shear stress in slabs has a parabolic distribution, with the highest stress at mid slab, which could explain the delamination at that location.

(b)   The curling action of the concrete due to drying and temperature changes may be the most significant contributor. The dissimilarity between the reinforcing steel and the concrete in thermal and drying shrinkage may be a contributory factor in causing the delamination to be located at the level of the steel. The selection of ingredients and their proportioning affect the shrinkage curling.

(c)   After the concrete slab has delaminated, it separates into two layers at the reinforcing steel. Now, the axle loading is carried by the upper layer, making it easy to break mainly in the wheel path of truck (Elfino and Steele, (2001).

Figures 6 (a) and (b) show horizontal cracking distresses in CRCP.
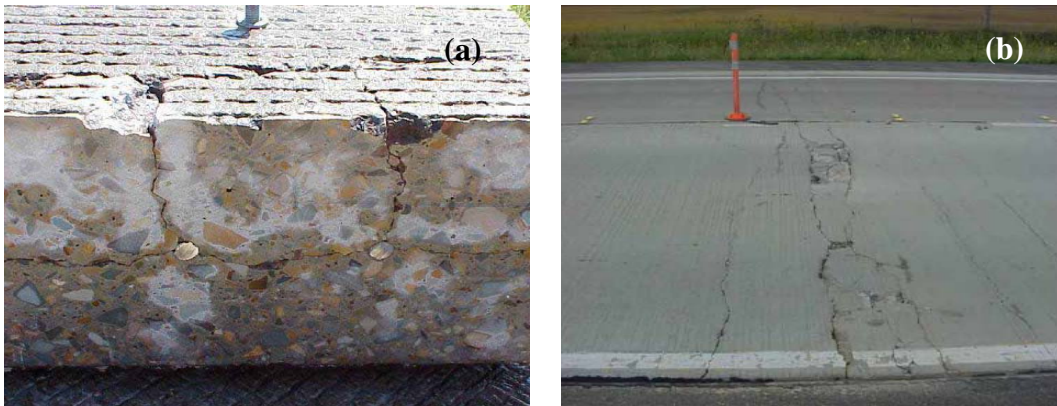
Figure 6. Horizontal cracking distresses in CRCP (Courtesy of the Center of Transportation Research, University of Texas at Austin).

In their theoretical analysis to estimate the effects of several design, environmental, and materials variables (number of steel layers, temperature variations, and thermal coefficient of thermal expansion and modulus of elasticity of concrete) on the potential for horizontal cracking, Kim and Won (2004) utilized a finite element modeling as shown in Figure 7. They based their analysis on horizontal cracking observed in Texas.
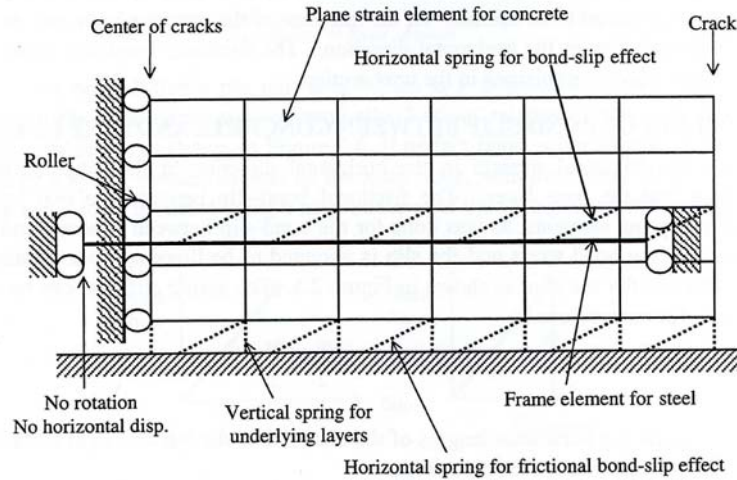
Figure 7. Finite element model of CRCP (Kim & Won, 2004).

They introduced bond slip element to model the interface between concrete and longitudinal steel with the assumption that concrete behaved in plane strain mode.

Figure 8 shows normal and shear stresses along the slab depth at transverse crack for two different temperature gradients. They found that higher temperature differentials between the top and bottom of the slab resulted in larger concrete stresses at the depth of steel.
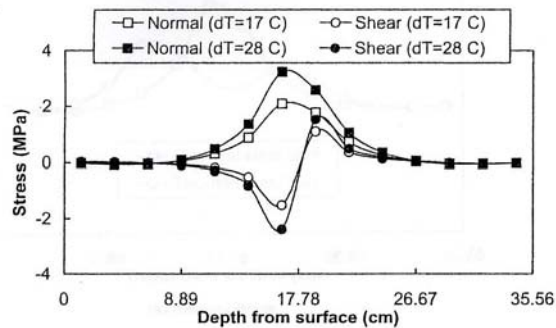
Figure 8. Effect of temperature variation on stress distribution along slab depth (Kim & Won, 2004).

Figure 9 illustrates the effects of concrete coefficient of thermal expansion (CTE) on normal and shear stresses along the slab depth. Concrete with higher CTE yields larger stresses in concrete. These results were compatible with the field observations, where concrete with high

10

CTE – concrete containing siliceous river gravel or sandstone – is more prone to horizontal cracking than concrete with low CTE – concrete containing crushed limestone.
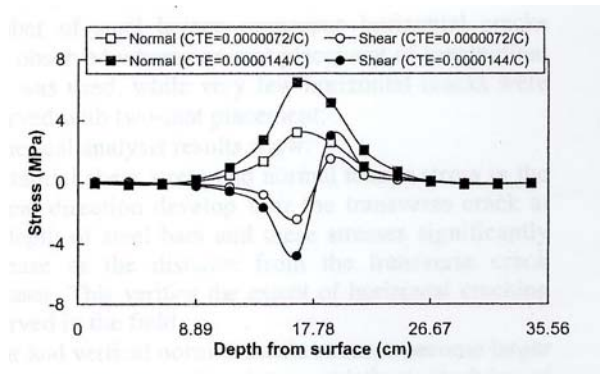
Figure 9. Effect of concrete coefficient of thermal expansion on concrete stress (Kim & Won, 2004).

Figure 10 shows the effect of concrete modulus of elasticity on the normal and shear stresses along the slab depth. They noted that concrete with higher modulus experiences larger normal and shear stresses. This finding also corroborated well with field observations, where concrete with higher modulus such as concrete containing hard siliceous river gravel had higher potential for horizontal cracking than concrete with lower modulus.
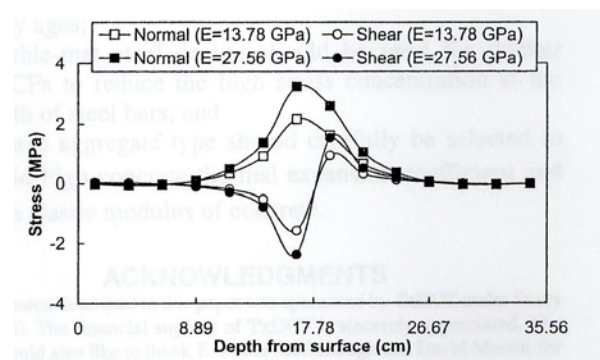
Figure 10. Effect of concrete modulus of elasticity on stress distribution along slab depth (Kim & Won, 2004).

Since only two papers were identified addressing horizontal cracking in CRCP, this was an indication of the unfamiliarity with this issue among researchers and practitioners. The finite element modeling used by Kim and Won, (2004) is not sophisticated enough to provide

quantifiable relationships, which could be used to develop design standards or specifications to mitigate horizontal cracking. More realistic and sophisticated modeling using advanced theories of concrete cracking is therefore needed.

Crack Initiation and Propagation

Structural design of concrete pavements is aimed at fulfilling the requirements of safety, durability and serviceability. In order to meet the safety requirements, the pavement is required to carry the applied loads and deformations subjected to it by traffic or the environment. It is also expected to withstand deterioration due to environmental influences. The evaluation of the service life of reinforced concrete pavements is achieved by the prediction of time to cracking. This is because the appearance of the first crack is usually used to define the end of the functional life where rehabilitation of structural element occurs. In order to understand the formation, propagation and interaction of cracks, examination of the basic structure of concrete is important.

Examination of a cross-section of concrete reveals two distinct entities: aggregate particles of varying size and shape and the binding medium that is composed of an incoherent mass of hydrated cement paste. At the microscopic level, these two entities are neither homogeneously distributed with respect to each other nor homogeneous themselves. The structure of the hydrated cement paste near the large and fine aggregate particles is usually very different from the structure of the bulk paste. This complex mass must therefore be viewed as a three-phase composite structure: a cement paste phase, bonded to the aggregate phase; and a transition zone, which represents the interfacial region between the particles of coarse and fine aggregates and the hydrated cement paste.

CHAPTER II

PURPOSE OF THE THESIS

Problem Statement

The two types of Portland cement concrete (PCC) pavements used as rigid pavement systems for highways include the jointed concrete pavement (JCP) and the continuously reinforced concrete pavement (CRCP). The districts of the Texas Department of Transportation (TxDOT) decided to use CRCP as the primary PCC pavement type because of the excellent performance history of CRCP, which include high durability and strength characteristics. These assure its longevity, low maintenance costs and smooth ride quality.

Even though the performance of CRCP in Texas has been excellent, some sections have had to be rehabilitated before their design lives were reached. The primary distresses experienced included punchouts and spalling.

Punchout is the major structural distress of CRCP. When the concrete slab cracks, the tensile stress in the reinforcement causes the fracture of surrounding concrete near the crack. The fracture of concrete reduces the stiffness of the slab and results in spalling on the crack surface under continuous traffic loadings, which consequently makes the crack open wide and results in the loss of load transfer across the crack. Without the load transfer, the slab between two closely spaced cracks, usually less than 0.610 m (2 ft) apart, acts as a cantilever beam, and as the applications of heavy truck load continue, a short, longitudinal crack forms between the two transverse cracks about 0.610 to 1.524 m (2 to 5 ft) from the pavement edge (Huang, 2004).

Spalling of cracks is the cracking, breaking, or chipping of the slab edges within 0.610 m (2 ft) of the crack. Spalling usually results from excessive stresses at the crack caused by infiltration of incompressible materials and subsequent expansion or traffic loading. It can also

13

be caused by the disintegrated and weakened concrete at the crack caused by the reinforcement excessively stressed in tension.

Pavement distress due to horizontal cracks was first observed in the CRCP section of IH-30 in the Paris district in Texas. This section of pavement is 250 mm-thick CRCP, built in 1986. The typical distress types included pop outs and half-depth punchouts as shown in Figure 11.

Figure 11. CRCP distress caused by horizontal cracking.
(Courtesy of the Center for Transportation Research, University of Texas at Austin)

During the repair work, extensive horizontal cracks were observed in the removed slabs as shown in Figure 12.

Figure 12. Mid-depth horizontal cracks.
(Courtesy of the Center for Transportation Research, University of Texas at Austin)

On close examination of these horizontal cracks, the cracks occurred around the coarse

aggregates, not through the aggregates, which is an indication of early age cracking. On IH-35 in

the Waco district, horizontal cracks at the depth of reinforcing steel were observed in a relatively

new CRCP that was not yet open to traffic. These cracks were observed to initiate and propagate

from the mid section where the rebar steel placement is done.

Several changes were made in terms of structural improvements, pavement design and

construction. These changes included using thicker slabs, stabilized bases and tying concrete

shoulders. These however did not alleviate the punchout problem.

In this project, the mechanisms and factors responsible for horizontal cracking were

identified. Since past research approach in CRCP studies were "macroscopic" in nature, the

microscopic behavior of concrete and steel in CRCP was investigated.

Purpose of the Research

The purpose of this research was to identify the significant factors and processes

responsible for horizontal cracking in CRCP. An in-depth analysis of the microstructure of the

interfacial transition zone (ITZ) was studied and various experiments were undertaken to analyze

the interfacial chemistry and morphological characteristics of the concrete mix and steel rebar.

The experiments undertaken included:

- Measurement of concrete-steel bond strength

- Characterization and identification of oxides using Fourier transform infrared
  spectroscopy (FTIR) and electron dispersive x-ray spectroscopy (EDS)

- Observation of cracking using the environmental scanning electron microscope (ESEM)

Research Questions

1. What is the effect of rebar temperature at the concrete pouring stage on the concrete-rebar bond strength?

2. What effect does changing the water to cement ratio have on bond strength?

3. What effect does using non-corroded rebar steel versus corroded rebar steel have on the concrete-rebar strength and does corrosion play a role in horizontal crack formation?

4. How does the morphology of the interfacial transition zone change with the rebar temperatures, using different w/c ratios and using corroded and non-corroded rebar steel?

Statement of Need

Attention to the design and construction quality control in CRCP is critical not only for the longevity and service life of the concrete pavement but also for the safety of the road users. Texas being a large state had about 9,400 lane miles of continuously reinforced concrete pavement (CRCP), and about 4,100 lane miles of JCP in 2006 (Du and Lukefahr, 2007). The TxDOT spends more than 50% of the annual construction and maintenance budget on pavements (Pavement Design Guide 2006).

Due to the initial costs incurred during the construction of the concrete pavements, preventative measures should be taken to prevent the occurrence and propagation of horizontal cracks that ultimately lead to expensive repair of the concrete pavements. Hitherto, no study has been undertaken to understand the microscopic behavior of concrete and rebar temperature in CRCP and the intricacies of the ITZ. Thus, this unique study is of significant importance: paving a new way in defining a solution to the problem of horizontal cracking in CRCP.

Research Method

The research method for this study is experimental. The ITZ between concrete and rebar

was quantitatively studied and microstructural analysis performed using ESEM and EDS. This shed light on the fundamentals underlying the formation of horizontal cracks and the morphological aspects of the corrosion products that lead to the rapid deterioration of CRCP.

CHAPTER III

LITERATURE REVIEW

The property of concrete, which is a highly complex heterogeneous material, depends on the properties of its component phases [aggregate, matrix and interfacial transition zone (ITZ) between the aggregates and the matrix] and the interactions between them. The ITZ plays an important role in determining the mechanical properties and failure behavior of concrete composites (Akcaouglu et al., 2005). Research shows that the thickness of the ITZ is 40 -50 μm and the adhesion between the aggregate and cement paste within the transition zone is a factor that governs the concrete strength (Prokopski and Halbiniak, 2000). The structure of the ITZ is determined by the water to cement ratio (w/c) of the mixture, cement and the properties of the aggregates including type, shape and surface conditions. Porosity of the ITZ is higher than that of the bulk paste therefore having a significant effect on the permeability and durability of concrete (Basheer et al., 2005).

It has been proposed that the mechanisms behind the existence of the ITZ is first due to the influence of the so called "wall effect"; here, due to the aggregates, the arrangement of the anhydrous cement particles become loose near the aggregate surface. This results in the local water to cement ratio (w/c) and the porosity being higher while the w/c ratio of the cement paste becomes lower. Secondly, microbleeding under the aggregates during vibration could also be responsible for the ITZ (Cwirzen and Penttala, 2005). Bourdette et al. (1995) stated that the diffusion coefficient of chloride ions could be 6-12 times greater in the transition zone compared to bulk paste. This therefore facilitates the ingress of external agents thus supporting various deleterious chemical reactions.

Various research studies undertaken have found that the bond strength is closely related

with the type, shape and surface texture of the aggregate used (Zimbelman, 1985, Hsu et al., 1964 and Prokopski et al., 2000). Lowering the w/c ratio improves the microstructure of the interface because it reduces porosity and the lower the w/c ratio, the thinner the ITZ (Tasong et al., 1999). The pores in the cement paste and aggregate components of concrete are considered very important in the determination of hardened concrete properties.

The engineering properties of concrete such as permeability, shrinkage, strength and durability are determined by the number, type and size of pores. The strength and elasticity is affected by the total volume of pores whereas concrete permeability is affected by the pore volume, size and continuity. Deterioration of concrete structures can be attributed to the movement of liquids, gases and ions and their interaction with the concrete constituents and pore water. In reinforced concrete structures, corrosion is a major cause of deterioration.

Nemati and Monteiro (1998) investigated the influence of the geochemical properties of natural rock aggregates on the nature of the ITZ. They used basalt, limestone and quartzite aggregate samples for their study. They concluded that the type of aggregate material used has a different chemical interaction with the cement paste and could greatly influence the bond strength. They noted that the limestone aggregates had the greatest influence on the nature and character of the ITZ compared with the other aggregates; the ITZ around the limestone aggregates was more porous that that of basalt and quartzite. This was attributed to the release of carbon dioxide gas because of the chemical interaction between the limestone and the hydrating cement paste. This led to a reduction in strength at an early age.

In Part II of their study, Tasong et al., (1999) studied the effects of aggregate mechanical and physical properties. This included surface roughness, on the bond strength at the ITZ and concluded that the "apparent" interfacial bond strength for a given cement paste is not a simple

function of aggregate surface roughness, but also a function of parent rock structure, both of which determine the topography and the fracture properties of the aggregates at the ITZ.

The matrix properties also have a great influence on the initiation and propagation of cracks. The large difference between the elastic moduli of the matrix and the aggregate induces higher tangential, radial and /or shear stresses at matrix aggregate interface. This causes the existence of a critical stress level where rapid and continuous crack propagation starts, and this is influenced by the aggregate properties and elastic compatibility between the matrix and the aggregate (Tasong et al., 1998). The increase in microcrack concentration at the ITZ after the concrete has been loaded acts as a source of the development of macrocracks. The quality of the matrix will therefore be dependent on the tendency of these microcracks to connect and coalesce.

Influence of Corrosion Products on the ITZ

Under normal operating conditions, the reinforced steel embedded in concrete forms a very stable passive film of iron oxides at the steel-to-concrete interface due to the high alkalinity of the Portland cement concrete pore solution. This solution is mainly consisted of saturated $Ca(OH)_2$ (pH = 12.6) which increases to more than 13 with the presence of NaOH and KOH (Giaccio et al.,1992). This passive layer can however be broken by carbonation or by chloride ingress into the concrete structure. In the presence of oxygen and moisture, corrosion of the steel will begin once this layer is broken and this will result in the formation of expansive corrosion products (rust) which occupy several times the volume of the original steel consumed.

Corrosion is an electrochemical process involving the establishment of anodic and cathodic half-cell reactions on the microscopic and/or macroscopic levels. In high pH solutions and in the absence of chloride ions, the anodic dissolution reaction of iron:

$$Fe \rightarrow Fe^{2+} + 2e^-$$
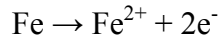
is balanced by the cathodic reaction:

$$\tfrac{1}{2}\,O_2 + H_2O + 2e^- \rightarrow 2OH^-$$
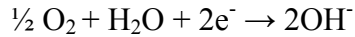
in addition, the Fe^{2+} ions combine with the OH^- ions to produce the stable passive film.

This electrochemical process is illustrated in Figure 13 (Andrade et al., 1995).
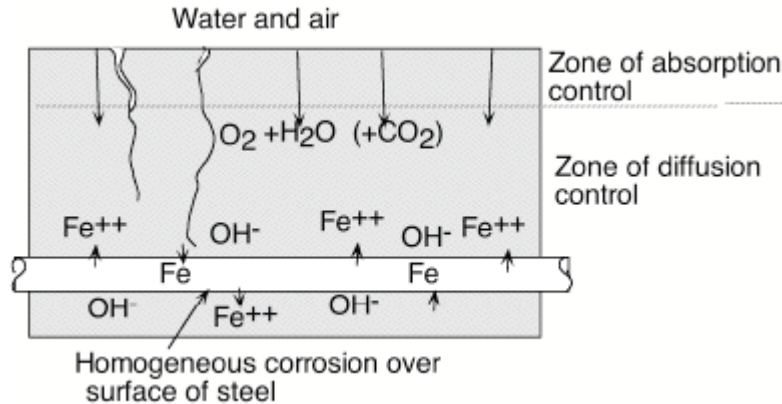
Figure 13. Schematic representation of passive corrosion (Andrade et al., 1995).

Chloride Induced Corrosion

Since the mechanism by which the chloride ions break down the passive film is not fully understood, it has been hypothesized that:

- The chloride ions become incorporated into the passive film and reduce its resistance

- The Cl^- ions "compete" for the OH^- anions for combining with Fe^{2+} cations and, because the Cl^- ions form soluble complexes with the Fe^{2+} ions, a passive film is not formed and the process stimulates further metal dissolution (Andrade et al., 1995).

The soluble iron-chloride complexes diffuse away from the steel and subsequently break down, resulting in the formation of expansive corrosion products. These expansive corrosion products create tensile stresses on the concrete surrounding the steel reinforcing bar and this can lead to the cracking of the concrete. Table 1 shows the corrosion products that can be formed.

Table 1. Iron and iron oxide properties (Kibaschewski & Hopkins, 1962; Hansson et al., 2007).

Iron oxide	Molar Volume cm3/mol Fe	Volume ratio[A]	Characteristic color
ά - Fe	7.1	1	metallic silver
Fe_3O_4, magnetite	14.9	2.1	black
ά- Fe_2O_3, hematite	15.2	2.14	earthy red or black
ά - FeOOH, goethite	21.3	3	blackish, yellowish or reddish brown
γ -FeOOH, lepidocrocite	22.4	2.15	deep red or reddish brown
β - FeOOH, akaganite	27.5	3.87	brown to rusty brown
$Fe(OH)_2$	26.4	3.72	pale green or white

[A] Ratio of molar volume of iron oxide to molar volume of ά - Fe

Once the diffusion process has occurred, the Cl⁻ ions are simultaneously released and these migrate back to the anode to react further with the steel. As the hydroxyl ions are consumed during the process, the solution pH decreases enhancing further the metal dissolution. Since the Cl⁻ ions are not consumed, the attack becomes "autocatalytic" seriously compromising the reinforcement cross-section and its structural resistance. Figure 14 shows a schematic of the illustration of chloride diffusion in cracked concrete (Higgins et al., 2003).
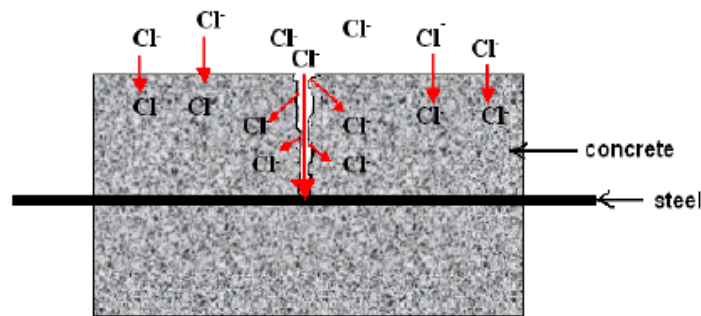
Figure 14. Schematic illustration of chloride diffusion in cracked concrete (Higgins et al., 2003).

Carbonation-Induced Corrosion

When carbon dioxide from the atmosphere reacts with calcium hydroxide (and other hydroxides) in the cement paste, the pore solution is neutralized.

$$Ca(OH)_2 + CO_2 \rightarrow CaCO_3 + H_2O$$
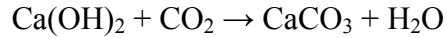
The rate at which carbonation advances is a function of relative humidity (RH) and this increase with time. At low RH, the penetration of CO_2 into the concrete is highest. Figure 15 shows the influence of relative humidity on the rate of carbonation of concrete (Tuuti, 1980).
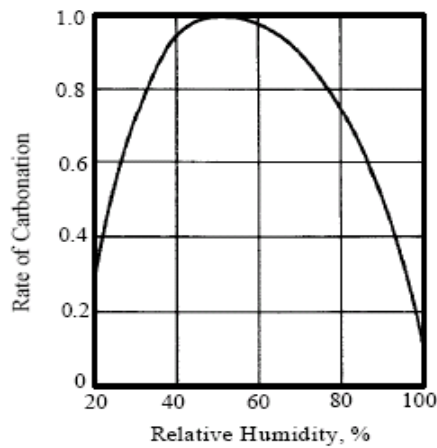
Figure 15. The Influence of relative humidity on the rate of carbonation of concrete (Tuuti, 1980).

As the carbonation front penetrates the concrete, its rate will decrease over a given period because of the following reasons:

- The gas has to penetrate deeper into the concrete

- The concrete becomes impermeable as it ages because of hydration

- The carbonation itself decreases the permeability by the precipitation of the carbonate in the existing pores and the reaction releases water, which further aids in the hydration process

The passive film is no longer stable when the carbonation front reaches the reinforcement and it is then that active corrosion initiates.

Prediction of Time from Corrosion Initiation to Corrosion Cracking

Prediction of time to corrosion cracking is a key element in evaluating the service life of corroding reinforced concrete structures. This is because the appearance of the first corrosion

crack is usually used to define the end of functional service life where rehabilitation of a corroding structural element is required (Tuuti, 1980 and Weyers, 1998).

The prediction of time to corrosion cracking is also important in the determination of the relationship between bond strength and degree of corrosion. This is because the bond strength at the steel-to-concrete interface of a corroding reinforced concrete element initially increases with the increase of corrosion up to cracking of concrete cover, after which time the bond strength decreases as corrosion progresses (State of the art report, Bulletin no. 10, International Federation for Structural Concrete, Switzerland; 2000).

Tuuti, (1980) developed a conceptual model for the service life prediction for corroded reinforced concrete structure. This is shown in Figure 16. There are two distinct periods in deterioration caused by corrosion according to this model. The first is the initiation period, T_o, which represents the time required for CO_2 or Cl^- ions to diffuse to the steel-to-concrete interface and activate corrosion. The second is the propagation period, T_{cr}, which represents the time between corrosion initiation and corrosion cracking.
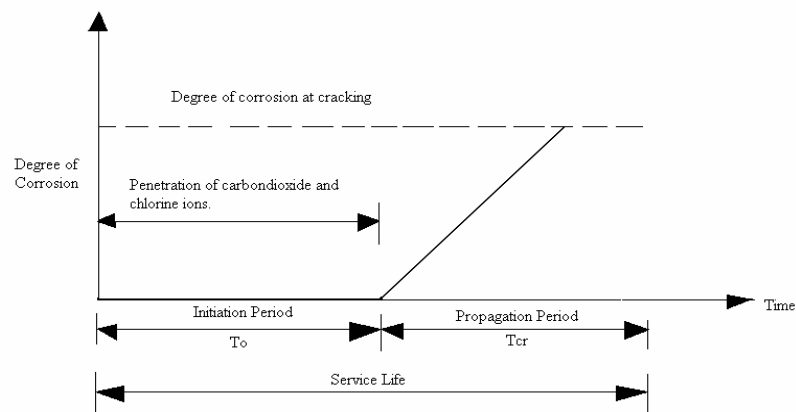
Figure 16. Service life model of corroded structures (Tuuti, 1980).

Weyers, (1998) reported that not all corrosion products contribute to the expansive pressure on the concrete; some of them fill the voids and pores around the steel reinforcing bar

24

and some migrate away from the steel-to-concrete interface through the concrete pores. He

concluded that the conceptual model presented by Tuuti, (1980) underestimates the time to

corrosion cracking compared with times obtained from field and laboratory observations. He

reported that there is a porous zone around the steel reinforcing bar caused by the transition from

cement paste to steel, entrapped/entrained air voids, and capillary voids in the cement paste into

which corrosion products diffuse. A schematic diagram of the corrosion-cracking process as

proposed by Weyers, (1998) is shown in Figure 17. A modified service life model in which the

propagation period T_{cr}, divided in two different periods is shown in Figure 18.
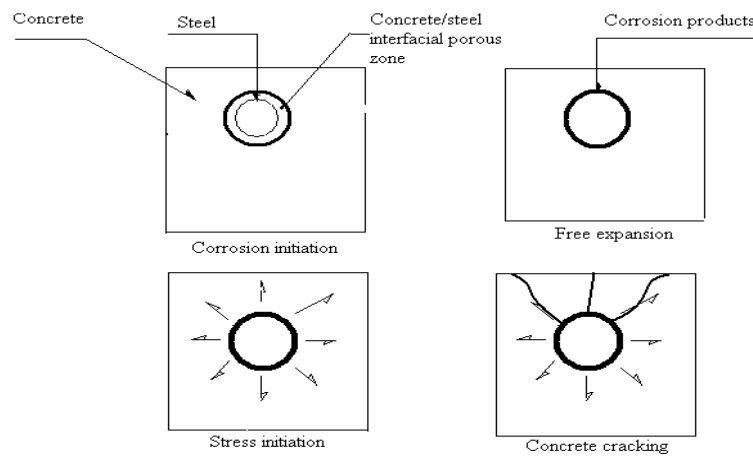
Figure 17. Corrosion and cracking process Weyers, (1998).
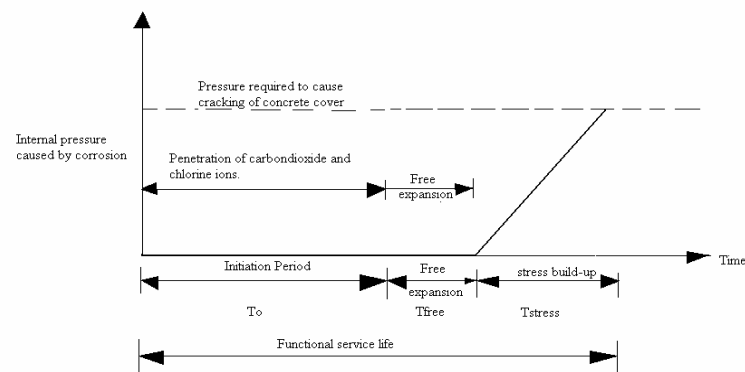
Figure 18. Modified service life model (Weyers, (1998).

The first period is the free expansion period, T_{free}, this corresponds to the time required for

corrosion products to fill the porous zone around the steel reinforcing bar. The second period represents the time in which the stress builds up, T_{stress}, as corrosion products, having filled the porous zone, exert an expansive pressure on the surrounding concrete. Weyers, (1998) model assumes that this pressure increases linearly as the volume of corrosion products increases until the internal tensile stresses exceed the tensile strength of concrete at which time cracking of concrete cover occurs.

Morinaga, (1988) proposed and empirical equation based on field and laboratory data to predict the time from corrosion initiation to corrosion cracking:

$$T_{cr} = \frac{0.602D\ (1+2\ C/D)^{0.85}}{i_{corr}}$$

Where T_{cr} is the time from corrosion initiation to corrosion cracking (days),

   D is the steel bar diameter (mm)

   i_{corr} is the corrosion rate (10^{-4}g/cm^2/day)

   C is the cover thickness (mm)

According to Morinaga's equation, the time from corrosion cracking is a function of corrosion rate, concrete clear cover, and steel bar diameter. Morinaga's equation does not account for the mechanical properties of concrete, which would significantly affect the time to corrosion cracking. This equation cannot therefore be generalized to predict the time from corrosion initiation to corrosion cracking for a concrete having various mechanical properties.

Effect of Rebar Embedment Length on Concrete Bond Strength

The most important property contributing to a successful reinforced concrete structure is the bond strength between the reinforcing steel and concrete. In order for the concrete to achieve

its designed capacity, a strong bond must be developed. The factors that influence the bond strength include:

- Rebar diameter

- The presence or absence of bar surface deformations (ribs)

- The geometry of the ribs

- Concrete cover over the bars

- The orientation in the concrete matrix

- Concrete loading conditions

- Construction details

In case of deformed steel bars, the bond strength and the process of bond transfer from the reinforcing bars to the surrounding concrete relies on the chemical adhesion and the friction (dependent on the bar surface condition), and the mechanical interlocking of the bar ribs on the concrete paste surrounding the bar (dependent on the bar deformation pattern).

One of the construction details that influences bond strength is the rebar embedment length. Several research studies have been undertaken to determine the effect of varying the embedment length when performing standard pullout and beam end specimen tests. Tighiouart et al., (1998) conducted a study using glass fiber reinforced polymer (GFRP) rebar in beam-end bond specimens. Sixty-four beam end tests were carried out in accordance to RILEM specifications. No. 4, 5, 6, and 8 bars were tested at embedment lengths of 6, 10 and 16 bar diameters. They found that as the embedment length increases, the load approaches the tensile strength of the bars and there is a reduction in the average bond strength. They explained the decrease in bond by a non-linear stress distribution along the embedment length of the rebar.

Chaallal and Benmokrane (1996) performed another study using direct pullout method.

Twenty four tests were performed using 30MPa concrete, on No. 4, 5 and 6 fiber reinforced concrete (FRP) bars, at embedment lengths of five and ten times the bar diameters. They performed four tests per bar size per embedment length. The bond strength of the bars ranged from 11.1 MPa to 15.1 MPa with an overall average bond stress for all the bars of 12.9 MPa. Their findings on the effect of the embedment length on bond strength were similar to that of Tighiouart et al., (1998). They found that the bond strength was lower for the larger embedment lengths. These effects can be related to steel rebar in that Tighiouart et al., (1998),Chaallal and Benmokrane (1996) also found out that the distribution of the tensile and the bond stresses along the embedment length for the GFRP rebar is similar to that of the steel rebar.

In general, the tensile stress reduces rapidly from the loaded end to the free end.

Bond Failure

The two typical modes of failure used to describe the bond mechanism of reinforcing steel bars and surrounding concrete are:

(a) Splitting bond failure
(b) Pullout failure

Splitting Failure

This results from splitting of the smallest concrete cover surrounding the bar and is most likely to occur in cases of low levels of confinement around the bonded bar or wedging effect of the bar deformations. The type of splitting failure depends on the relative difference among bar spacing, bottom or top cover, and side cover. When the side cover is less than the top cover or half of the bar spacing, a side split failure occurs (Figure 19 (a)). When half of the bar spacing

and the side cover are both greater than the top cover, a V-notch split failure occurs (Figure 19 (b)).

Pullout Failure

This results from crushing and shearing off of the concrete keys enclosed between the bar ribs along a cylindrical plan of failure which passes by the rib tips. Pullout failure occurs if the radial confinement, caused by the presence of relatively thick concrete covers and /or excessive transverse stirrups, is greater than the transverse bond force that causes splitting of the surrounding concrete. Pullout failure is shown in Figure 19 (c).
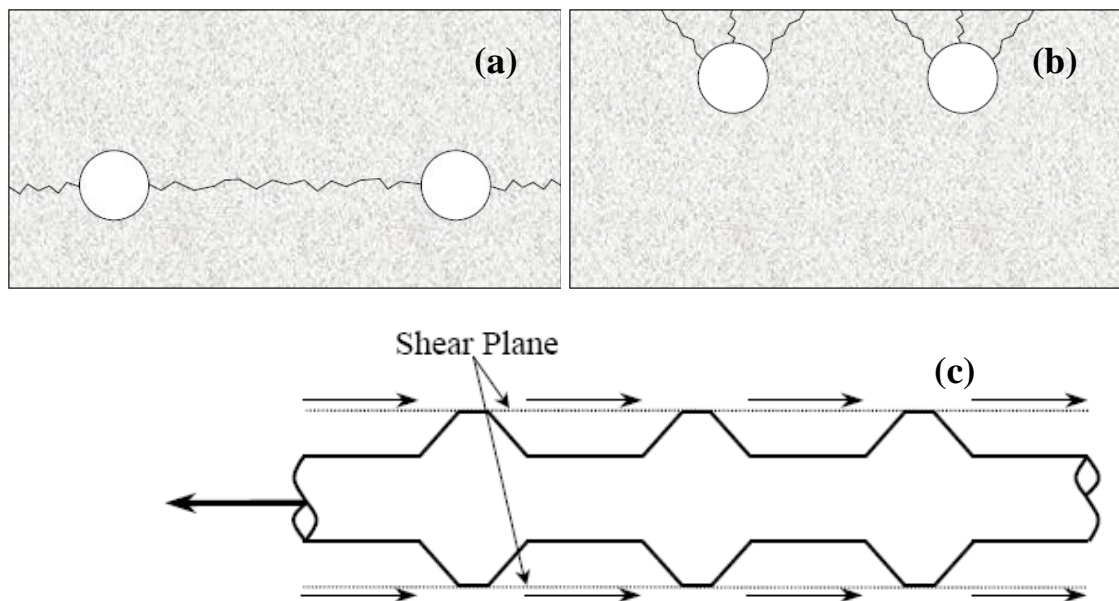
Figure 19. Side split failure (a), V-notch failure (b), Pullout failure (c). (Seddelmeyer et al., Research Report 4904-3, 2000).

CHAPTER IV

EXPERIMENTAL APPROACH

Specimen Preparation

Laboratory test specimens were prepared as per ASTM Standard C 192/C 192M-00 "Standard Practice for Making and Curing Concrete Test Specimens in the Laboratory". Cylindrical casts with a diameter of 4 in x 8 in. length were used for this experiment. The cylindrical casts were made from concrete test cylinder molds conforming to ASTM 470 standard. These dimensions were chosen because they are lightweight, small, consume less material and require lower area for curing period. Fine aggregate gradation was done in accordance to ASTM C 136, "Sieve or Screen Analysis of Fine and Coarse Aggregates". Gradation results are shown in Table 2. The gradation curve generated form the results showed the fine aggregate type to be dense or well graded referring to a gradation that is near maximum density. The sieve analysis curve is shown in Figure 20.

Table 2. Fine Aggregate gradation results.

Sieve Size	Mass retained (g)	Individual % retained	Cumulative % retained	Total % passing
No.4	41	1	1	99
No.8	95	3	4	96
No.16	115	4	8	92
No.30	344	12	20	80
No.50	1182	40	60	40
No.100	584	20	80	20
No.200	546	18	98	2
Pan	49	2	100	0
TOTAL	2963	100	-	-

Fineness Modulus of Sand = Σ (Cumulative % retained)/100
= (1+4+8+20+60+80+98)/100 = 2.71

The result obtained from the fineness modulus calculation shows that the sand used for this experiment falls within the expected range for sands used in concrete, which is 2.3 to 3.1. The

coarser the fine aggregate, the higher the fineness modulus (ACI Education Bulletin E1-99).
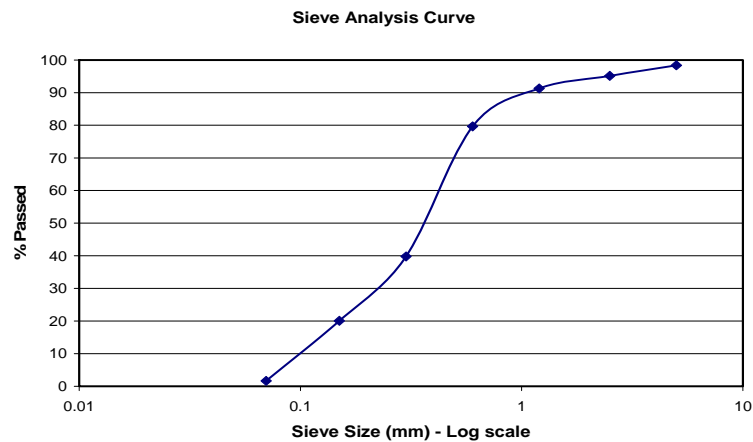
Figure 20. Gradation Curve for dense or well-graded fine aggregate.

Bar Properties

The rebar steel, used for this experiment, was in accordance to ASTM A615 "Standard

Specification for Deformed and Plain Billet-Steel Bars for Concrete Reinforcement". The # 6 bar

properties used are shown in Table 3.

Table 3. ASTM A615 Requirements (American Society for Testing and Materials, Pennsylvania, 2001).

Bar Size	Nominal Weight (lb/ft)	Nominal Diameter (in)	Cross-sectional area (in.^{2})	Deformation Requirements (inches)		
				Maximum Average Spacing	Minimum Average Height	Maximum Gap
6	1.502	0.75	0.44	0.525	0.038	0.286

Experimental Program

The experimental program was designed to evaluate the bond strength, including the

ultimate bond strength, horizontal cracking, free end slip and modes of failure of the test

specimen. Since cracks were observed at an early age even before the pavement was open for

traffic, the concrete mixes were designed using Ordinary Portland cement (OPC) Type I II, sand

and aggregates. The rebar steel was placed at the center of the cylindrical specimens. The

embedment lengths of the rebars were varied at 8 inches and 4 inches for each run .After the

specimens were cast, they were covered immediately with a polythene bag to prevent

evaporation. The molds were removed after 32 hours of casting and moist cured by spraying with

tap water at room temperature until the pullout tests were performed.

The pullout tests were conducted at different ages since the bond slip behavior will

change depending on concrete strength (bond strength). The testing was done at 3 days, 10 days,

and 28 days. This allowed for the investigation of the "early age" cracking phenomenon. Table 4

shows the experimental run matrix for the corroded and non-corroded tests. There will be a total

of 54 specimens cast for the 8-in embedded length parameter and 54 specimens cast for the and

4-in embedded length parameter for the corroded and non-corroded rebar tests. There will be 216

specimens cast for this research study.

Pullout Test Specimen Set Up

The bond-slip relationship was examined using the pullout test. This was done in

accordance to the standard RILEM pull out test, AAC 8.1; "Pull out test for reinforcement". This

standard was used because the ASTM standard C234 – 91a "Standard test method for comparing

concretes on the basis of the bond developed with reinforcing steel", was withdrawn in February

2000 (Manual Book of ASTM Standards, 2001). The pullout test was performed in order to

measure the interfacial strength between the rebar and the concrete matrix. The rebar was

gripped by the cross head of an Instron 4482 Tensile tester with a maximum tensile load capacity

of 20 kips (88 KN). A specially designed loading frame was fixed to the base of the Instron

universal testing machine. Advantages of the pull out test include:

1. It offers the advantage of simplicity.

2. The free end of the rod is accessible allowing for the measurement of the free end slip and for the placement of instrumentation.

Some of the disadvantages of using this set up however are:

1. Failure by splitting of the concrete mass may occur at a load below the maximum bond capacity.

2. The compressive stresses existing in the concrete near the loaded end of the rod. These compressive stresses at the loading face are however very small and hence are neglected during the pull out test process.

The tensile tester applied a monotonic load on the rebar embedded in the concrete until bond slip/failure occurred. The pullout load versus slippage readings were collected electronically and recorded by the computer. A high precision linear variable differential transducer (LVDT) was attached on the loaded end of the steel rebar to measure the displacement from the beginning up to the completion of loading. The average shear stress of the bond was calculated using the maximum shear stress equation used by Abdolkarim and Hogg (2005).

$$\mu_{max} = P_{max} / \pi 2 r l_b$$

Where P is the bond force, $2r$ is the diameter, l_b is the bond length.

After conducting the bond test, the specimens were sectioned transversely and longitudinally using a diamond saw to obtain an approximate specimen size of (1.5x1.5x1.5) in suitable for ESEM analysis.

The rebar was gripped at the top by the Instron tester and secured at the bottom by the fabricated steel fixture shown in Figure 21. The pullout test setup is as shown in Figure 22. The LVDT for the measurement of slip was attached at the bottom of the specimen, and connected to

the data logger. The data logger connection and the data logger are shown in Figures 23 and 24 respectively.

Figure 21. Instron tensile testing machine for pullout testing.

Figure 22. Pullout test set-up.
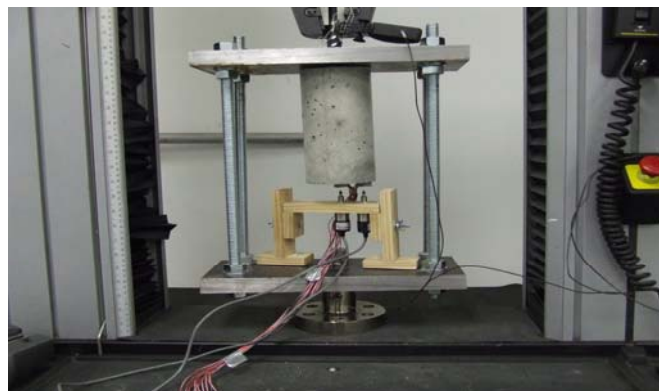
Figure 23. Bottom LVDT connection.

Figure 24. Data Logger.

The pullout rate used was 0.08 in/min with data recorded every one second.

In order to ensure the centricity of the test samples, a wooded fixture was created as shown in Figure 24. A 1 x 6 x 6 select radiata pine was subdivided into 13 sections. Each section was 4 inches in length representing the diameter of cylindrical molds. ¾ in diameter holes were drilled at the center for the insertion of the steel rebar. This ensured that the rebars were centered and consistent for each cast specimen.

Figure 25. Centricity fixture.

Rebar Temperature Control

The rebar temperatures were chosen to simulate normal/ambient conditions, hot summer days and cold winter days. This simulated rebar temperature condition during the concrete placement stage.

The normal/ ambient temperature condition, 77°F, is an approximate room temperature and did not require any adjustment on rebar temperature. Extreme summer temperature of 252°F was achieved by heating the rebar to the desired temperature in a temperature control oven. Rebars were left in the oven for four hours to ensure even heat distribution. Since pavement construction also takes place in extreme winter conditions as shown in Figure 26, a rebar temperature of 14°F was used, and this was achieved by adjusting the thermostat in the refrigerator to the 14°F-desired temperature. Rebars were left to cool for four hours to ensure even cooling on the rebar surface.

Figure 26. CRCP construction in winter conditions (Picture taken on 4/6/2008).

Once the desired temperature was reached, the rebars were removed and immediately inserted in the concrete specimens.

Table 4 shows the experimental run matrix for the 8-in embedment length experiments for the corroded and non-corroded rebars.

Table 4. Experimental run matrix for corroded and non-corroded rebars tests.

Run @ 2 specimens per run	W/C	Temperature (°F)	Embedded Length (in)	Pullout Time (Days)
1	0.40	14	8	3
2	0.40	14	8	10
3	0.40	14	8	28
4	0.45	14	8	3

(table continues)

36

Table 4 *(continued).*

Run @ 2 specimens per run	W/C	Temperature (°F)	Embedded Length (in)	Pullout Time (Days)
5	0.45	14	8	10
6	0.45	14	8	28
7	0.50	14	8	3
8	0.50	14	8	10
9	0.50	14	8	28
10	0.40	77	8	3
11	0.40	77	8	10
12	0.40	77	8	28
13	0.45	77	8	3
14	0.45	77	8	10
15	0.45	77	8	28
16	0.50	77	8	3
17	0.50	77	8	10
18	0.50	77	8	28
19	0.40	252	8	3
20	0.40	252	8	10
21	0.40	252	8	28
22	0.45	252	8	3
23	0.45	252	8	10
24	0.45	252	8	28
25	0.50	252	8	3
26	0.50	252	8	10
27	0.50	252	8	28

Rebar Corrosion

The corrosion of the rebars used for this study was achieved by using the Atlas CCX 3000 Advanced Cyclic Exposure System and the corrosion process done in accordance to ASTM Standard G 85-02; "Standard Practice for Modified Salt Spray (Fog) Testing". Figures 27 shows the interior cabinet of the Atlas CCX 3000 Advanced Cyclic Exposure System salt fog testing machine with the atomizing nozzles, specimen support chambers clearly visible. The rebars were left to corrode in the SFG tester for six weeks.

Figure 27. Interior chamber of the Atlas CCX 3000-Advanced Cyclic Exposure System.

ESEM Examination

After mechanical testing, the samples were examined using environmental scanning electron microscopy. The use of a scanning electron microscope is ideal because the image obtained from the concrete sample will be magnified to a point similar to a traditional microscope but with more depth of field, making this technique useful for morphological analysis. An FEI Quanta 200 ESEM was used to examine the interfacial transition zone.

The principle of operation of a scanning electron microscope begins with the production of a beam of electrons by an electron gun. These electrons are then accelerated towards the sample to be rastered. The electrons then passes through one or two condenser lenses forming a fine probe that later is rastered over the sample by the scanning coils in the objective lens (Figure 28). The electrons penetrate the surface forming a teardrop volume that creates the scattering effect, which is the emission of electrons or photons. The detectors corresponding to each type of scattered electrons or photons then collect the electrons and photons. The electrons detected are then converted into voltages and amplified. They are then applied to the cold cathode tube (CRT) grid to produce the image. The three types of images produced are backscattered electrons

images, secondary electron images and elemental X-rays. The electron beam raster over the surface creates for each point of the sample a point in the image (Brundle et al., 1992).
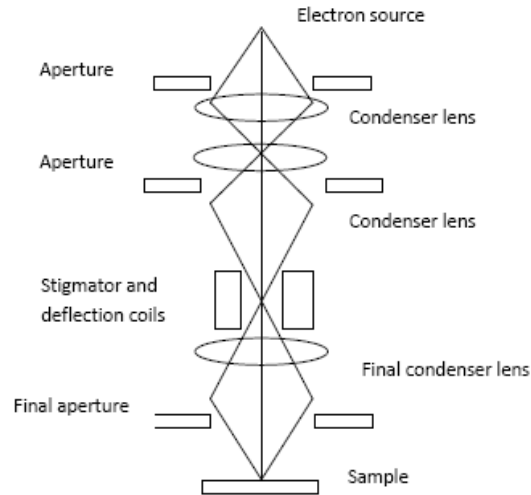
Figure 28. Schematic of scanning electron microscope.

The procedure for sample preparation for microstructural analysis followed was that used by Diamond, (2001), Diamond and Huang, (2001). Since we were examining the rebar-concrete bond area, the grinding of the specimen was not done. This allowed for the study of the fundamentals underlying the formation of cracks, identification of failure modes and the morphological aspects of the corrosion products, which lead to the rapid deterioration of CRCP.

Characterization of Oxides using FTIR

The non-destructive characterization of iron oxides using infrared spectroscopy was performed. Fourier-transform infrared spectroscopy allowed for the rapid collection of data together with increased resolution of the sample under investigation. The ability of the infrared spectrometer to provide information on the chemical bonding which varies depending on the

material under investigation was important for the determination of the predominant oxide

present on the aggregate-cement and concrete-steel bond interface.

In this research, a Nicolet Aviator 370 DTGS FTIR in Attenuated Total Reflection (ATR)

mode with Omnic software was used to obtain the infrared spectra in transmittance or

absorbance vs. wavelength. The FTIR operation involves a beam of light travelling through a

sample with I_o intensity and leaving the sample with I_t intensity interacting with the different

bonds in the sample. The ratio of these intensities as a function of the frequency of the light is the

infrared spectrum represented by:

$$T_w = (I_t/I_o)_w$$

Where T_w is the transmittance of the sample. The beam is reflected through an optically dense

crystal at a certain angle. Once the sample is placed in contact with the crystal, the infrared

radiation interacts with the sample producing a transmittance-like spectrum. At the surface of the

sample, an evanescent wave is produced. The energy produced from the evanescent wave that is

altered or attenuated passes back to the beam, which exits at the end of the crystal to form the

spectrum, as is shown in Figure 29.
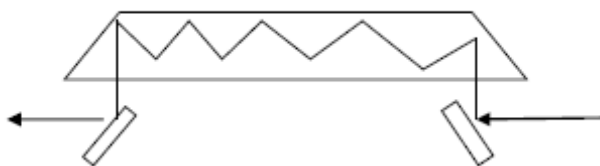
Figure 29. Schematic of attenuated total reflection (ATR) in FTIR.

The infrared spectrum has three characteristics that could be used to make quantitative

analyses; peak position, integrated peak intensity and peak width. The peak width is mostly used

for qualitative identification due to the unique chemical group characteristics. The integrated

peak intensity is proportional to the concentration of absorbing bonds, when a band arises from a

particular vibrational mode. The peak width is a function of the homogeneity of the chemical

bonding, where the full width at half maximum (FWHM) is a characteristic for defects and bond

strain. The change in strength of chemical bonds cause shift in peak position (Brundle, Evans

and Wilson, 1992).

CHAPTER V

RESULTS AND DISCUSSIONS

Since the long-term performance of CRCP depends on not only the proper pavement design and materials selection, but also good construction practices, this research sought to investigate the effect of these factors and their influence on the horizontal cracking on CRCP.

Investigation on the effect of w/c ratios (0.40, 0.45, and 0.50), rebar temperature (14°F, 77°F and 252°F) was done to determine their influence of rebar-concrete bond strength. The effect of steel corrosion on bond between steel rebar and concrete was analyzed using corroded and non-corroded rebars. This is because the presence of iron oxides on the rebar concrete interface creates tensile stresses that can lead to early age cracking in CRCP. The microstructural analysis of the ITZ was articulated using the techniques of environmental scanning electron microscopy (ESEM) and electron dispersive x-ray spectroscopy (EDS) to study its morphological characteristics. Fourier transform infrared spectroscopy (FTIR) was used to identify the corrosion products at the interface.

Non-Corroded Rebar Experiments

The partially corroded rebar used in this experiment is shown in Figure 30.

Figure 30. Partially corroded rebar used in this experiment.

Mix Proportions

The selection of a good concrete mix proportion is essential for the achievement of a balance between economy, placement requirements, durability, density, appearance and strength of the concrete mix. The bulk specific gravity and absorption capacity of the materials used in this research are shown in Table 5.

Table 5. Bulk specific gravity and absorption capacity of materials.

Material	BSG* (SSD)	AC** (%)	Description
Cement	3.15	NA	Type I/II
Water	1	NA	
Rock	2.65	2	Estimate, Crushed LS
Sand	2.6	1	Estimate, Natural Sand
* BSG = Bulk Specific Gravity. **LS=Limestone ** AC = Absorption Capacity.			

The batch weights were calculated for the preparation of 54 specimens for each experimental run. Table 6 shows the batch weights per cubic feet for the w/c ratios of 0.40, 0.45 and 0.50.

Table 6. Batch Weights per cubic feet (lbs) for the w/c of 0.40, 0.45 and 0.50 for non-corroded rebar at 77°F rebar temperature experiments.

w/c Ratio	Slump (in)	Materials	Batch weight per cu. Ft (lbs)
0.40	2	Cement, lb.	32.55
		Water, lb	14.47
		Rock, lb	127.37
		Sand, lb	80.33
0.45	2	Cement, lb.	32.55
		Water, lb	16.01
		Rock, lb	119.33
		Sand, lb	178.64
0.50	1.5	Cement, lb.	32.55
		Water, lb	17.63
		Rock, lb	119.33
		Sand, lb	176.96

These w/c ratios were chosen to provide a wide strength rate as used in the construction of Portland cement concrete (PCC) pavements. The w/c ratio chosen for the construction purpose is optimized to achieve the required strength, durability and permeability requirements.

The values for the moisture conditions for the materials used for the experiment were calculated by considering the weights before and after they were heated in the oven. Moisture conditions for w/c ratio of 0.40, 0.45 and 0.50 are shown below:

Rock: Weight of dish: 0.44 lbs

Weight of sample and the dish (Rs): 3.37 lbs

Oven-dried weight of sample and the dish Rs (Rod): 3.31 lbs

Moisture Content (Rmc) = ((Rs-Rod)/Rod) x100 = 1.00%

Sand: Weight of dish: 0.44 lbs

Weight of sample and the dish (Ss) 3.34 lbs

Oven-dried weight of sample and the dish Ss (Rod): 3.31 lbs

Moisture Content (Smc) = ((Ss-Rod)/Rod) x100 = 0.77%

The pullout test results for specimens cast at 77°F for the 3-day, 10-day and 28 days are shown. Tables 7, 8 and 9 show the results for the 4-in embedment length.

There was a large difference in the values obtained for the 0.45 water to cement ratio for the 8-in embedment length, the experiment was redone and the values obtained were used to compute the final pullout force and shear strength.

Table 7. Measured bond strength magnitudes for non-corroded rebar steels at different w/c ratios after 3days at 77°F rebar temperature, 4-in Embedment.

w/c	Embedment Length (in)	Actual Embedment Length (in)	Maximum Pullout Force (lbf)	Pullout Force (lbf)	Shear stress(psi)	Extension at Peak Load (in)	Extension (in)
0.40	4	5	8770	7613	702	0.324	0.493
0.40	4	4.2	6456			0.663	
0.45	4	4.5	6620	4614	505	0.742	0.573
0.45	4	3.2	2608			0.404	
0.50	4	4	5490	4866	471	0.681	0.568
0.50	4	4.7	4242			0.454	

Table 8. Measured bond strength magnitudes for non-corroded rebar steels at different w/c ratios after 10 days at 77°F rebar temperature, 4-in Embedment.

w/c	Embedment Length (in)	Actual Embedment Length (in)	Maximum Pullout Force (lbf)	Pullout Force (lbf)	Shear stress(psi)	Extension at Peak Load (in)	Extension (in)
0.40	4	4.3	7398	9162	831	0.202	0.246
0.40	4	5	10926			0.290	
0.45	4	5	6915	7127	668	0.348	0.308
0.45	4	4	7339			0.268	
0.50	4	4.5	7420	7527	635	0.172	0.171
0.50	4	5.5	7634			0.169	

Table 9. Measured bond strength magnitudes for non-corroded rebar steels at different w/c ratios after 28 days at 77°F rebar temperature, 4-in Embedment.

w/c	Embedment Length (in)	Actual Embedment Length (in)	Maximum Pullout Force (lbf)	Pullout Force (lbf)	Shear stress(psi)	Extension at Peak Load (in)	Extension (in)
0.40	4	4	7038	7653	787	0.197	0.185
0.40	4	4.2	8268			0.172	
0.45	4	3.5	3786	6181	652	0.120	0.151
0.45	4	4.5	8577			0.181	
0.50	4	4.8	8413	5876	627	0.180	0.135
0.50	4	3.1	3340			0.089	

Tables 10, 11 and 12 shows the results for the 8-in embedment length.

Table 10. Measured bond strength magnitudes for non-corroded rebar steels at different w/c ratios after 3days at 77°F rebar temperature, 8-in Embedment.

w/c	Embedment Length (in)	Actual Embedment Length (in)	Maximum Pullout Force (lbf)	Average Pullout Force (lbf)	Shear stress(psi)	Extension at Peak Load (in)	Average Extension (in)
0.40	8	8	9323	9726	515	0.313	0.334
0.40	8	8	10130			0.355	
0.45	8	8	6953	7402	392	0.520	0.643
0.45	8	8	7852			0.766	
0.50	8	8	7866	6639	352	1.248	0.935
0.50	8	8	5412			0.622	

Table 11. Measured bond strength magnitudes for non-corroded rebar steels at different w/c ratios after 10 days at 77°F rebar temperature, 8-in Embedment.

w/c	Embedment Length (in)	Actual Embedment Length (in)	Maximum Pullout Force (lbf)	Average Pullout Force (lbf)	Shear stress(psi)	Extension at Peak Load (in)	Average Extension (in)
0.40	8	8	11587	10296	546	0.190	0.205
0.40	8	8	9004			0.219	
0.45	8	8	5584	5884	312	0.227	0.208
0.45	8	8	6183			0.189	
0.50	8	8	5613	5730	304	0.151	0.185
0.50	8	8	5846			0.218	

Table 12. Measured bond strength magnitudes for non-corroded rebar steels at different w/c ratios after 28 days at 77°F rebar temperature, 8-in Embedment.

w/c	Embedment Length (in)	Actual Embedment Length (in)	Maximum Pullout Force (lbf)	Average Pullout Force (lbf)	Shear stress(psi)	Extension at Peak Load (in)	Average Extension (in)
0.40	8	8	10745	10970	582	0.235	0.397
0.40	8	8	11190			0.558	
0.45	8	8	8945	9463	502	0.208	0.210
0.45	8	8	9981			0.212	
0.50	8	8	5133	5424	288	0.170	0.155
0.50	8	8	5715			0.139	

Failure Modes

The failure mode experienced during the pullout process was pullout failure as shown in Figure 31. Failure occurred along the length of the rebar.

Figure 31. Pullout failure mode.

The graphical results for the pullout tests at 77^oF for the 8-in and 4-in embedment lengths are shown in Appendix A. These represent the 0.40, 0.45 and 0.50 water to cement ratio. The ESEM micrographs for the w/c ratios of 0.40, 0.45 and 0.50 at 77^oF for the 8-in embedment length are shown in Figures 32-34.

Presence of porosity on a sample with w/c of 0.40 after 3 days is indicated in Figure 32 (a). Porous cement is shown in Figure 32 (b) at a higher magnification. Figure 32 (c, d) shows ITZ for cement-aggregate and close vicinity of multiple aggregates that facilitates crack bridging from one aggregate to the next (Figure 32 (c)). High magnification of one of the aggregates demonstrates high probability that cracking could start at the aggregate ITZ (Figure 32 (d)).

ESEM image for the 28 days set samples show extensive cracking both at the porous and compact region (Figure 32 (e, f)). Higher water to cement ratio appears to have resulted in the formation of more porous concrete (Figure 33 (a-e)). It appears that the aggregate/cement ITZ is larger in length with more extensive porous region (Figure 33 (a-e)). The presence of coarse aggregates within the interfacial zone show clustering of the cement grains with marked differences in paste density with the structure of the paste between the aggregate grains being

significantly less dense than regions farther away (Figure 32 and 33(d)). Crack bridging was also

seen in samples prepared with w/c ratio of 0.45 (Figure 33 (e)). When w/c was increased to 0.50,

the extent of porous ITZ region was increased to 1 mm compared to 30μm in a normal case.

(Figure 34 (e) Figure 34 (c) and 34 (e) shows that crack propagation takes place along the rebar

length and this is in agreement with field observations.
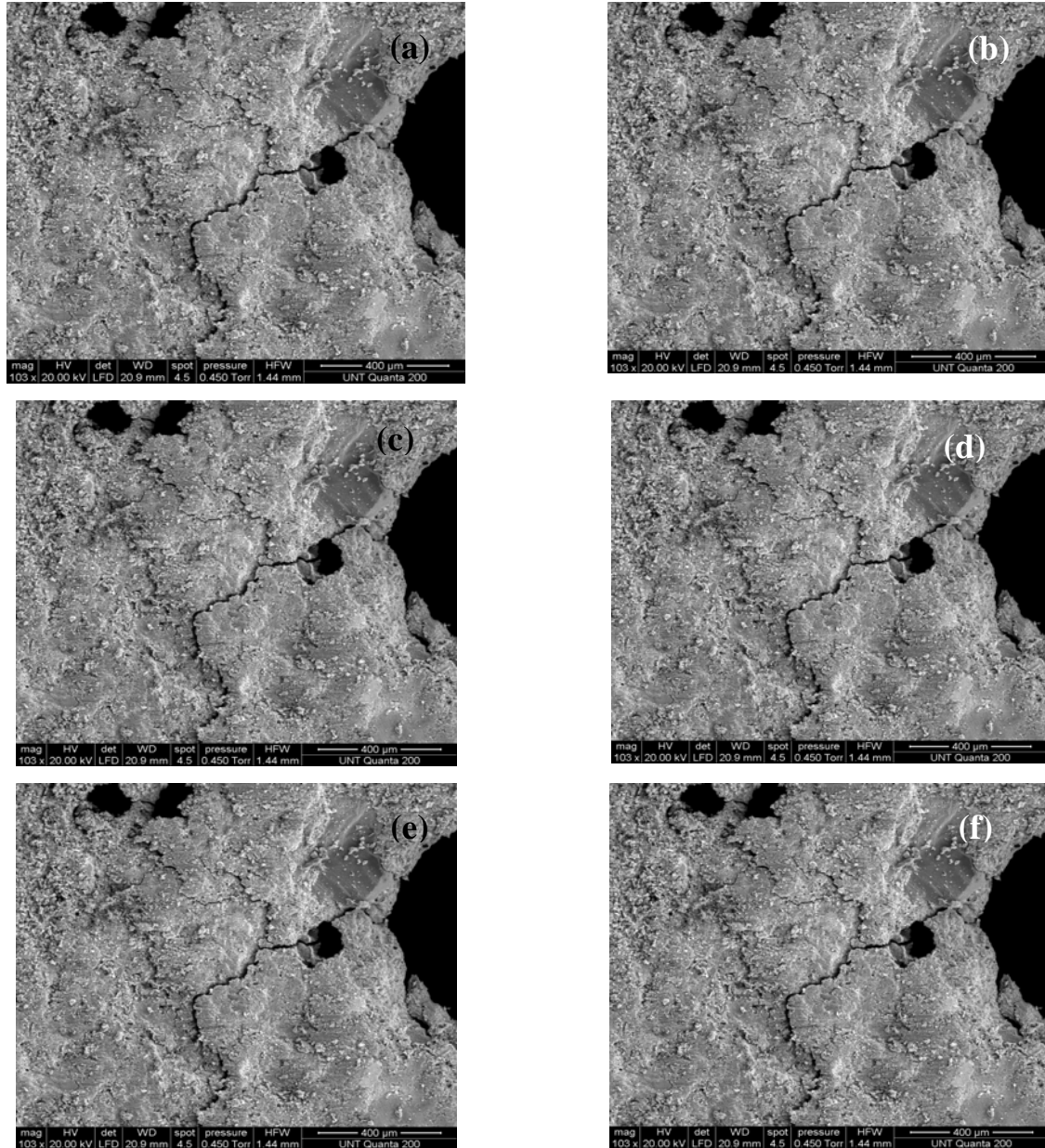
Figure 32. ESEM micrographs for the ITZ for non-corroded rebar steels at 77°F for w/c 0.40
after 3 days (a,b), 10 days (c,d), 28 days (e,f).
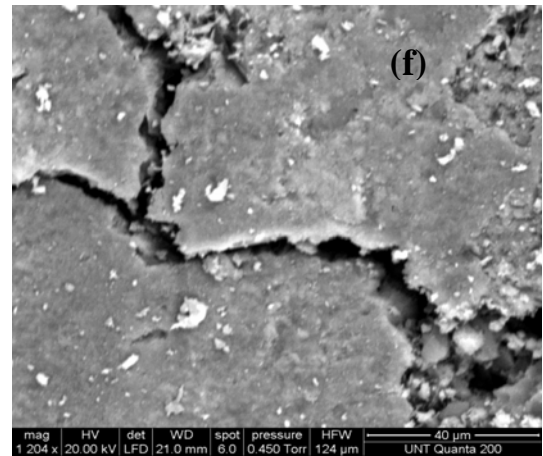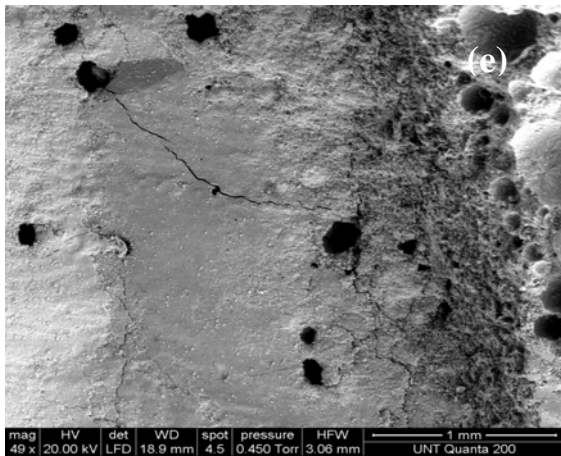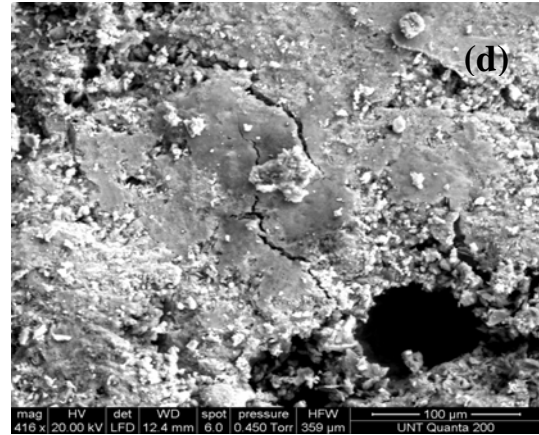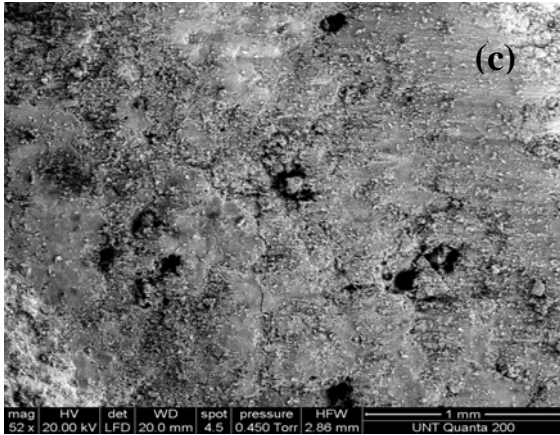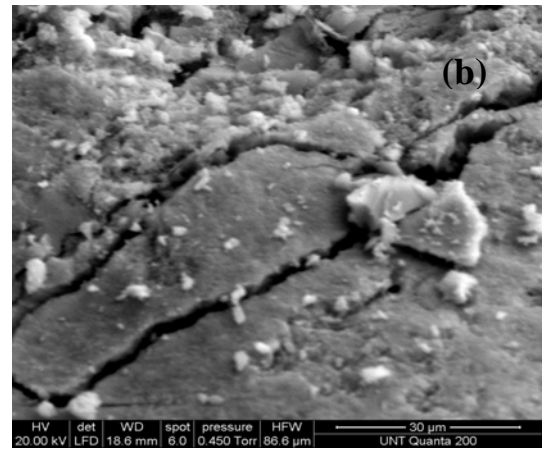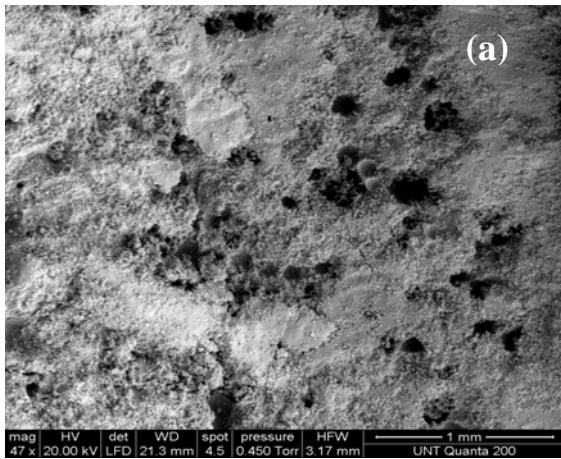
Figure 33. ESEM micrographs for the ITZ for non-corroded rebar steels at 77°F for w/c ratio
0.45 after 3 days (a,b), 10 days (c,d), 28 days (e,f).

Figure 34. ESEM micrographs for the ITZ for non-corroded rebar steels at 77°F for w/c ratio 0.50 after 3 days (a,b), 10 days (c,d), 28 days (e,f).

The second set of experiments involved the heating of the rebars for 4 hours at 252°F and

immediately embedding them in the concrete molds. This simulated casting in hot summer conditions. In doing this, the effect of using hot rebars during the CRCP construction process was determined. The moisture conditions used for the casting of specimens for the 0.40, 0.45 and 0.50 are shown below.

Rock: Weight of the dish: 0.90 lbs

      Weight of the sample and the dish (Rs):   3.55 lbs

      Oven-dried weight of sample and the dish Rs (Rod) 3.50 lbs

      Moisture Content (Rmc) = ((Rs-Rod)/Rod) x 100   1.43 %

Sand: Weight of the dish: 0.90 lbs

      Weight of the sample and the dish (Rs):   2.90 lbs

      Oven-dried weight of sample and the dish Rs (Rod) 2.80 lbs

      Moisture Content (Rmc) = ((Rs-Rod)/Rod) x 100   3.57 %

Table 13 shows the adjusted batch weights.

Table 13. Adjusted batch weights per cubic feet (lbs) for the w/c of 0.40, 0.45 and 0.50 for non-corroded rebar at 252$^{\text{o}}$F rebar temperature experiments.

W/C Ratio	Slump (in)	Material	Batch weight per cu. Ft (lbs)
0.40	2	Rock, lb	129.19
		Sand, lb	83.14
		Water, lb	11.04
		Cement, lb	32.55
0.45	2	Rock, lb	121
		Sand, lb	81.39
		Water, lb	12.71
		Cement, lb	32.55
0.50	1.5	Rock, lb	121
		Sand, lb	79.65
		Water, lb	14.25
		Cement, lb	32.55

The pullout test results for the bond strength measurements for the non-corroded rebar steels at different w/c after 3 days, 10 days and 28 days for the 252$^{\text{o}}$F rebar temperature and 4-in

and 8-in embedment lengths are shown in Tables 14, 15, 16, 17, 18 and 19.

Table 14. Measured bond strength magnitudes for non-corroded rebar steels at different w/c ratios after 3 days at 252°F rebar temperature, 4-in Embedment.

w/c	Embedment Length (in)	Actual Embedment Length (in)	Maximum Pullout Force (lbf)	Pullout Force (lbf)	Shear stress(psi)	Extension at Peak Load (in)	Extension (in)
0.40	4	4	4209	2747	323	0.118	0.159
0.40	4	3.2	1286			0.041	
0.45	4	5	3868	4684	378	0.104	0.125
0.45	4	5.5	5500			0.145	
0.50	4	4	3508	4484	475	0.102	0.152
0.50	4	4	5460			0.155	

Table 15. Measured bond strength magnitudes for non-corroded rebar steels at different w/c ratios after 10 days at 252°F rebar temperature, 4-in Embedment.

w/c	Embedment Length (in)	Actual Embedment Length (in)	Maximum Pullout Force (lbf)	Average Pullout Force (lbf)	Shear stress(psi)	Extension at Peak Load (in)	Average Extension (in)
0.40	4	3.8	5012	5877	639	0.135	0.169
0.40	4	4	6743			0.204	
0.45	4	4	5559	4522	492	0.208	0.154
0.45	4	3.8	3485			0.099	
0.50	4	4	4029	4028	427	0.124	0.148
0.50	4	4	4026			0.171	

Table 16. Measured bond strength magnitudes for non-corroded rebar steels at different w/c ratios after 28 days at 252°F rebar temperature, 4-in Embedment.

w/c	Embedment Length (in)	Actual Embedment Length (in)	Maximum Pullout Force (lbf)	Average Pullout Force (lbf)	Shear stress(psi)	Extension at Peak Load (in)	Average Extension (in)
0.40	4	4	10104	9609	1019	0.271	0.261
0.40	4	4	9114			0.250	
0.45	4	3	2135	4398	497	0.075	0.143
0.45	4	4.5	6660			0.211	
0.50	4	4	3989	3280	356	0.126	0.117
0.50	4	3.8	2571			0.107	

Table 17. Measured bond strength magnitudes for non-corroded rebar steels at different w/c ratios after 3 days at 252°F rebar temperature, 8-in Embedment.

w/c	Embedment Length (in)	Actual Embedment Length (in)	Maximum Pullout Force (lbf)	Average Pullout Force (lbf)	Shear stress(psi)	Extension at Peak Load (in)	Average Extension (in)
0.40	8	8	1618	4924	261	0.051	0.144
0.40	8	8	8230			0.236	
0.45	8	8	4840	4879	258	0.161	0.157
0.45	8	8	4918			0.153	
0.50	8	8	4179	5213	276	0.199	0.204
0.50	8	8	6246			0.208	

Table 18. Test Measured bond strength magnitudes for non-corroded rebar steels at different w/c ratios after 10 days at 252°F rebar temperature, 8-in Embedment.

w/c	Embedment Length (in)	Actual Embedment Length (in)	Maximum Pullout Force (lbf)	Average Pullout Force (lbf)	Shear stress(psi)	Extension at Peak Load (in)	Average Extension (in)
0.40	8	8	5379	7021	372	0.143	0.227
0.40	8	8	8663			0.310	
0.45	8	8	6343	5475	290	0.215	0.191
0.45	8	8	4606			0.167	
0.50	8	8	3938	3623	192	0.151	0.126
0.50	8	8	3309			0.100	

Table 19. Measured bond strength magnitudes for non-corroded rebar steels at different w/c ratios after 28 days at 252°F rebar temperature, 8-in Embedment.

w/c	Embedment Length (in)	Actual Embedment Length (in)	Maximum Pullout Force (lbf)	Average Pullout Force (lbf)	Shear stress(psi)	Extension at Peak Load (in)	Average Extension (in)
0.40	8	8	8037	8193	434	0.218	0.211
0.40	8	8	8348			0.205	
0.45	8	8	7897	6357	337	0.265	0.224
0.45	8	8	4816			0.183	
0.50	8	8	4848	4208	223	0.162	0.135
0.50	8	8	3569			0.108	

The ESEM micrographs for the 252°F rebar temperature condition for the w/c ratios of

0.40, 0.45 and 0.50 are show in the Figures 35-37. Higher rebar temperature (252°F) led to the

formation of highly powdery concrete particles as shown in Figure 35 (b). Lack of solid bond formation between aggregates rich region near the rebar is shown in Figure 35 (e, f). These poorly bonded aggregate particles add a new level of concrete heterogeneity and disrupt the packing of cement particles locally at the cement paste aggregate interface.

Microcrack formation along the rebar length is also shown in Figure 35 (e, f). Increased w/c ratio to 0.45 made the concrete even more porous (Figure 36 (a, b). Figure 36 (c) shows aggregate particles that have not participated in the bonding and are relatively loosely attached to a highly porous region. The porous microstructure phenomenon was also observed by R. Zimbelman (1999) and P. Simenow et al., (1999). Increase in porosity leads to a great number of sites lacking binding material at the interface. Extensive cracking is observed in severely porous regions as shown in Figure 36 (a, c, e, and f). Further increased w/c ratio intensified both porosity and cracking (Figure 37 (a – f). Figure 37 (e) shows a region highly concentrated with fraction of mm size voids possibly indicating fast evaporation and bubble formation thus preventing strong bond formation between rebar and concrete.

Microcrack formation forms inside void cups as shown in Figure 37 (f). Some of the voids are μm in diameter whereas others are in mm range (Figure 37 (f)). G. Prokopksi and B. Langier (2000) also found that as the w/c ratio increased; the porosity in the ITZ is also increased, resulting in the initiation and development of microcracks in this zone. The existence of these cracks are detrimental to the concrete bond strength because when they coalesce and reach the surface, they allow for the chloride ingress into the concrete structure which will ultimately result in the formation of expansive corrosion products (rust) which occupy several times the volume of the original steel consumed.
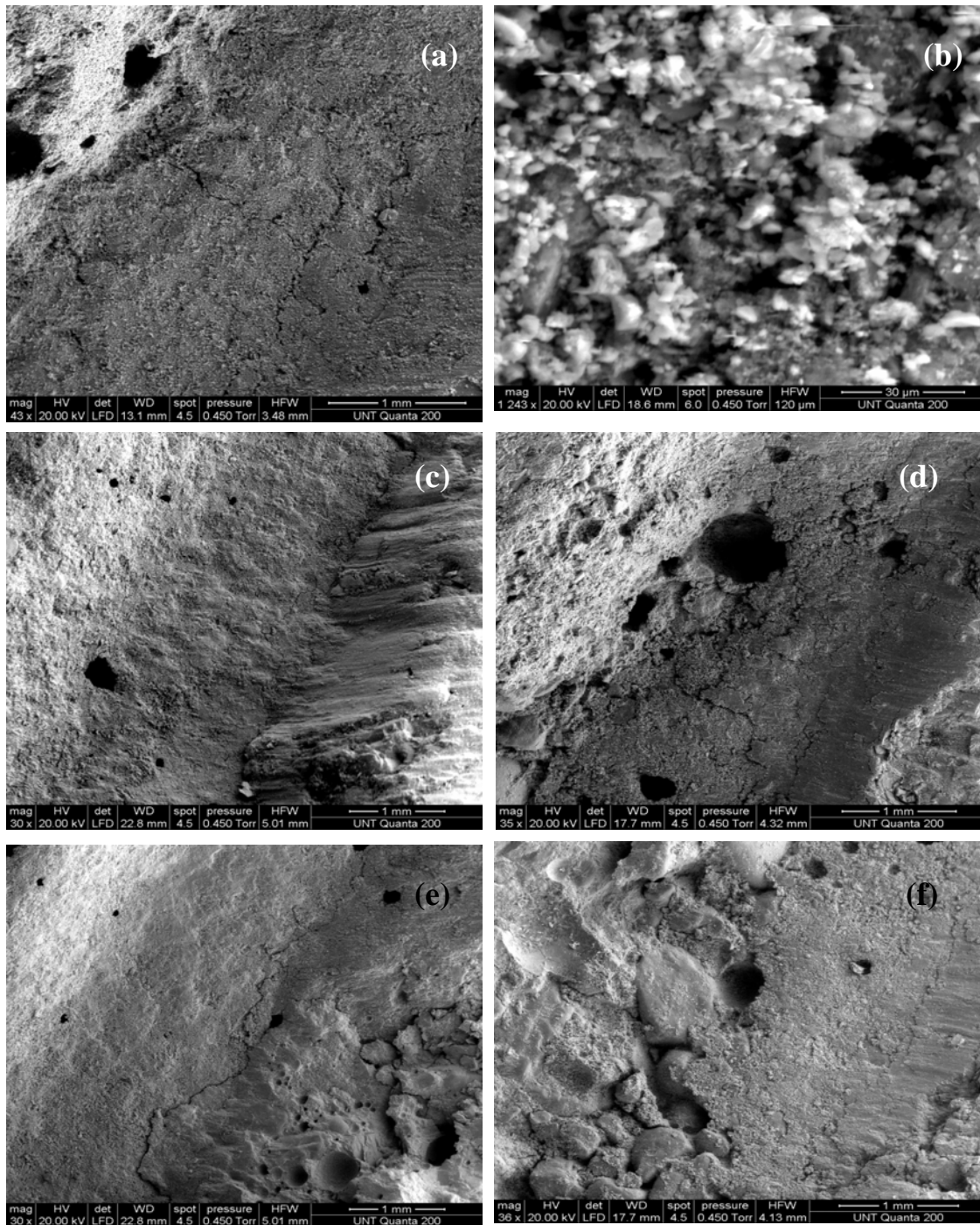
Figure 35. ESEM micrographs for the ITZ for non-corroded rebar steels at 252°F for w/c ratio 0.40 after 3 days (a,b), 10 days (c,d), 28 days (e,f).
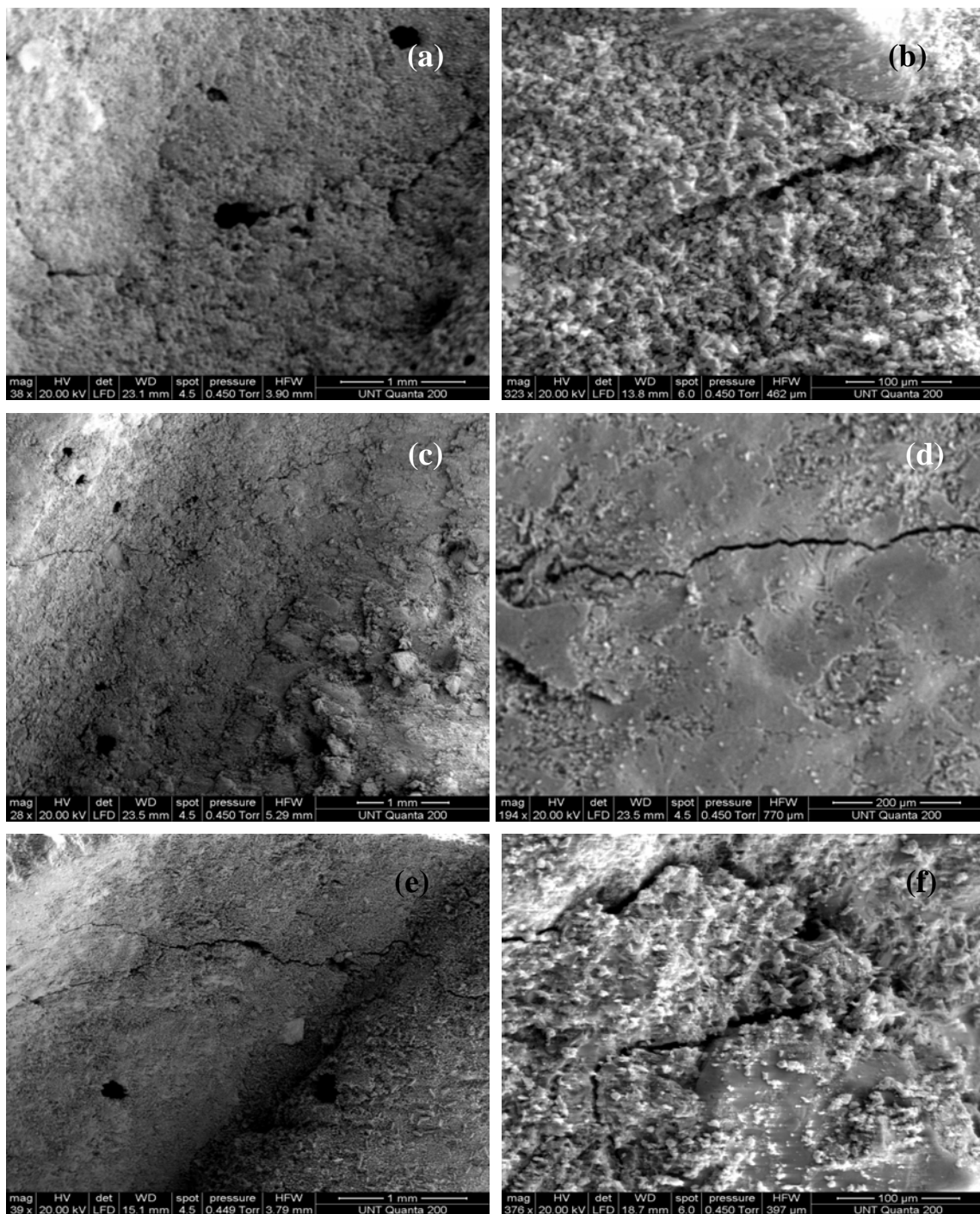
Figure 36. ESEM micrographs for the ITZ for non-corroded rebar steels at 252°F for w/c ratio 0.45 after 3 days (a,b), 10 days (c,d), 28 days (e,f).
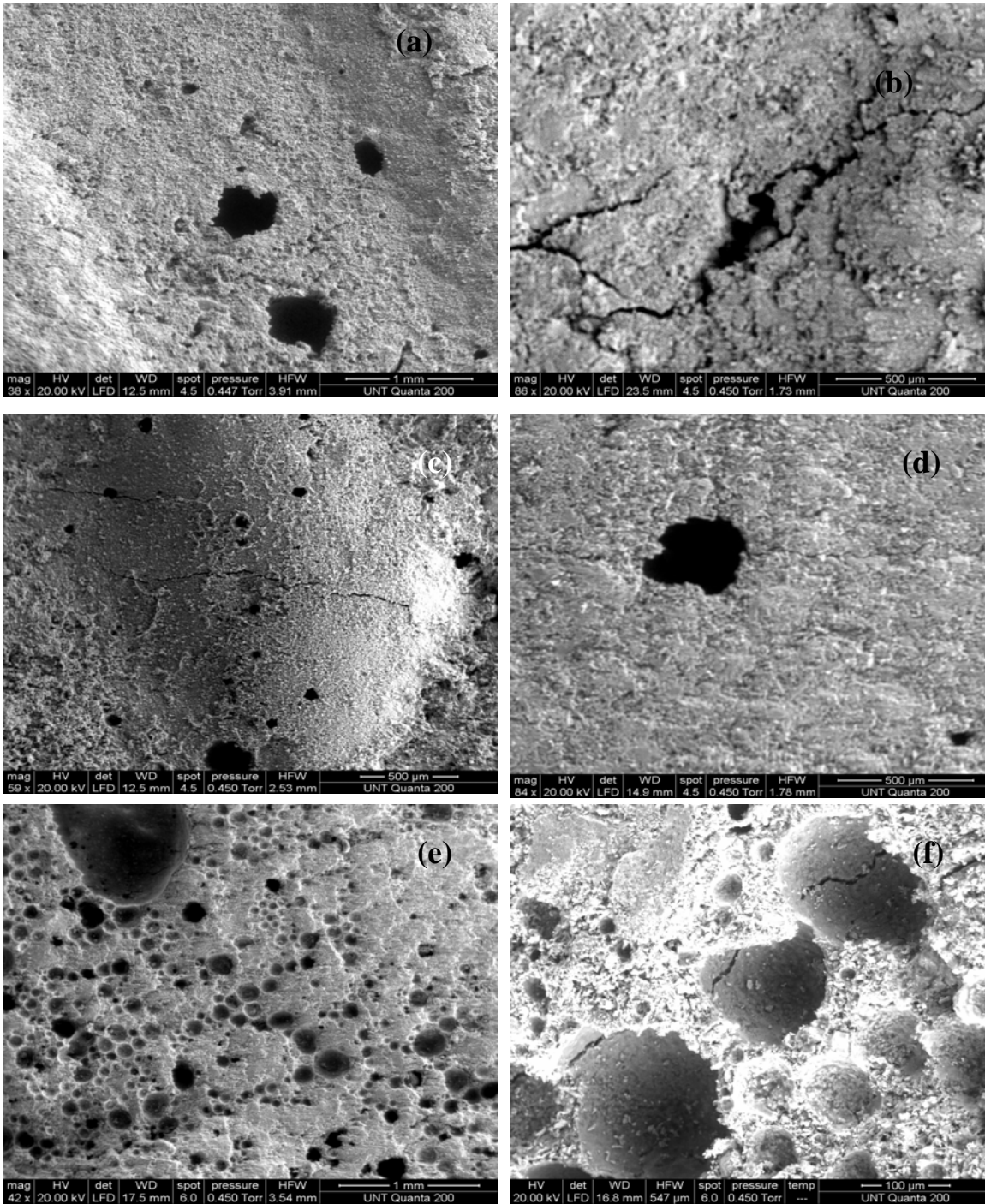
Figure 37. ESEM micrographs for the ITZ for non-corroded rebar steels at 252°F for w/c ratio 0.50 after 3 days (a,b), 10 days (c,d), 28 days (e,f).

The graphical results representing the 0.40, 0.45 and 0.50 water to cement ratios for the

pullout tests for the 8-in and 4-in embedment lengths are shown in Appendix A.

The third set of experiments involved the cooling of the rebars for 4 hours at 14°F and immediately embedding them in the concrete molds. This simulated casting in cold winter conditions allowing for the determination of the effect of using cold rebars during the CRCP construction process. The moisture conditions used for the casting of specimens for the 0.40, 0.45 and 0.50 are shown below.

Rock: Weight of the dish: 0.90 lbs

  Weight of the sample and the dish (Rs):   3.55 lbs

  Oven-dried weight of sample and the dish Rs (Rod) 3.50 lbs

  Moisture Content (Rmc) = ((Rs-Rod)/Rod) x 100 1.43 %

Sand: Weight of the dish: 0.90 lbs

  Weight of the sample and the dish (Rs):   3.55 lbs

  Oven-dried weight of sample and the dish Rs (Rod) 3.50 lbs

  Moisture Content (Rmc) = ((Rs-Rod)/Rod) x 100 4.41 %

Table 20 shows the adjusted batch weights for 14°F rebar temperature for the w/c ratios of 0.40, 0.45, and 0.50.

Table 20. Adjusted batch weights per cubic feet (lbs) for the w/c of 0.40, 0.45 and 0.50 for non-corroded rebar at 14°F rebar temperature experiments.

W/C Ratio	Slump (in)	Material	Batch weight per cu. Ft (lbs)
0.40	2	Rock, lb	129.20
		Sand, lb	83.88
		Water, lb	12.12
		Cement, lb	32.55
0.45	2	Rock, lb	121.04
		Sand, lb	82.10
		Water, lb	14.02
		Cement, lb	32.55
0.50	1.5	Rock, lb	121.04
		Sand, lb	80.36
		Water, lb	15.70
		Cement, lb	32.55

The pullout test results for the bond strength measurements for the non-corroded rebar steels at different w/c after 3 days, 10 days and 28 days for the 14°F rebar temperature and 4-in and 8-in embedment lengths are shown in Tables 21, 22, 23, 24, 25, and 26.

Table 21. Measured bond strength magnitudes for non-corroded rebar steels at different w/c ratios after 3 days at 14°F rebar temperature, 4-in Embedment.

w/c	Embedment Length (in)	Actual Embedment Length (in)	Maximum Pullout Force (lbf)	Pullout Force (lbf)	Shear stress(psi)	Extension at Peak Load (in)	Extension (in)
0.40	4	3	2290	4848	526	0.131	0.147
0.40	4	4.8	7406			0.163	
0.45	4	4	4877	5424	483	0.123	0.142
0.45	4	5.5	5970			0.161	
0.50	4	6	9468	6849	460	0.192	0.167
0.50	4	6.6	4230			0.139	

Table 22. Measured bond strength magnitudes for non-corroded rebar steels at different w/c ratios after 10 days at 14°F rebar temperature, 4-in Embedment.

w/c	Embedment Length (in)	Actual Embedment Length (in)	Maximum Pullout Force (lbf)	Pullout Force (lbf)	Shear stress(psi)	Extension at Peak Load (in)	Extension (in)
0.40	4	5.7	9065	6744	657	0.207	0.157
0.40	4	3	4424			0.107	
0.45	4	4	4437	3863	467	0.095	0.110
0.45	4	3	3290			0.125	
0.50	4	3.2	2743	3507	457	0.0911	0.179
0.50	4	3.3	4271			0.1790	

Table 23. Measured bond strength magnitudes for non-corroded rebar steels at different w/c ratios after 28 days at 14°F rebar temperature, 4-in Embedment.

w/c	Embedment Length (in)	Actual Embedment Length (in)	Maximum Pullout Force (lbf)	Average Pullout Force (lbf)	Shear stress(psi)	Extension at Peak Load (in)	Average Extension (in)
0.40	4	4	5798	5751	610	0.147	0.152
0.40	4	4	5704			0.156	
0.45	4	2.7	1604	2529	363	0.035	0.056
0.45	4	3.2	3455			0.077	
0.50	4	4	2929	2445	276	0.048	0.0484
0.50	4	3.5	1960			0.049	

Table 24. Measured bond strength magnitudes for non-corroded rebar steels at different w/c ratios after 3 days at 14°F rebar temperature, 8-in Embedment.

w/c	Embedment Length (in)	Actual Embedment Length (in)	Maximum Pullout Force (lbf)	Average Pullout Force (lbf)	Shear stress(psi)	Extension at Peak Load (in)	Average Extension (in)
0.40	8	8	6955	5644	299	0.212	0.140
0.40	8	8	4332			0.067	
0.45	8	8	5369	6457	342	0.164	0.215
0.45	8	8	7546			0.266	
0.50	8	8	9750	6541	347	0.214	0.330
0.50	8	8	3332			0.116	

Table 25. Measured bond strength magnitudes for non-corroded rebar steels at different w/c ratios after 10 days at 14°F rebar temperature, 8-in Embedment.

w/c	Embedment Length (in)	Actual Embedment Length (in)	Maximum Pullout Force (lbf)	Average Pullout Force (lbf)	Shear stress(psi)	Extension at Peak Load (in)	Average Extension (in)
0.40	8	8	11312.75	10459	554	0.249	0.228
0.40	8	8	9605.36			0.207	
0.45	8	8	12488.59	8303	440	0.342	0.264
0.45	8	8	4118.12			0.186	
0.50	8	8	4899.32	8218	436	0.135	0.156
0.50	8	8	11538.25			0.176	

Table 26. Measured bond strength magnitudes for non-corroded rebar steels at different w/c ratios after 28 days at 14°F rebar temperature, 8-in Embedment.

w/c	Embedment Length (in)	Actual Embedment Length (in)	Maximum Pullout Force (lbf)	Average Pullout Force (lbf)	Shear stress(psi)	Extension at Peak Load (in)	Average Extension (in)
0.40	8	8	12332	12204	647	0.197	0.251
0.40	8	8	12075			0.305	
0.45	8	8	14550	12102	642	0.306	0.253
0.45	8	8	9653			0.200	
0.50	8	8	5629	3816	202	0.145	0.115
0.50	8	8	2002			0.084	

The ESEM micrographs for the 14°F rebar temperature condition for the w/c ratios of

0.40, 0.45 and 0.50 are show in the Figures 38-40. Low rebar temperature is as harmful as high

rebar temperature as weak bonding form between rebar and concrete. Figure 38 (a-f) demonstrates incomplete inclusion of the aggregates into the matrix of concrete. Incomplete bonding is clearly shown in Figure 38 (a). Extensive cracking and porosity is shown in Figure 38 (b, c, d, and f). Increased w/c ratio to 0.45 for rebar temperature at 14^oF before cement pouring showed both weak aggregate bonding and porosity (Figure 39 (b)), powdery interface (Figure 39 (d) and extensive cracking as shown in Figure 39 (b, d, and f). An interesting feature is shown in Figure 40 (d), the increase of the ITZ interface to more than $200\mu m$. Generally, it is observed that at both temperature extremes (252^oF and 14^oF) the extent of ITZ especially for aggregate to concrete transition zone has increased in some cases by three orders of magnitude from μm to mm range.

Figure 38. ESEM micrographs for the ITZ for non-corroded rebar steels at 14°F for w/c ratio 0.40 after 3 days (a,b), 10 days (c,d), 28 days (e,f).
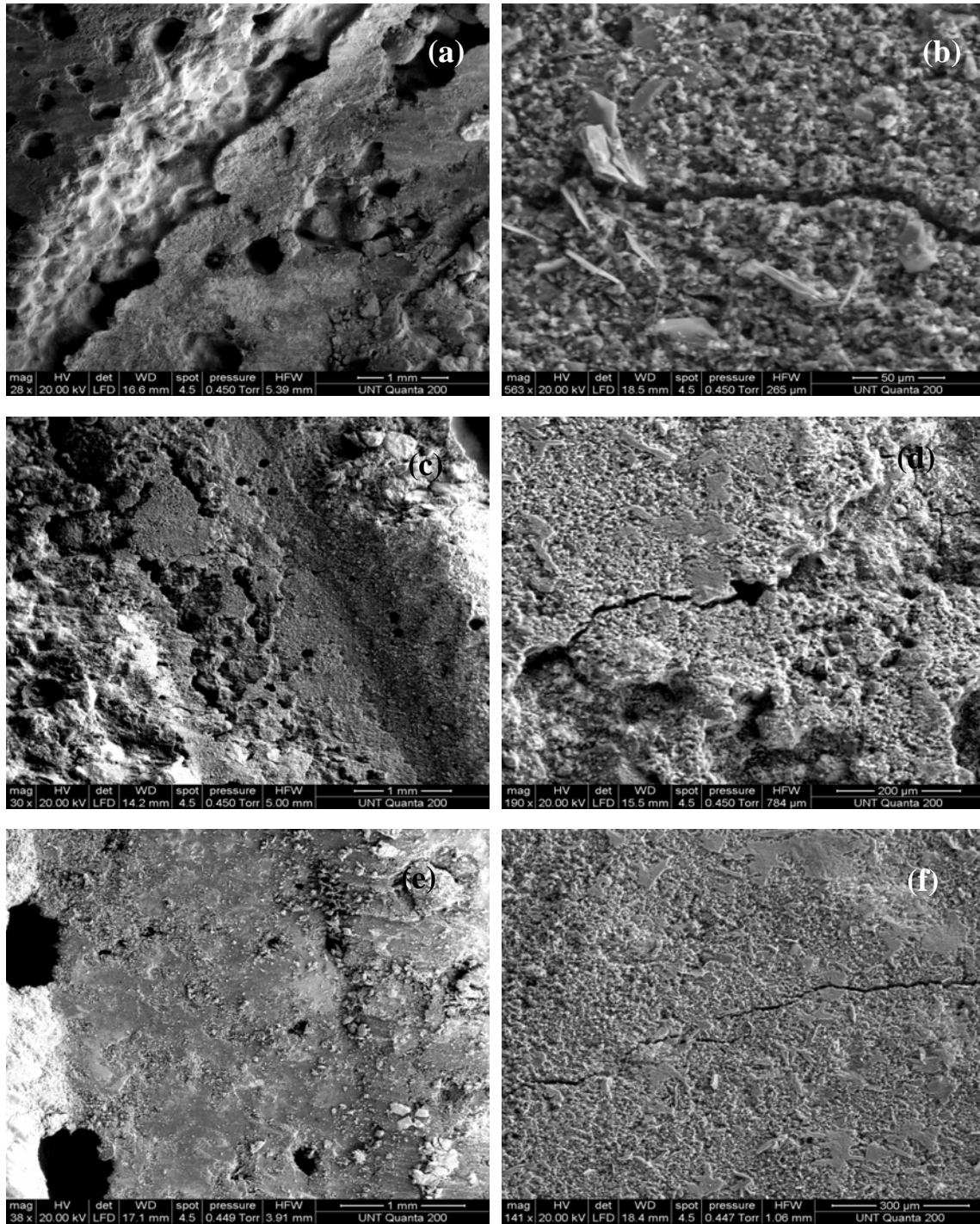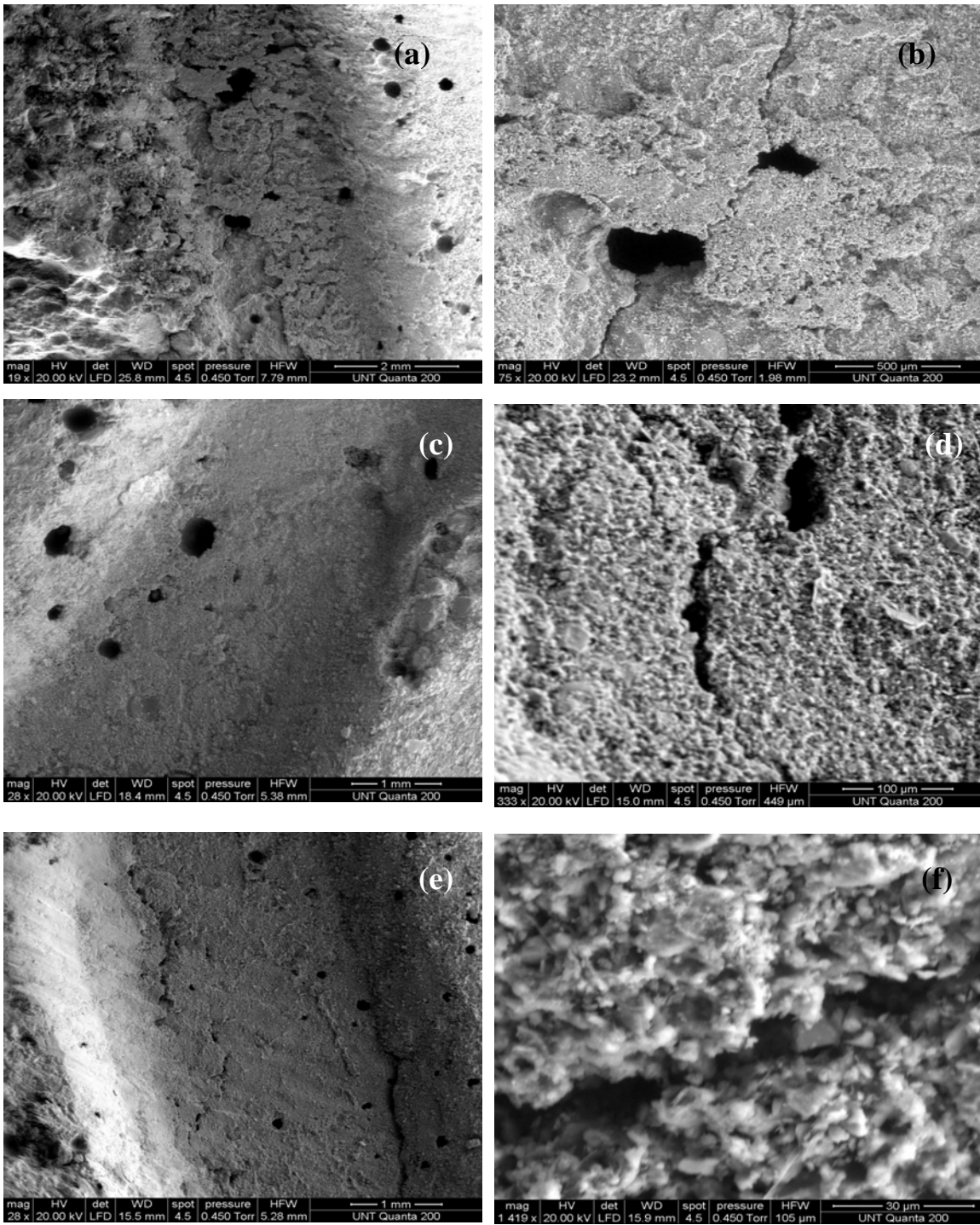
Figure 39. ESEM micrographs for the ITZ for non-corroded rebar steels at 14°F for w/c ratio 0.45 after 3 days (a,b), 10 days (c,d), 28 days (e,f).
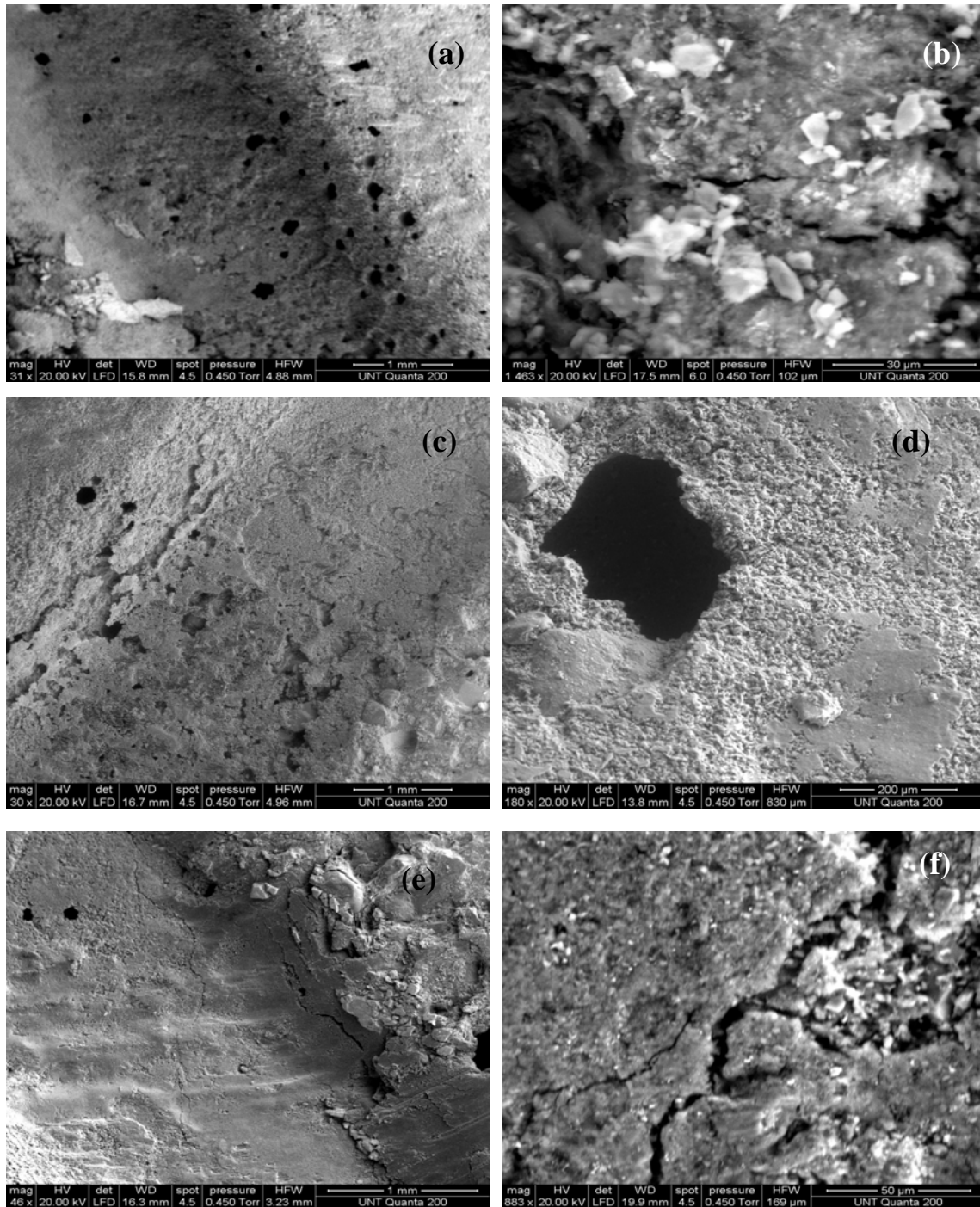
Figure 40. ESEM micrographs for the ITZ for non-corroded rebar steels at 14°F for w/c ratio 0.50 after 3 days (a,b), 10 days (c,d), 28 days (e,f).

Table 27 and Table 28 show all the results for measured bond strength magnitudes for the non-corroded rebar steel.

Table 27. Measured bond strength magnitudes for non-corroded rebar steels at different w/c ratios and rebar temperatures, 8-in Embedment.

w/c	Temp (^{o}F)	Pullout Force (lbf)			Shear Stress (psi)			Extension (in)		
		3day	10day	28day	3day	10day	28day	3day	10day	28day
0.40		5644	10459	12204	299	554	647	0.140	0.228	0.251
0.45	14	6457	8303	12102	342	440	642	0.215	0.264	0.253
0.50		6541	8218	3816	347	436	202	0.330	0.156	0.115
0.40		9726	10296	10970	515	546	582	0.334	0.205	0.397
0.45	77	7402	5884	9463	392	312	502	0.643	0.209	0.210
0.50		6639	5730	5424	352	304	288	0.935	0.185	0.155
0.40		4924	7021	8193	261	372	434	0.144	0.227	0.211
0.45	252	4879	5475	6357	258	290	337	0.157	0.191	0.224
0.50		5213	3623	4208	276	192	223	0.204	0.126	0.135

Table 28. Measured bond strength magnitudes for non-corroded rebar steels at different w/c ratios and rebar temperatures, 4-in Embedment.

w/c	Temp (^{o}F)	Pullout Force (lbf)			Shear Stress (psi)			Extension (in)		
		3day	10day	28day	3day	10day	28day	3day	10day	28day
0.40		4848	6744	5751	526	657	610	0.147	0.157	0.152
0.45	14	5424	3863	2529	483	467	363	0.142	0.110	0.056
0.50		6849	3507	2445	460	457	276	0.167	0.179	0.048
0.40		7613	9162	7653	702	831	787	0.493	0.246	0.185
0.45	77	4614	7127	6181	505	668	652	0.573	0.338	0.151
0.50		4866	7527	5876	471	635	627	0.568	0.171	0.135
0.40		2747	5877	9609	323	639	1019	0.159	0.169	0.261
0.45	252	4684	4522	4398	378	492	497	0.125	0.154	0.143
0.50		4484	4028	3280	475	427	356	0.152	0.148	0.117

Figures 41 and 42 show the pullout test results for the 10-day and 28-day tests respectively. The three-day results have not been graphically represented because sufficient bond strength has not been established at this early age to produce a reliable trend in the bond strength characteristic. Figure 43 however shows the overall picture of all the pullout strength results obtained.
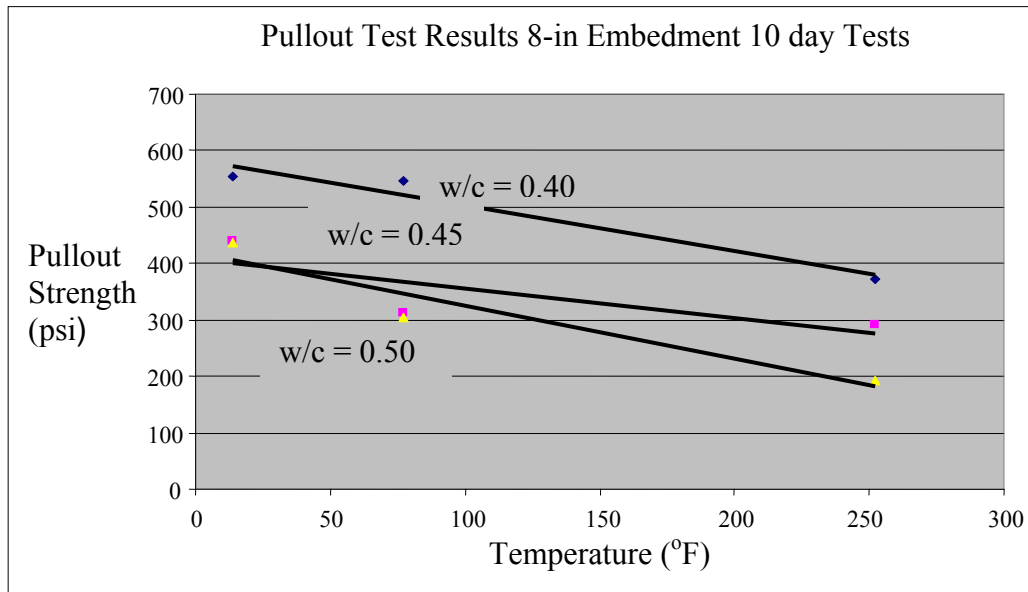
Figure 41. Bond strength vs. rebar temperature pullout test results for non-corroded rebar at 10 days.
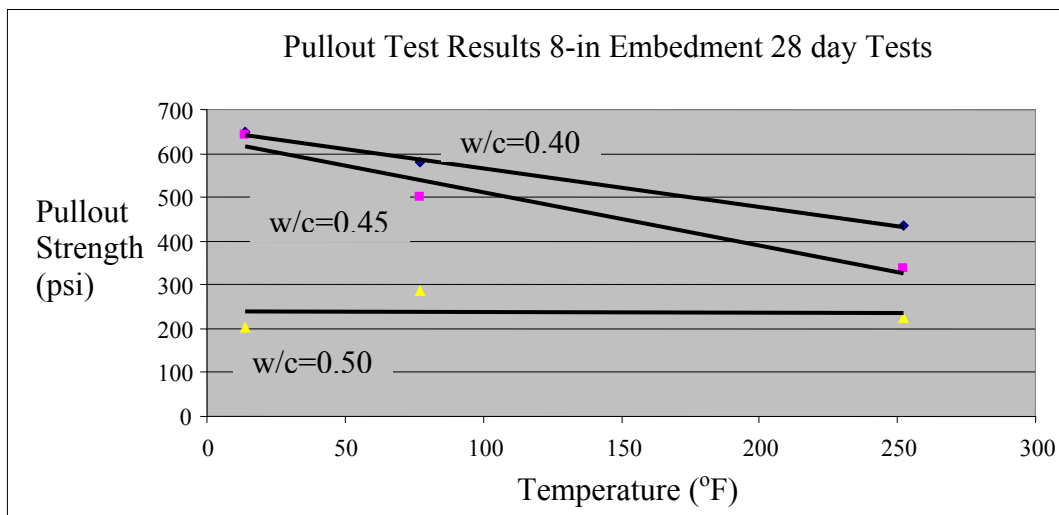
Figure 42. Bond strength vs. rebar temperature pullout test results for non-corroded rebar at 28 days.
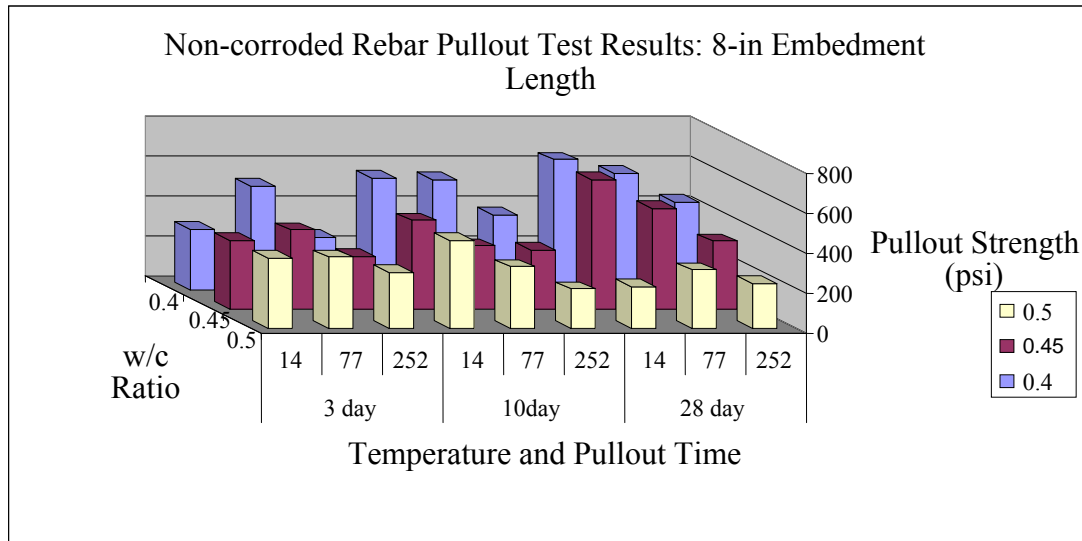
Figure 43. Non-corroded rebar pullout test results 8-in embedment length at different pullout times, temperature and w/c ratios.

Discussion

Due to the variation in the final embedment length of the 4-in embedment length experiments, the 8-in embedment length results were used for the analysis of the parameter effects due to their consistency and repeatability. The scatter in the 0.40-in embedment length pullout results was as a result in the change in the final embedment lengths of the specimens. This variation was caused by the setting of the rebar deeper into the concrete mix soon after the compaction process or the rebar being held higher than the required 4-in embedment during casting.

Rebar Temperature Effects

The results show a reduction in the peak pullout load as the temperature increased for the 10 days and 28 days tests (Figure 41 and 42). Since the rate of hydration is very sensitive to temperature especially during the initial curing stages, Samarai et al. 1993 showed that the higher

the curing temperature the higher the heat release. The high rebar temperature therefore leads to

a rapid buildup of heat on the rebar-concrete interface resulting in the localized evaporation of

water molecules within this region and so a reduction in concrete bond strength.

Several research studies have been undertaken to investigate the effect of elevated

temperatures on bond strength. Katz and Berman (2000) studied the effect of high temperature

on the bond strength between FRP reinforcing bars and concrete. By using a heat jacket around

their concrete specimen, they varied the temperature applied from $20^{o}C$ to $200^{o}C$ and performed

pullout tests to determine the average bond. They found that there was a severe reduction in the

bond strength as the temperature rises. Their experiments also showed a high bond strength

characteristic and a high pullout peak load by using low temperature. Their results are shown in

Table 29. Their experiment was different from what was done in this research study because here,

the rebar was heated and the concrete specimen maintained at room temperature. Nevertheless,

their study gives us an insight on the effect of high temperature on the bond strength because

heating the concrete specimen also causes heat transfer to the rebar through conduction.

Table 29. Bond strength at room temperature and residual bond at $200^{o}C$ (Amnon Katz, Neta Reman 2000).

Rod type	R.T. (20°C)		~130°C		~200°C		
	Peak load (kN)	Average bond (MPa)	Peak load (kN)	Average bond (MPa)	Peak load (kN)	Average bond (MPa)	Residual (%)
CB	31.3	13.2	16.0	6.7	2.6	1.1	8.3
CPH	29.0	12.2	16.0	5.0	3.8	1.7	13.9
CPI	25.6	10.9	11.9	6.7	4.0	1.6	14.7
NG	9.7	4.1	1.8	0.8	1.9	0.8	19.5
STEEL	25.2	10.6	19.3	8.1	16.4	6.9	67.0

Water to Cement Ratio Effects

The bond strength was significantly influenced by the water to cement ratio. The 10 days

and the 28 days shear stress measurements showed that the lower the water to cement ratio the higher the rebar concrete bond strength (Table 27). The 28 days pullout tests for 14^oF rebar temperature showed a relatively higher bond strength magnitude, 647 psi, 642 psi, and 202 psi compared to the 252^oF bond strength magnitudes of 434 psi, 337 psi, and 223 psi for the w/c ratios of 0.40, 0.45 and 0.50 respectively (Figures 41 and 42). The 77^oF rebar temperature bond strength magnitudes at 28 days for the w/c ratios of 0.40, 0.45 and 0.50 were 581 psi, 502 psi and 287 psi respectively (Table 27). The high w/c ratio of 0.50 yielded a low bond strength concrete due to the increase in porosity created during the hydration process (Figure 37 (e, f)). This led to low bond strength between the concrete and rebar interface at high rebar temperature.

Corroded Rebar Experiments

After completion of the non-corroded rebar test procedure, the effect of the corroded rebar on the concrete bond strength and morphological characteristics of the concrete mix and steel rebar were examined. The rebars were corroded using an Atlas CCX 3000 Advanced Cyclic Exposure System Salt Fog Tester for six weeks. The 6000 hours required to expose the rebars to the corrosive environment was not used because of time constraints. The rebars however achieved the level of corrosion acceptable for this experiment. Figure 44 shows the condition of the rebar after removal from the Salt Fog Testing machine.

FTIR measurements were performed on the corroded rebar to identify the corrosion products present prior to casting of the specimens. The most predominant oxide observed was Maghemite (γ-Fe_2O_3) with IR peak wavelengths of 463 cm^{-1} and Goethite (α-FeOOH) with IR peak wavelengths of 875 cm^{-1}. This is shown in Figure 45.

69

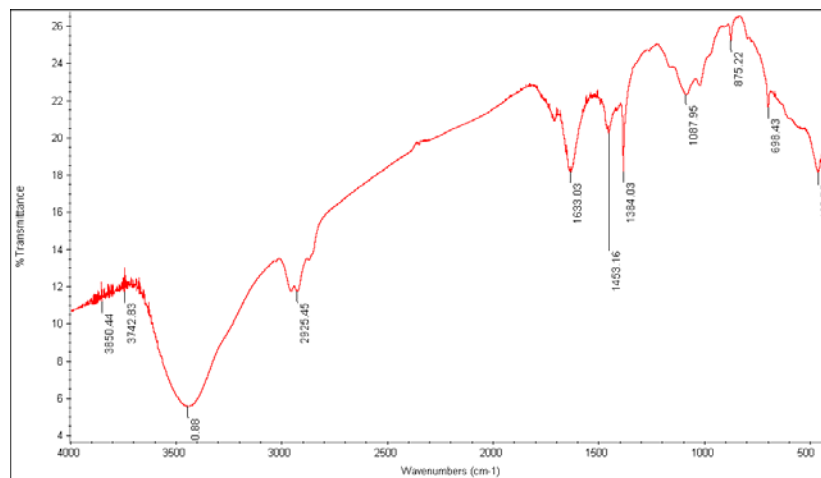Figure 44. Corroded rebar used in this research.

Figure 45. FTIR results of the corroded rebar used in this research.

The corrosion process closely mimicked what would naturally occur in the field when rebar is exposed to corrosion products. Prior to performing the experiments for the non-corroded rebar, (FTIR) was also used to identify the oxides present on the rebar and the results obtained are shown in Figure 46. The IR peak of 1019 cm^{-1} indicated the presence of corrosion products consisting of Lepidocrocite (γ-FeOOH), the 744 cm^{-1} and 877.42cm^{-1} peaks indicated the presence of Goethite (α-FeOOH). From Table 1, the presence of these iron oxides creates tensile stresses on the concrete surrounding the steel reinforcing bar, which can lead to the cracking of the concrete.
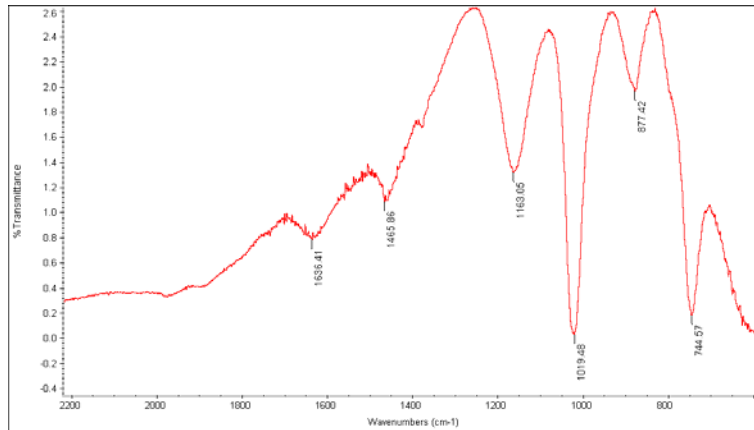
Figure 46. FTIR results of the non-corroded rebar used in this research.

Lepidocrocite (γ-FeOOH) and goethite (α-FeOOH) have a molar volume of 21.3 cm^3/mol Fe and 22.4 cm^3/mol Fe respectively. This is approximately three and 2.15 times the volume ratio of iron.

In order to visualize how the degree of protection is compromised by the corrosion of the rebar, a 0.40-in rebar used in this experiment was cut and examined under the ESEM. A cross-sectional view of the rebar is shown in Figure 47. It shows that the protective oxide layer, which is approximately 20.42μm, is lost due to the corrosion process. The rebar is therefore exposed to deleterious oxides that will greatly influence the rebar-concrete strength.

Figure 47. ESEM picture of corroded rebar.

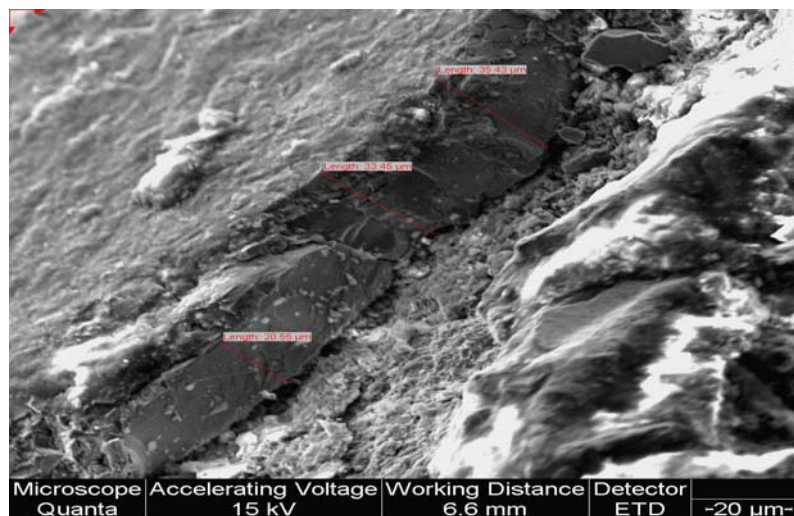*Experimental Process*

For this experiment, the 4-in embedment length specimens were not cast because of the inconsistencies in the final embedment lengths as observed in the non-corroded rebar specimens. Fifty-four specimens were cast with 8-in embedment lengths using w/c ratios of 0.40, 0.45 and 0.50. The rebar temperatures of $14\,^oF$, $77\,^oF$ and $252\,^oF$ were used. Figure 48 shows the specimens prior to demolding.

Figure 48. Specimens with 8-in embedment corroded rebars.

The moisture conditions used for the casting of specimens for the 0.40, 0.45 and 0.50 are shown below.

Rock: Weight of the dish: 0.90 lbs

Weight of the sample and the dish (Rs):   3.55 lbs

Oven-dried weight of sample and the dish Rs (Rod) 3.51 lbs

Moisture Content (Rmc) = ((Rs-Rod)/Rod) x 100   1.11 %

Sand: Weight of the dish: 0.90 lbs

Weight of the sample and the dish (Rs):   3.55 lbs

Oven-dried weight of sample and the dish Rs (Rod) 3.53 lbs

Moisture Content (Rmc) = ((Rs-Rod)/Rod) x 100   0.70 %

Table 30 shows the adjusted batch weights per cubic feet (lbs) for the w/c of 0.40, 0.45 and 0.50

for the corroded rebars at 14°F, 77°F, and 252°F rebar temperature experiments.

Table 30. Adjusted batch weights per cubic feet (lbs) for the w/c of 0.40, 0.45 and 0.50 for corroded rebar at 14°F, 77°F and 252°F rebar temperature experiments.

W/C Ratio	Slump (in)	Material	Batch weight per cu. Ft (lbs)
0.40	2	Rock, lb	95.50
		Sand, lb	60.25
		Water, lb	10.85
		Cement, lb	24.42
0.45	2	Rock, lb	90.25
		Sand, lb	133
		Water, lb	12.02
		Cement, lb	24.42
0.50	1.5	Rock, lb	89.65
		Sand, lb	133
		Water, lb	13.12
		Cement, lb	24.42

The pullout test results for the 14°F, 77°F, and 252°F corroded rebar temperature

experiments are shown in the Tables 31-40.

Table 31. Measured bond strength magnitudes for corroded rebar steels at different w/c ratios after 3 days at 14°F rebar temperature, 8-in Embedment.

w/c	Embedment Length (in)	Actual Embedment Length (in)	Maximum Pullout Force (lbf)	Average Pullout Force (lbf)	Shear stress(psi)	Extension at Peak Load (in)	Average Extension (in)
0.40	8	8	5210	6060	321	0.158	0.167
0.40	8	8	6910			0.176	
0.45	8	8	5449	4355	231	0.180	0.157
0.45	8	8	3261			0.134	
0.50	8	8	2786	2331.	123	0.098	0.090
0.50	8	8	1875			0.081	

Table 32. Test Measured bond strength magnitudes for corroded rebar steels at different w/c ratios after 3 days at 77°F rebar temperature, 8-in Embedment.

w/c	Embedment Length (in)	Actual Embedment Length (in)	Maximum Pullout Force (lbf)	Pullout Force (lbf)	Shear stress(psi)	Extension at Peak Load (in)	Extension (in)
0.40	8	8	5484	6001	318	0.183	0.188
0.40	8	8	6518			0.192	
0.45	8	8	3828	4204	223	0.171	0.180
0.45	8	8	4579			0.189	
0.50	8	8	1521	1653	87	0.087	0.073
0.50	8	8	1786			0.059	

Table 33. Measured bond strength magnitudes for corroded rebar steels at different w/c ratios after 3 days at 252°F rebar temperature, 8-in Embedment.

w/c	Embedment Length (in)	Actual Embedment Length (in)	Maximum Pullout Force (lbf)	Average Pullout Force (lbf)	Shear stress(psi)	Extension at Peak Load (in)	Average Extension (in)
0.40	8	8	4612	4548	241	0.137	0.130
0.40	8	8	4485			0.124	
0.45	8	8	4953	4440	235	0.085	0.097
0.45	8	8	3927			0.108	
0.50	8	8	1474	1063	56	0.060	0.042
0.50	8	8	651			0.024	

Table 34. Measured bond strength magnitudes for corroded rebar steels at different w/c ratios after 10 days at 14°F rebar temperature, 8-in Embedment.

w/c	Embedment Length (in)	Actual Embedment Length (in)	Maximum Pullout Force (lbf)	Average Pullout Force (lbf)	Shear stress(psi)	Extension at Peak Load (in)	Average Extension (in)
0.40	8	8	7022	9063	480	0.236	0.243
0.40	8	8	11103			0.249	
0.45	8	8	5130	4940	262	0.208	0.196
0.45	8	8	4751			0.183	
0.50	8	8	3414	3797	201	0.100	0.118
0.50	8	8	4179			0.135	

Table 35. Measured bond strength magnitudes for corroded rebar steels at different w/c ratios after 10 days at 77°F rebar temperature, 8-in Embedment.

w/c	Embedment Length (in)	Actual Embedment Length (in)	Maximum Pullout Force (lbf)	Pullout Force (lbf)	Shear stress(psi)	Extension at Peak Load (in)	Extension (in)
0.40	8	8	9809	7973	422	0.221	0.186
0.40	8	8	6136			0.151	
0.45	8	8	4434	4887	259	0.136	0.184
0.45	8	8	5339			0.232	
0.50	8	8	2979	3676	195	0.117	0.148
0.50	8	8	4373			0.179	

Table 36. Measured bond strength magnitudes for corroded rebar steels at different w/c ratios after 10 days at 252°F rebar temperature, 8-in Embedment.

w/c	Embedment Length (in)	Actual Embedment Length (in)	Maximum Pullout Force (lbf)	Average Pullout Force (lbf)	Shear stress(psi)	Extension at Peak Load (in)	Average Extension (in)
0.40	8	8	7744	6781	359	0.227	0.171
0.40	8	8	5817			0.155	
0.45	8	8	4300	4185	222	0.143	0.160
0.45	8	8	4069			0.176	
0.50	8	8	1190	1654	87	0.048	0.073
0.50	8	8	2118			0.097	

Table 37. Measured bond strength magnitudes for corroded rebar steels at different w/c ratios after 28 days at 14°F rebar temperature, 8-in Embedment.

w/c	Embedment Length (in)	Actual Embedment Length (in)	Maximum Pullout Force (lbf)	Average Pullout Force (lbf)	Shear stress(psi)	Extension at Peak Load (in)	Average Extension (in)
0.40	8	8	10367	8991	477	0.297	0.258
0.40	8	8	7616			0.218	
0.45	8	8	5586	5461	289	0.178	0.186
0.45	8	8	5336			0.194	
0.50	8	8	3097	3824	202	0.219	0.249
0.50	8	8	4550			0.278	

Table 38. Measured bond strength magnitudes for corroded rebar steels at different w/c ratios after 28 days at 77°F rebar temperature, 8-in Embedment.

w/c	Embedment Length (in)	Actual Embedment Length (in)	Maximum Pullout Force (lbf)	Pullout Force (lbf)	Shear stress(psi)	Extension at Peak Load (in)	Extension (in)
0.40	8	8	9044	8738	463	0.280	0.240
0.40	8	8	8432			0.200	
0.45	8	8	5191	5162	273	0.172	0.180
0.45	8	8	5133			0.188	
0.50	8	8	3540	3591	190	0.163	0.126
0.50	8	8	3643			0.089	

Table 39. Measured bond strength magnitudes for corroded rebar steels at different w/c ratios after 28 days at 252°F rebar temperature, 8-in Embedment.

w/c	Embedment Length (in)	Actual Embedment Length (in)	Maximum Pullout Force (lbf)	Average Pullout Force (lbf)	Shear stress(psi)	Extension at Peak Load (in)	Average Extension (in)
0.40	8	8	6067	5704	302	0.204	0.176
0.40	8	8	5342			0.148	
0.45	8	8	3873	4052	214	0.175	0.191
0.45	8	8	4230			0.206	
0.50	8	8	3136	3177	168	0.103	0.162
0.50	8	8	3219			0.221	

Table 40 shows the overall results for the corroded rebar tests.

Table 40. Measured bond strength magnitudes for corroded rebar steels at different w/c ratios and rebar temperatures, 8-in Embedment

w/c	Temp (°F)	Pullout Force (lbf)			Shear Stress (psi)			Extension (in)		
		3day	10day	28day	3day	10day	28day	3day	10day	28day
0.40		6060	9063	8991	321	480	477	0.167	0.243	0.258
0.45	14	4355	4940	5461	231	262	289	0.157	0.196	0.186
0.50		2331	3797	3824	123	201	202	0.090	0.118	0.249
0.40		6001	7973	8738	318	422	463	0.188	0.186	0.240
0.45	77	4204	4887	5162	223	259	273	0.180	0.184	0.180
0.50		1653	3676	3591	87	195	190	0.073	0.148	0.126
0.40		4548	6781	5704	241	359	302	0.130	0.171	0.176
0.45	252	4440	4185	4052	235	222	214	0.097	0.160	0.191
0.50		1063	1654	3177	56	87	168	0.042	0.073	0.162

Figures 49 and 50 show the 10-day and 28-day corroded rebar pullout test results respectively.

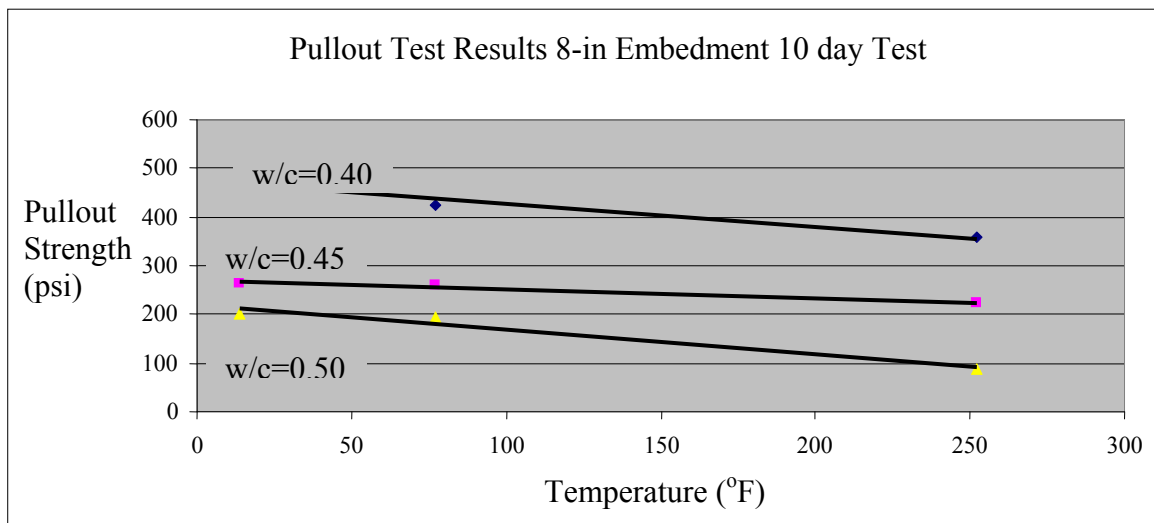Figure 51 shows the overall corroded rebar pullout test results.

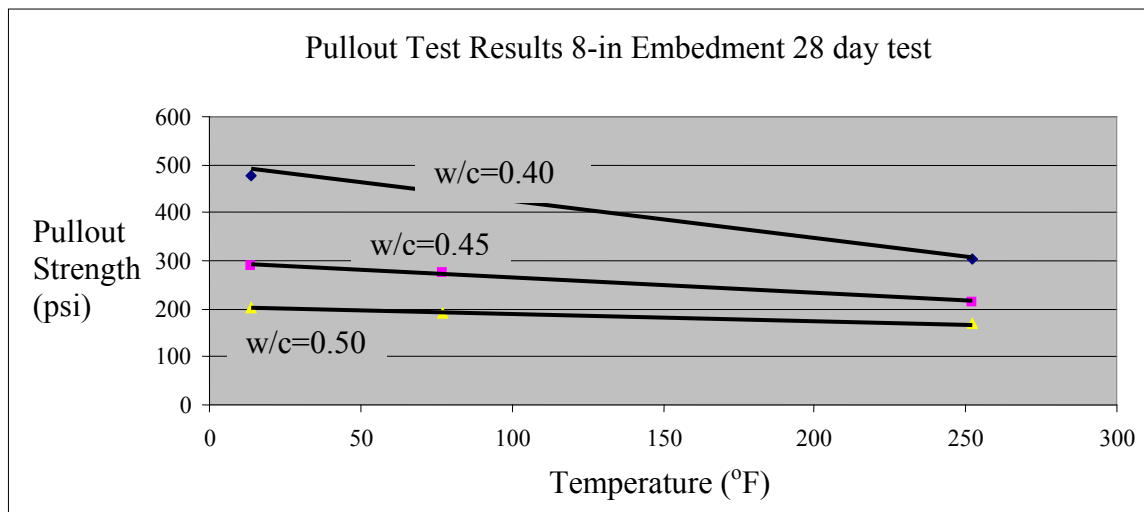Figure 49. Bond strength vs. rebar temperature pullout test results for corroded rebar at 10 days.

Figure 50. Bond strength vs. rebar temperature pullout test results for corroded rebar at 28 days.
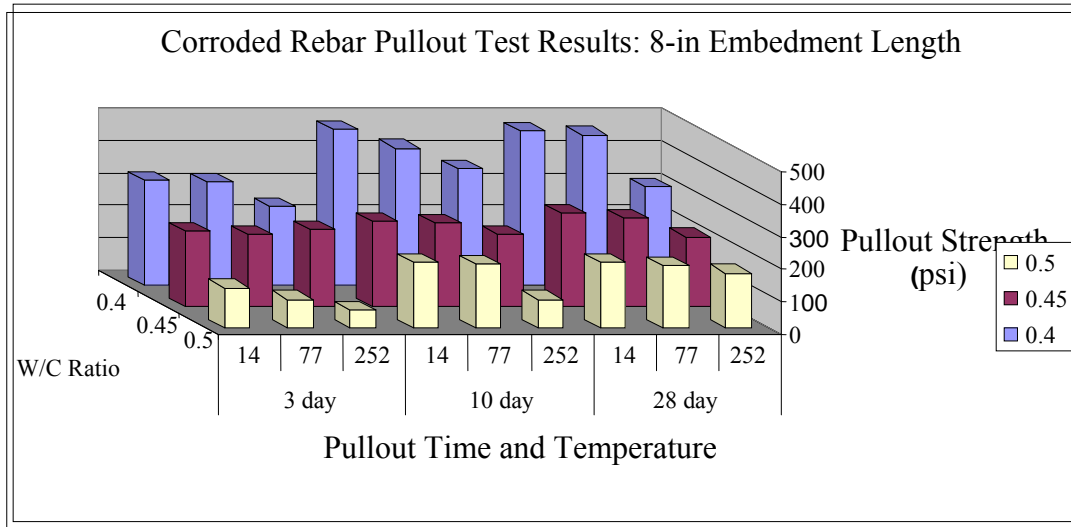
Figure 51. Corroded rebar pullout test results 8-in embedment length at different pullout times, temperature and w/c ratios.

FTIR Results

After performing the pullout tests, an examination of the rebar-concrete interface and the rebar was done. Apart from the corrosion products characterized by an earthy red coloration from the rebar prior to the experiments being done, there was a presence of a blackish and a reddish brown product both on the rebar-concrete interface and the rebar itself. FTIR spectroscopy was performed and it was determined that the corrosion product present on the rebar were maghemite (γ–Fe_2O_3), goethite (α-FeOOH and gepidocrocite (γ–FeOOH) with a wave number 1094.04 cm^{-1}. The FTIR spectrum is shown in Figure 52.
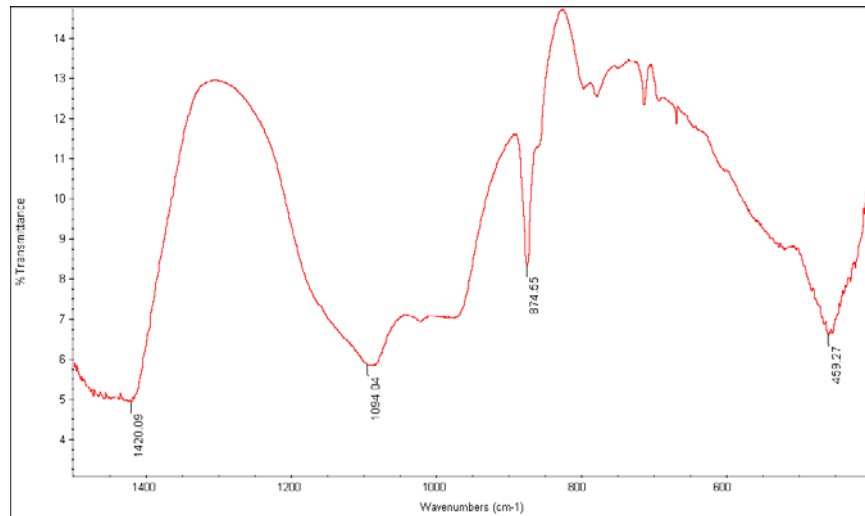
Figure 52. FTIR spectrum of corroded rebar after curing.

This corrosion product build-up will ultimately lead to an increase in internal stresses in the rebar-concrete interface exacerbating early age cracking because the oxide and hydroxides have specific volumes greater than that of steel as earlier discussed. Lepidocrocite (γ –FeOOH) and maghemite (γ –Fe$_2$O$_3$) have a specific volume of 2.2 and 3.15 respectively.

Rebar Temperature Effects

The pullout test results on the corroded rebars also showed reduction in the peak pullout load as the temperature increased just as observed in the non-corroded rebar for the 10-day and 28-day tests (Figure 49 and 50). The measured bond strength magnitudes for the 28 days tests at 14°F rebar temperature were 477 psi, 289 psi and 202 psi for the w/c ratios of 0.40, 0.45 and 0.45 respectively (Table 40). These values were relatively higher compared to the 252°F rebar temperature values of 302 psi, 214 psi and 168 psi for the 28 days tests. The pullout load and shear strength measurements were however lower for the corroded rebar compared to the non-corroded rebar. The decrease in bond strength can be attributed to the presence of corrosion products on the concrete rebar interface. These results agree with those done by Batis and

79

Rakanta (2005) in which they found that pre-oxidized steels exhibited a great reduction in pullout strength with the bond strength between rebar steel and concrete decreasing with increasing weathering on steels.

Water to Cement Ratio Effects

The w/c ratio effects exhibited the same characteristics as observed in the previous experiment with non-corroded rebars. The 28 day shear stress measurements showed that the lower the water to cement ratio the higher the rebar concrete bond strength (Figure 51). The w/c ratio values for the 77°F rebar temperature were 422 psi, 259 psi, and 195 psi for w/c ratios of 0.40, 0.45, and 0.50 respectively (Table 40).The w/c ratio effects in relation to the bond strength characteristics was also examined by Romagnoli et al. (2002). In their experiment, they observed that the steel-mortar bond strength decreased as the water to cement ratio increased. They performed their experiment after 1 year of exposing their specimens to different electrolytes. They found out that the rebar-mortar bond strength for the specimens stored in tap water were higher than those stored in 3 percent NaCl solution. The corrosive environment created by the NaCl lead to low bond strength analogous to the corroded rebars used in this experiment.

Rebar Condition Effects

The results of the pullout tests on the corroded rebar showed that the 28-day bond strength decreased by a value between 20-50 % compared to the results obtained for the non-corroded rebars. For example, the 28 days pullout test results for the w/c ratio of 0.40 at 14°F rebar temperature for the non-corroded rebar was 647 psi compared to 477 psi for the corroded rebar for the same parameters (Tables 27 and 40). Bond strength reduction is a result the

corrosion product, rust, residing at the interface between reinforcement and concrete. This degraded the bond between rebar and concrete. These results are in agreement with those done by Congqi et al. (2004) in their study of the influence of corrosion on bond in reinforced concrete. Figure 53 shows the ESEM micrographs of the ITZ for the corroded rebar steels.

The fundamental difference between the corroded and non-corroded experiments rebar tests is the conglomeration of corrosion products on the rebar concrete interface (Figure 53 (a) – (i)). The images show a distinct and clear plastering of the corrosion product on the interfacial zone shown as bright layers on the ESEM pictures compared to the darker and denser concrete matrix. The ESEM micrographs shown are for the 28-day curing time, the 3-day and 10-day images are shown in Appendix C.

Energy dispersive x-ray spectroscopy (EDS) was used to chemically characterize the elements on the ITZ. EDS was used because each periodic table element has a unique electronic configuration that gives a specific response to high-energy radiation. For this research, a Quanta 200 equipped with EDAX was used to perform the chemical analyses on the concrete samples' rebar-concrete interface and the ITZ.

The corrosion products were established to be Maghemite (γ –Fe_2O_3), Goethite (α-FeOOH) and Lepidocrocite (γ –FeOOH) by FTIR measurements (Figure 52). The presence of corrosion products led to the reduction in the pullout peak loads as shown by the pullout tests results (Table 40). These corrosion products prevented the proper development of bond between the rebar and concrete matrix. The ESEM image for the 28-day of the test specimens for the w/c ratios of 0.50 at $252^{o}F$ shows a porous structure (Figure 53 (i)) similar to what was observed on the non-corroded specimen (Figure 37 (e)). Figure 53 shows the ESEM micrographs of the ITZ for corroded rebar steels.
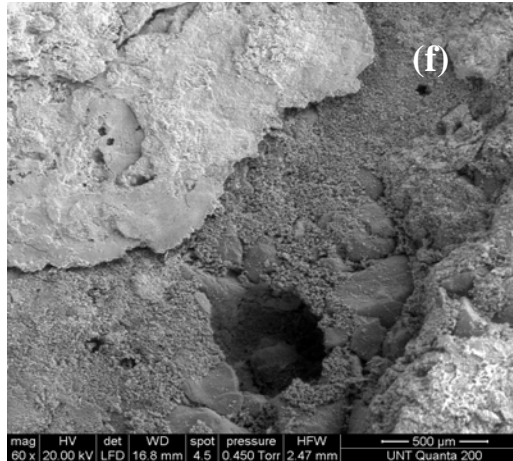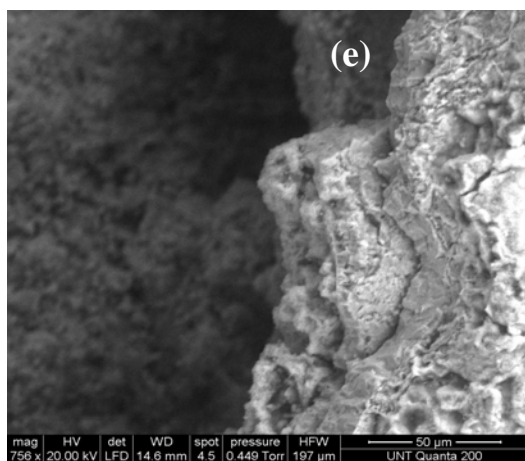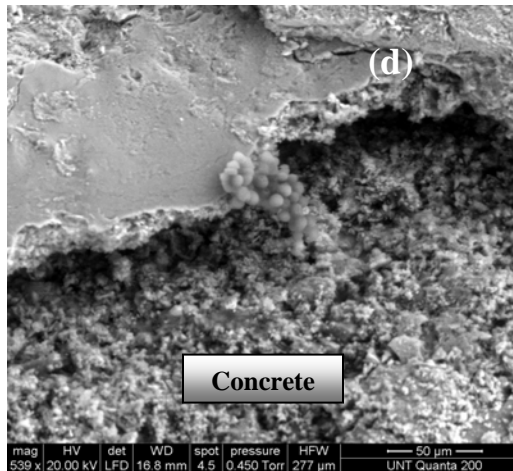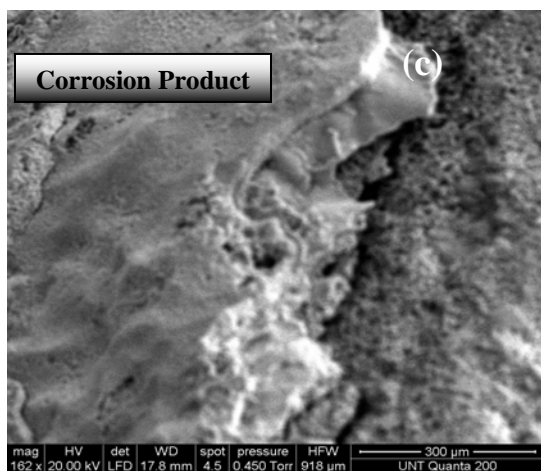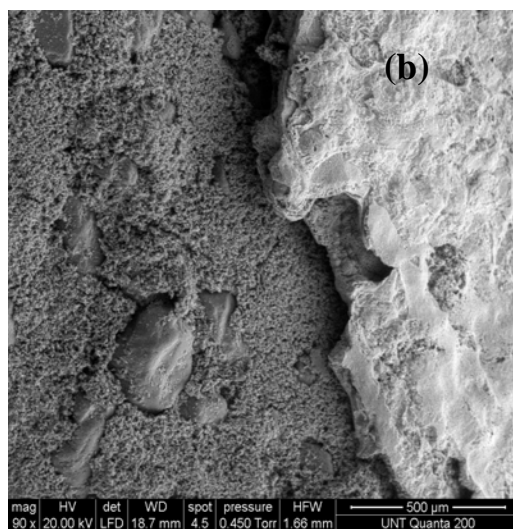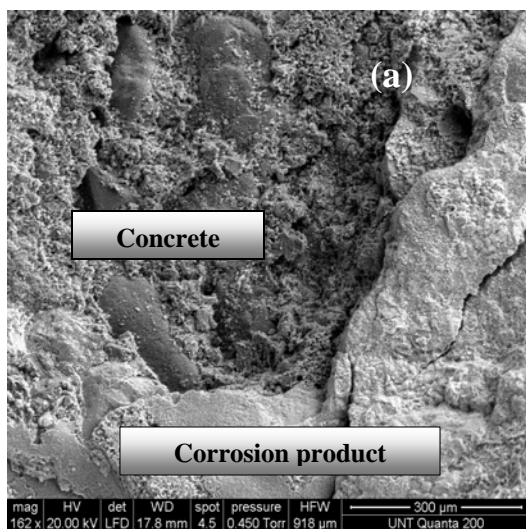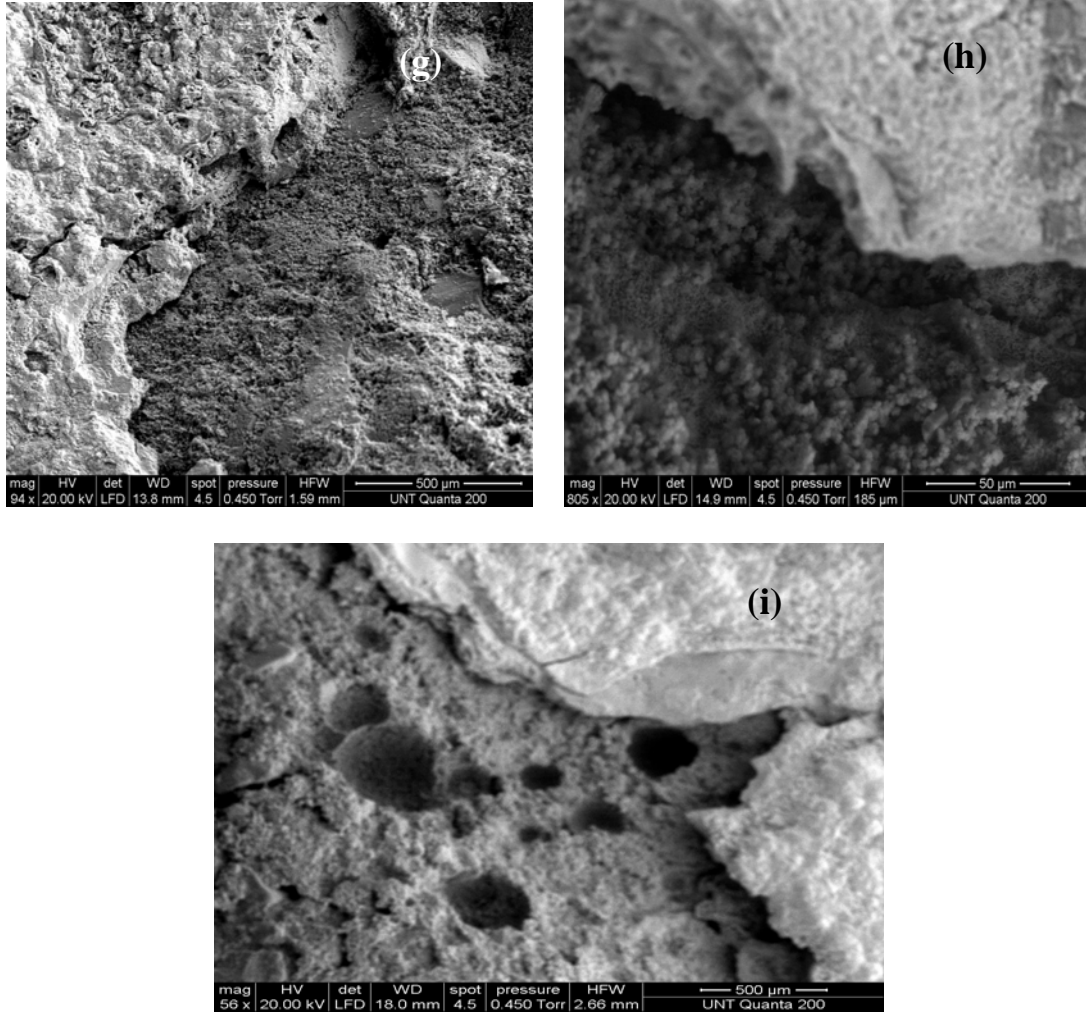
Figure 53. ESEM micrographs of the ITZ for corroded rebar steels at 14°F for w/c 0.40 after 28 days (a), 14°F for w/c 0.45 after 28 days (b), 14°F for w/c 0.50 after 28 days (c), 77°F for w/c 0.40 after 28 days (d), 77°F for w/c 0.45 after 28 days (e), 77°F for w/c 0.50 after 28 days (f), 252°F for w/c 0.40 after 28 days (g), 252°F for w/c 0.45 after 28 days (h), 252°F for w/c 0.50 after 28 days (i).

Figure 54 shows the elemental analysis of the ESEM micrograph of the ITZ for the

corroded rebar at 14°F for w/c 0.40 after 28 days.
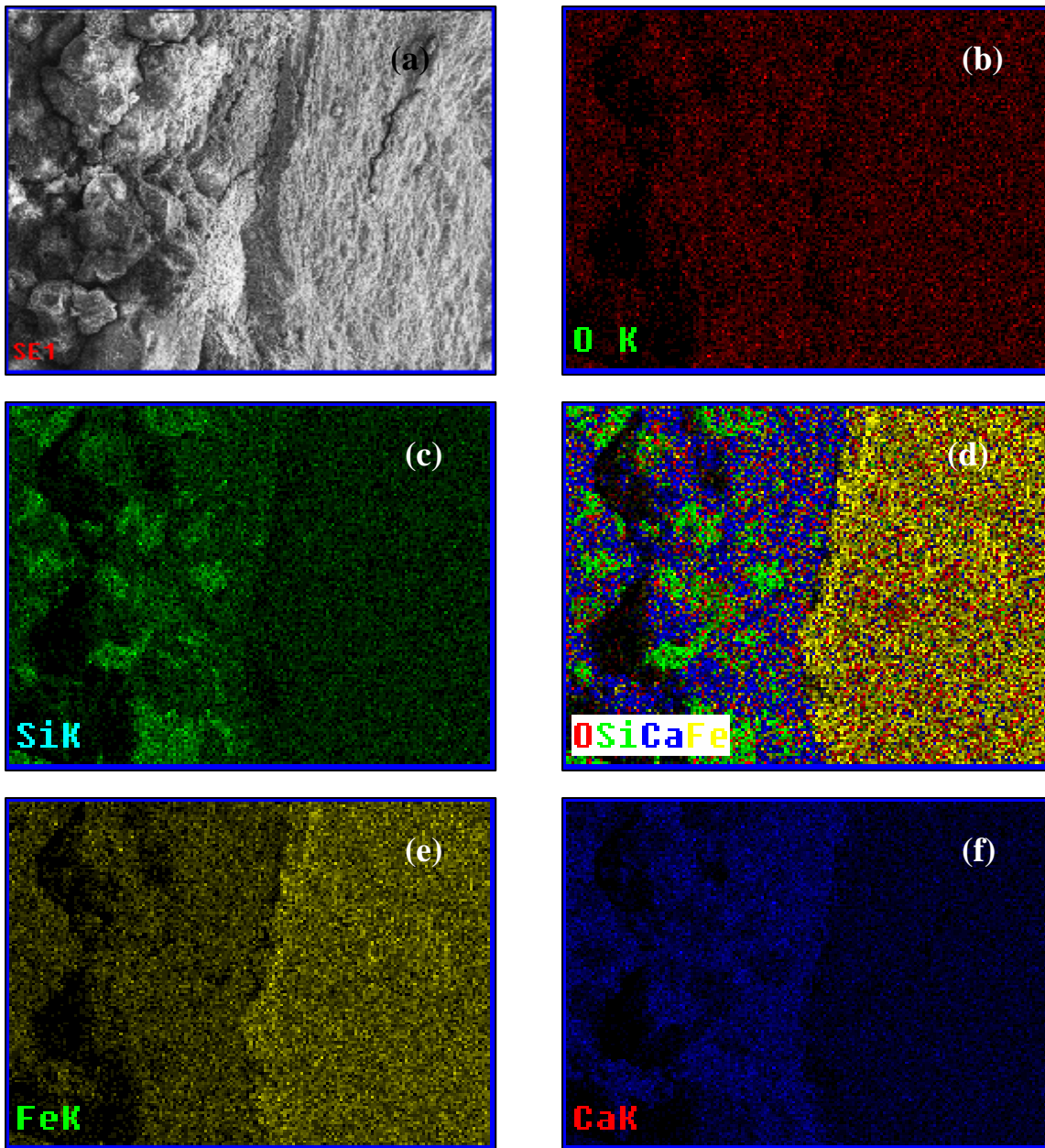
Figure 54. ESEM micrograph of the ITZ for corroded rebar steel at 14°F for w/c 0.40 after 28 days (a), oxygen mapscan (b) iron mapscan (c), calcium mapscan (d), silicon mapscan (e), EDS overlay of elements mapscan (f).

Figure 55 shows the spectrum of the elements present on the rebar-concrete and the ITZ interface.
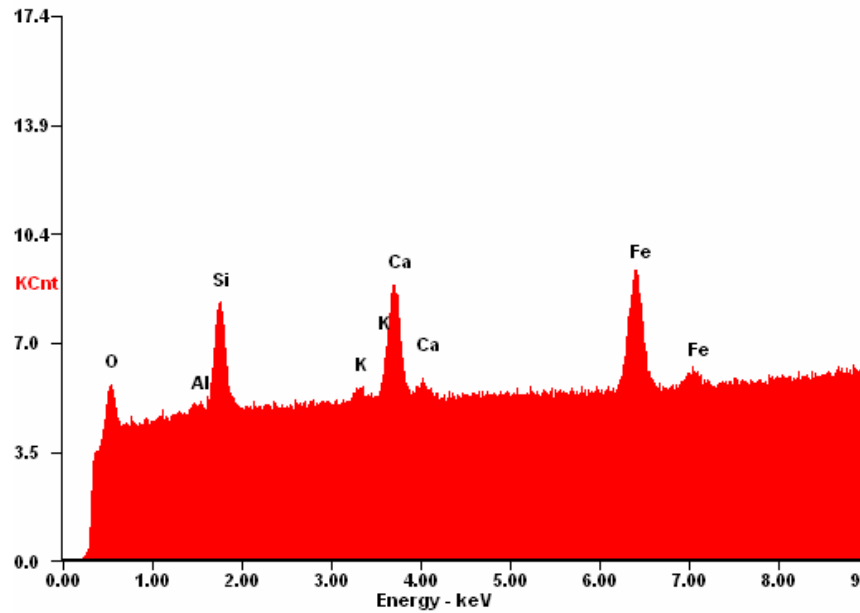
Figure 55. EDS elements spectrum for the ESEM micrograph of the ITZ for corroded rebar steel at 14°F for w/c 0.40 after 28 days.

CHAPTER VI

CONCLUSIONS

The primary objective of this study was to identify the effect of rebar temperature at the concrete pouring stage on the concrete- rebar bond strength, the effect of changing the water to cement ratio, using non-corroded rebar steel versus corroded rebar steel and how the morphology of the interfacial transition zone changes with the variation of these parameters. An in-depth analysis of the microstructure of the interfacial transition zone (ITZ) was studied and various experiments were undertaken to analyze the interfacial chemistry and morphological characteristics of the concrete mix. The identification of the significant factors and processes responsible for the early age cracking of continuously reinforced concrete pavements (CRCP) were also studied.

Corrosion product characterization was achieved by the use of FTIR and EDS. ESEM was used to determine the morphology of the ITZ at the concrete rebar interface. The operating parameters of the ESEM were accelerating voltage 20 keV and a chamber pressure of 0.450 Torr. The magnification values used were 30 – 50 for low magnification examination and 900 – 1600 for high magnification examination. Detailed analysis of the variation of the different parameters mentioned above enabled us to study the early-age behavior of concrete as applied in the construction of CRCP. The 4-in embedment length parameter was not considered because of the inconsistencies in the final embedment lengths of the samples after curing. For this reason, only the 8-inch embedment length samples were used for analysis.

The experimental results can be categorized into rebar temperature, water to cement ratio, and initial rebar condition effects. These parameters allowed for the examination of the ITZ and the rebar-concrete interface. The experimental investigation showed:

i) The bond strength was significantly influenced by the water to cement ratio. The 28 day shear stress measurements showed that the lower the water to cement ratio the higher the rebar concrete bond strength.

ii) Based on the 10 days and 28 days data (Figures 41, 42, 49 and 50), that there is a reduction in the peak pullout load as the temperature increased from 14^oF to 252^oF for both the corroded and non-corroded rebar experiments.

iii) The images show that aggregate particles add a new level of heterogeneity and disrupt the packing of cement particles locally at the cement paste aggregate interface.

iv) There is bridging of cracks between coarse aggregate locations within the interfacial zone and these propagate through the mortar.

v) The structure of the ITZ grows more compactly as the curing time increases. They consistently show that the ITZ of the corresponding w/c ratio and temperature becomes denser as the curing time increases.

vi) Presence of corrosion products on the ITZ ultimately led to a reduction on rebar concrete bond strength. From the results obtained from this research, corrosion cannot be said to be responsible for early age cracking as microcracks were also observed on the non-corroded rebar specimens at as early as three days.

CHAPTER VII

RECOMMENDATIONS AND FUTURE WORK

There is need for the examination of the ITZ using the parameters used in this experiment without doing pullout tests. Pullout tests interfere with the microstructure of the interface and the results are not a true representation of the interface. There should also be experimentation using different aggregates to determine the bridging characteristics of cracks in the interfacial zone. A rebar temperature of between $150^{o}F - 170^{o}F$ should also be used to determine their effect on the characteristics of the rebar-concrete interface. Since the pullout test does not fully represent the stress conditions existing in the concrete around reinforcement in a flexural member, a flexural test for example using beam end specimens should be used as in this case the steel and the concrete are in tension.

APPENDIX A

NON-CORRODED REBAR PULLOUT TEST GRAPHS

Specimen 1 to 1
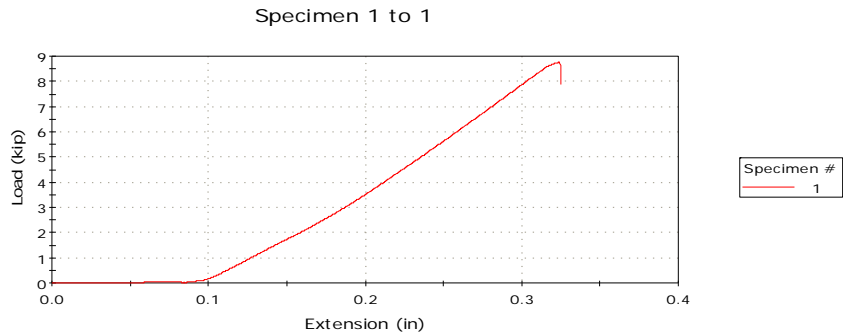
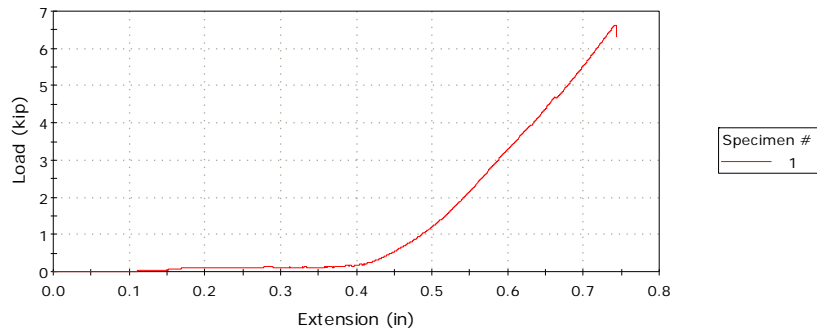| Actual Embedment Length (in)	Extension at Machine Peak Load (in)	Load at Machine Peak Load (lbf)
5	0.32400	8770

W/C 0.40 4-in Embedment Length
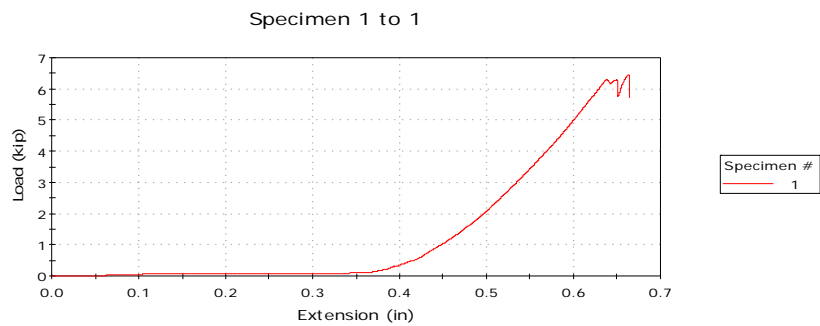
Specimen 1 to 1

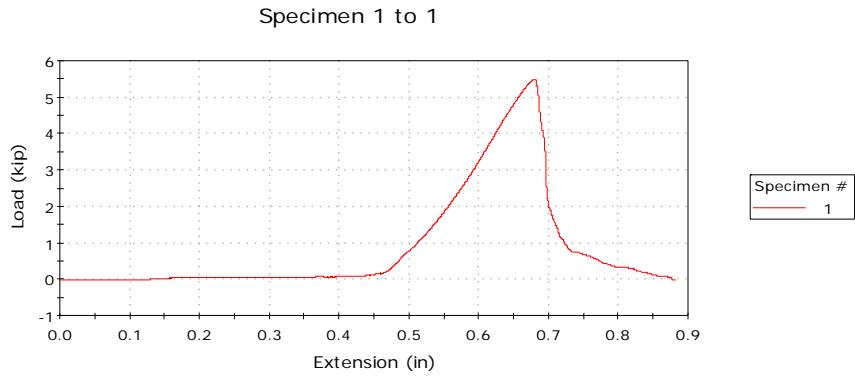| Actual Embedment Length (in)	Extension at Machine Peak Load (in)	Load at Machine Peak Load (lbf)
4.2	0.66300	6456

W/C 0.40 4-in Embedment Length

Specimen 1 to 1

Actual Embedment Length (in)	Extension at Machine Peak Load (in)	Load at Machine Peak Load (lbf)
4.5	0.74200	6620

W/C 0.45 4-in Embedment Length

Specimen 1 to 1
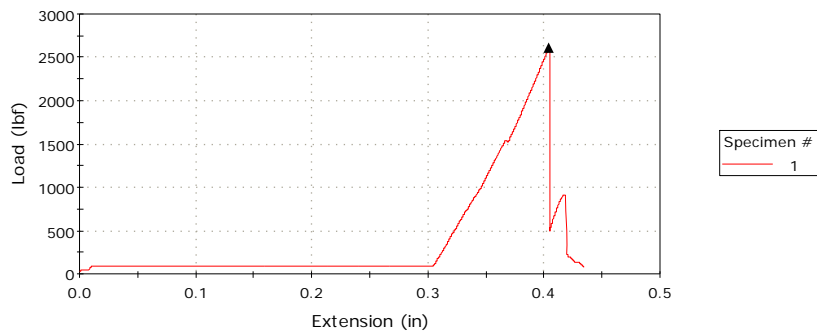
Actual Embedment Length (in)	Maximum Load (lbf)	Extension at Maximum Load (in)
3.2	2608	0.40403

W/C 0.45 4-in Embedment Length

Specimen 1 to 1

Actual Embedment Length (in)	Extension at Machine Peak Load (in)	Load at Machine Peak Load (lbf)
4	0.68100	5490

W/C 0.50 4-in Embedment Length
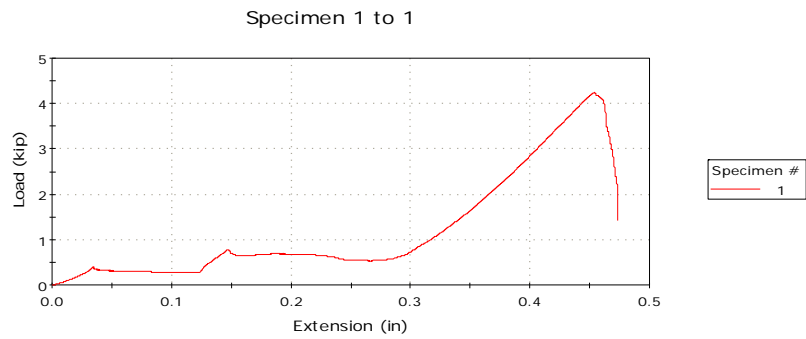
Specimen 1 to 1

Actual embedment length (in)	Extension at Machine Peak Load (in)	Load at Machine Peak Load (lbf)
4.7	0.45400	4242

W/C 0.50 4-in Embedment Length

Specimen 1 to 1
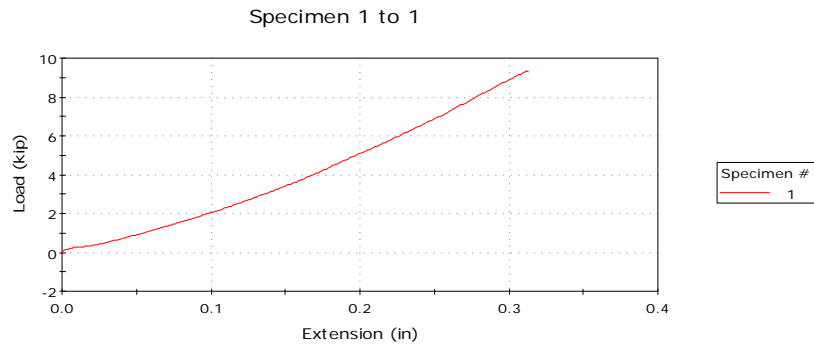
Extension at Machine Peak Load (in)	Load at Machine Peak Load (lbf)
0.31300	9323

W/C 0.40 8-in Embedment Length

Specimen 1 to 1
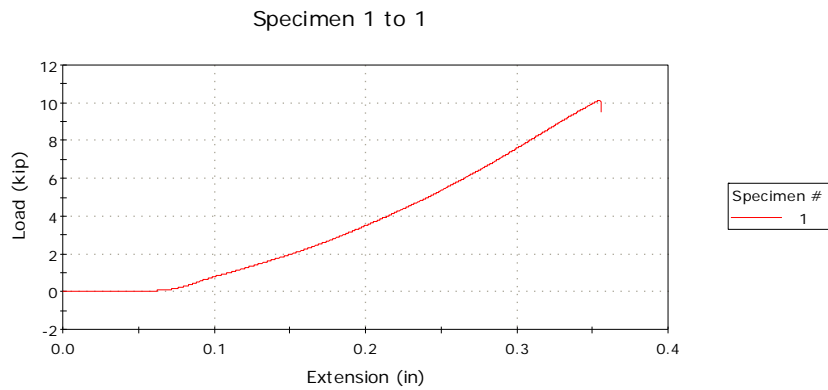
Extension at Machine Peak Load (in)	Load at Machine Peak Load (lbf)
0.35500	10130

W/C 0.40 8-in Embedment Length
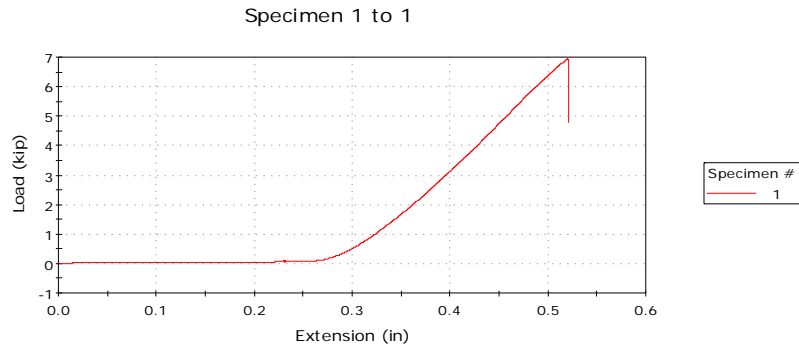
Specimen 1 to 1

Extension at Machine Peak Load (in)	Load at Machine Peak Load (lbf)
0.52000	6953

W/C 0.45 8-in Embedment Length
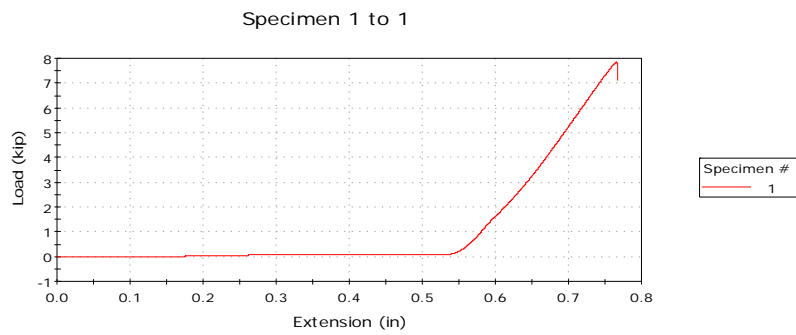
Specimen 1 to 1

Extension at Machine Peak Load (in)	Load at Machine Peak Load (lbf)
0.76600	7852
0.76600	7852

W/C 0.45 8-in Embedment Length
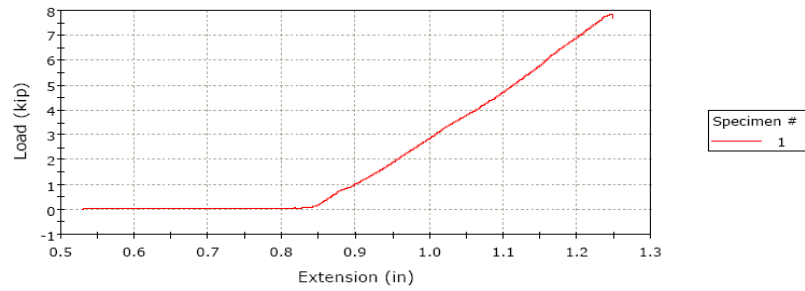
Specimen 1 to 1

	Extension at Machine Peak Load (in)	Load at Machine Peak Load (lbf)
1	> 1.24800	7866.00000
Maximum	1.24800	7866.00000
Minimum	1.24800	7866.00000
Standard Deviation	-----	-----

W/C 0.50 8-in Embedment Length

Specimen 1 to 1
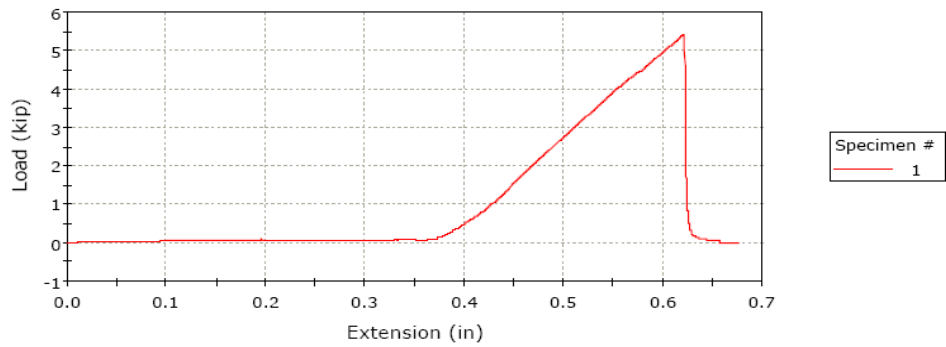
	Extension at Machine Peak Load (in)	Load at Machine Peak Load (lbf)
1	> 0.62200	5412.00000
Maximum	0.62200	5412.00000
Minimum	0.62200	5412.00000
Standard Deviation	-----	-----

W/C 0.50 8-in Embedment Length
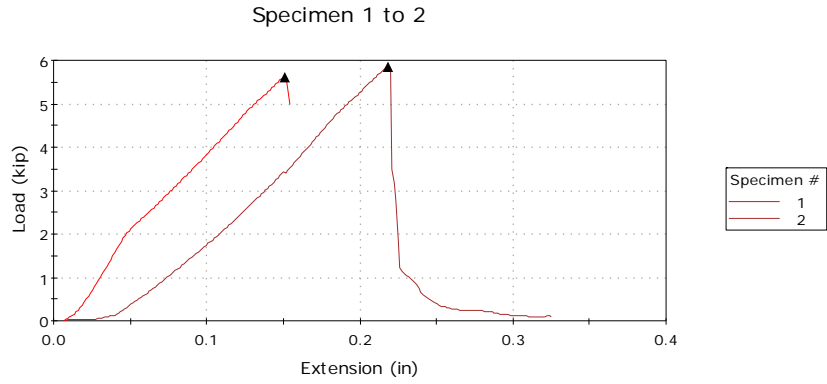
10 DAY TESTS, 8-IN EMBEDMENT LENGTH, 77°F

Specimen 1 to 2
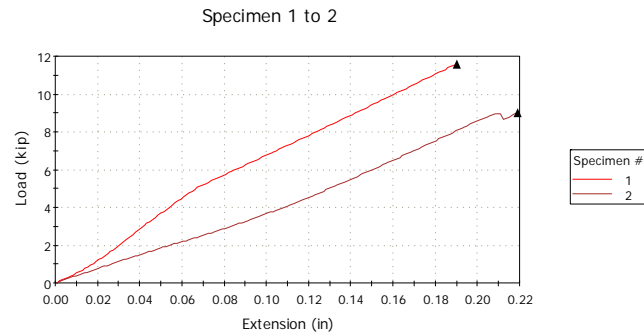
Specimen #	Maximum Load (lbf)	Extension at Maximum Load (in)
1	11586	0.19009
2	9004	0.21910

W/C 0.40, Embedment Length 8-in

Specimen 1 to 2
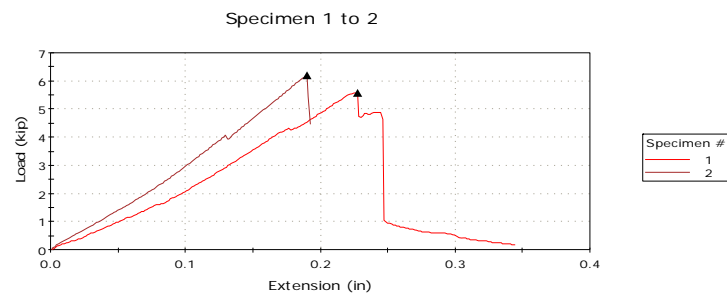
Specimen #	Maximum Load (lbf)	Extension at Maximum Load (in)
1	5583	0.22756
2	6182	0.18983

W/C 0.45, Embedment length 8-in

Specimen 1 to 2

Specimen #	Maximum Load (lbf)	Extension at Maximum Load (in)
1	5613	0.15064
2	5846	0.21839

W/C 0.50, Embedment Length 8-in

10DAY TESTS, 4-IN EMBEDMENT LENGTH, 77°F

Specimen 1 to 2
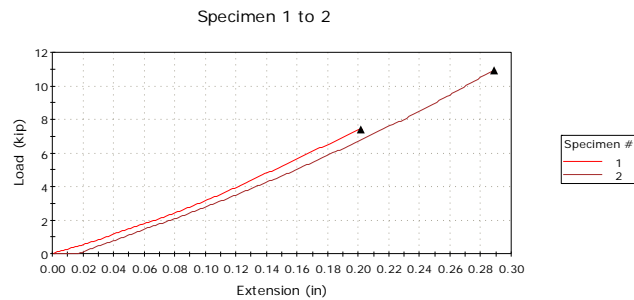
Specimen #	Actual Embedment Length (in)	Maximum Load (lbf)	Extension at Maximum Load (in)
1	4.3	7398	0.20185
2	5	10926	0.28907

W/C 0.40, Embedment Length 4-in

Specimen 1 to 2
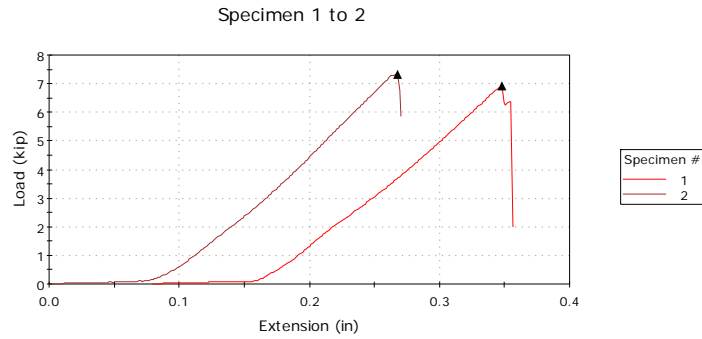
Specimen #	Actual Embedment Length (in)	Maximum Load (lbf)	Extension at Maximum Load (in)
1	5	6915	0.34823
2	4	7339	0.26780

W/C 0.45, Embedment length 4-in

Specimen 1 to 2
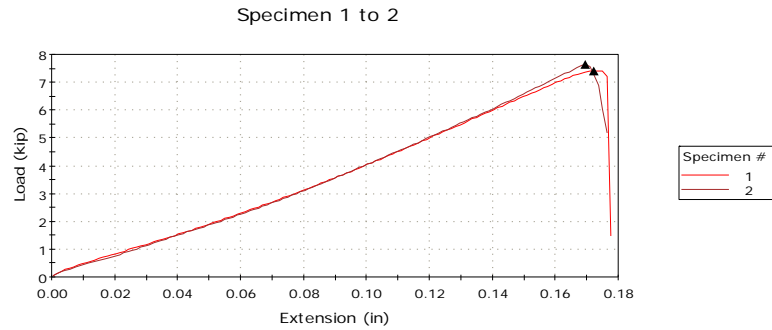
Specimen #	Actual Embedment Length (in)	Maximum Load (lbf)	Extension at Maximum Load (in)
1	4.5	7420	0.17239
2	5.5	7634	0.16967

W/C 0.50, Embedment Length 4-in

28 DAY TESTS, 8-IN EMBEDMENT LENGTH, 77°F
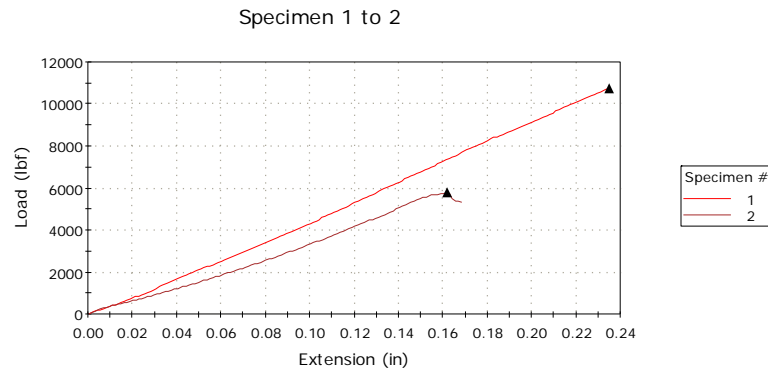
Specimen 1 to 2

Specimen #	Maximum Load (lbf)	Extension at Maximum Load (in)
1	10748	0.23501
2	5785	0.16177

W/C 0.40, Embedment length 8-in
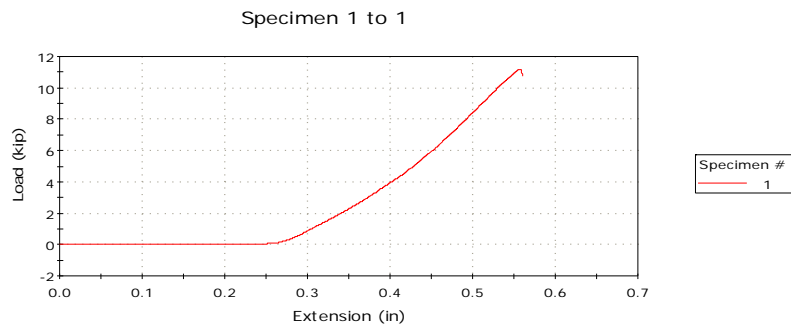
Specimen 1 to 1

Specimen #	Maximum Load (lbf)	Extension at Maximum Load (in)
1	11190	0.55800

W/C 0.40, Embedment length 8-in
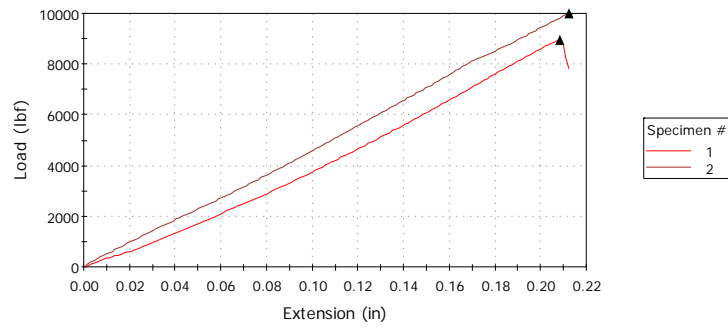
Specimen 1 to 2

Specimen #	Maximum Load (lbf)	Extension at Maximum Load (in)
1	8944	0.20847
2	9981	0.21238

W/C 0.45, Embedment Length 8-in

Specimen 1 to 2
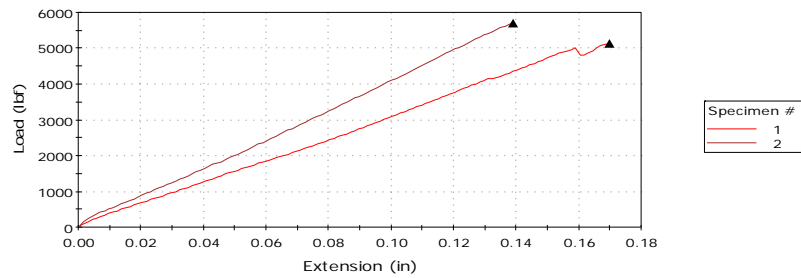
Specimen #	Maximum Load (lbf)	Extension at Maximum Load (in)
1	5132	0.16977
2	5715	0.13909

W/C 0.50, Embedment Length 8-in

28 DAY TESTS, 4-IN EMBEDMENT LENGTH, 77°F

Specimen 1 to 2
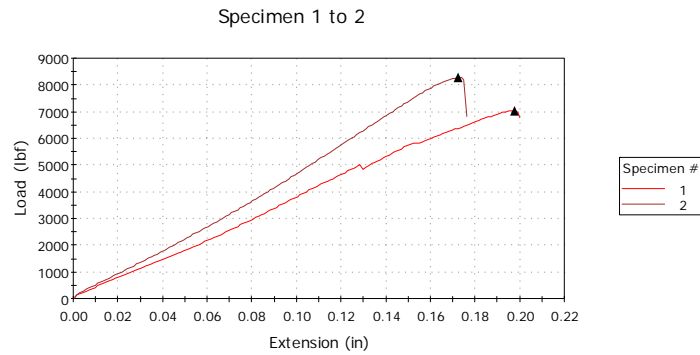
Specimen #	Actual Embedment Length (in)	Maximum Load (lbf)	Extension at Maximum Load (in)
1	4	7038	0.19773
2	4.2	8268	0.17239

W/C 0.40, Embedment length 4-in

Specimen 1 to 2
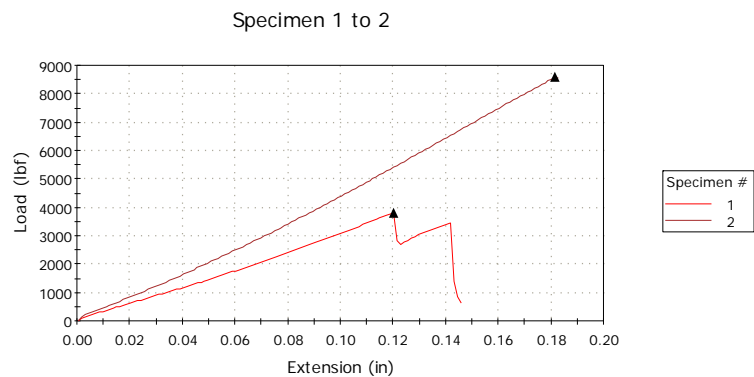
Specimen #	Actual Embedment Length (in)	Maximum Load (lbf)	Extension at Maximum Load (in)
1	3.5	3786	0.12042
2	4.5	8577	0.18171

W/C 0.45, Embedment Length 4-in

Specimen 1 to 2
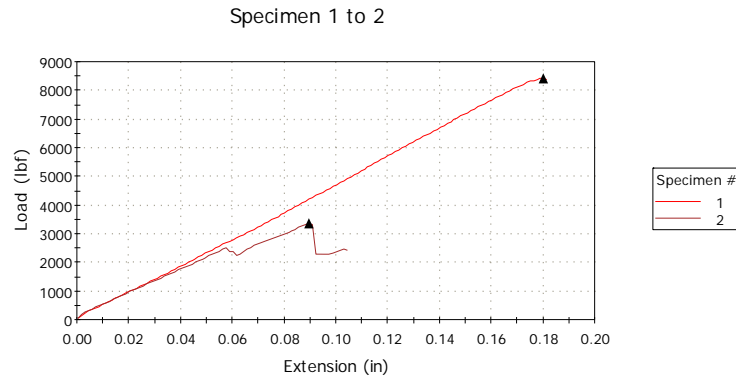
Specimen #	Actual Embedment Length (in)	Maximum Load (lbf)	Extension at Maximum Load (in)
1	4.3	8413	0.18037
2	3.8	3340	0.08977

W/C 0.50, Embedment length 4-in

3-DAY TESTS, 4-IN and 8-IN EMBEDMENT LENGTH, 14°F

Specimen 1 to 4
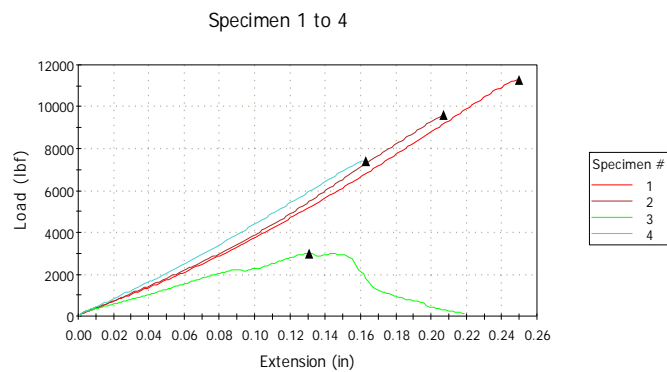
Specimen #	Embedment length (in)	Maximum Load (lbf)	Extension at Maximum Load (in)
1	8	11312	0.24973
2	8	9605	0.20706
3	3	2990	0.13106
4	4.8	7406	0.16306

W/C 0.40 3-Day Tests

Specimen 1 to 4

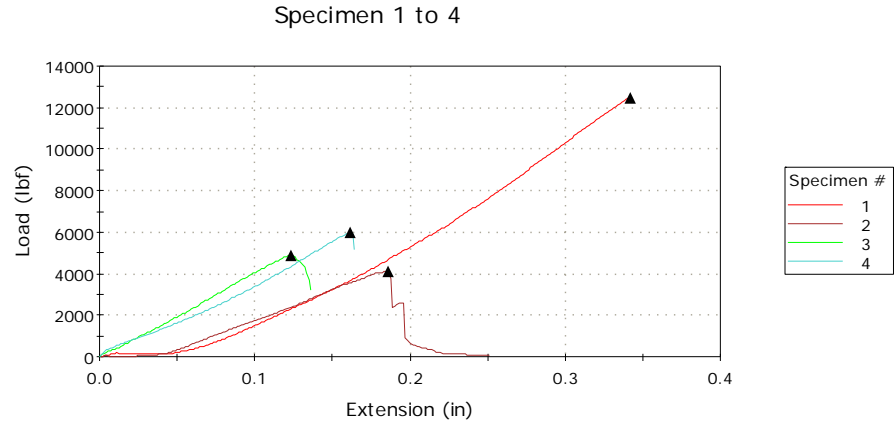| Specimen #	Embedment Length (in)	Maximum Load (lbf)	Extension at Maximum Load (in)
1	8	12488	0.34192
2	8	4118	0.18622
3	4	4877	0.12305
4	5.5	5970	0.16168

W/C 0.45 3-Day tests

Specimen 1 to 4
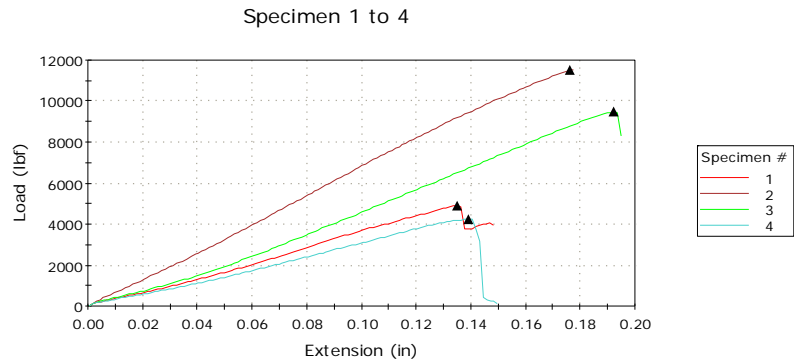
Specimen #	Embedment Length(in)	Maximum Load (lbf)	Extension at Maximum Load (in)
1	8	4899	0.13509
2	8	11538	0.17639
3	6	9468	0.19244
4	4	4230	0.13916

W/C: 0.50, 3-Day tests

10-DAY TESTS, 4-IN and 8-IN EMBEDMENT LENGTH, 14°F

Specimen 1 to 4
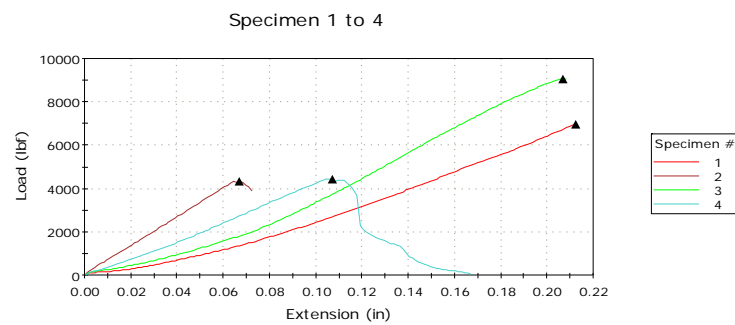
Specimen #	Embedment Length (in)	Maximum Load (lbf)	Extension at Maximum Load (in)
1	8	6955	0.21243
2	8	4332	0.06708
3	6.5	9065	0.20709
4	4.5	4424	0.10710

W/C: 0.40 10-Days Test

Specimen 1 to 5
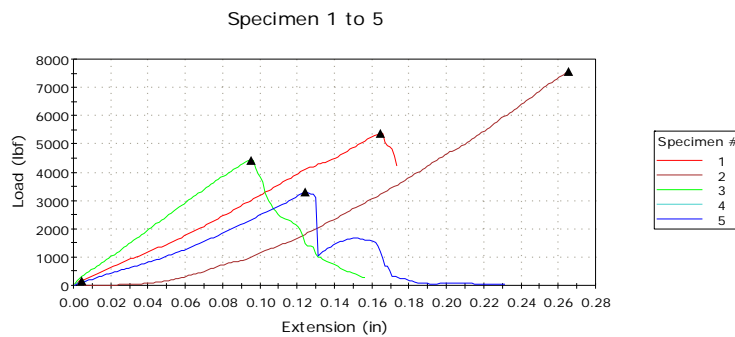
Specimen #	Embedment Length(in)	Maximum Load (lbf)	Extension at Maximum Load (in)
1	8	5369	0.16438
2	8	7546	0.26576
3	4	4437	0.09510
5	3.9	3290	0.12450

W/C: 0.45, 10-Days Test

Specimen 1 to 4
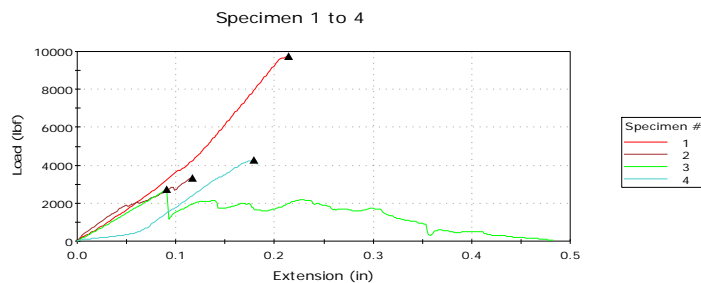
Specimen #	Embedment Length (in)	Maximum Load (lbf)	Extension at Maximum Load (in)
1	8	9750	0.21372
2	8	3332	0.11646
3	3.2	2743	0.09119
4	4	4271	0.17904

W/C: 0.50 10-Days Tests

28-DAY TESTS, 4-IN and 8-IN EMBEDMENT LENGTH, 14°F

Specimen 1 to 5
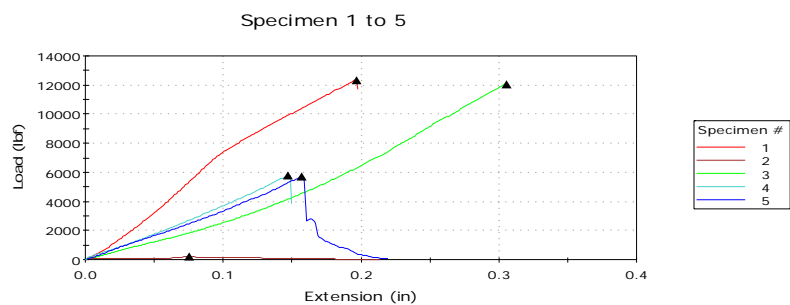
Specimen #	Embedment Length (in)	Maximum Load (lbf)	Extension at Maximum Load (in)
1	8	12332	0.19680
3	8	12075	0.30579
4	4	5798	0.14705
5	4	5704	0.15648

W/C: 0.40, 28-Days Test

Specimen 1 to 4
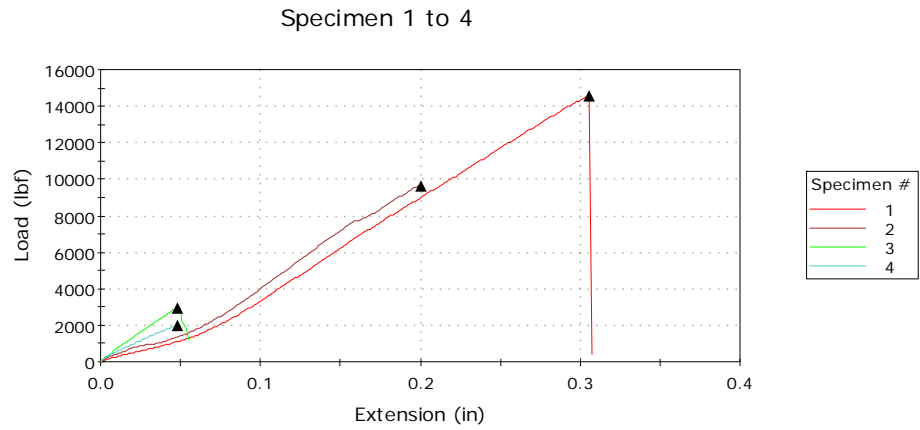
Specimen #	Embedment length (in)	Maximum Load (lbf)	Extension at Maximum Load (in)
1	8	14550	0.30577
2	8	9653	0.20037
3	2.7	1604	0.03505
4	3.2	3455	0.07773

W/C: 0.45, 28-Days Test

Specimen 1 to 4

Specimen #	Embedment Length (in)	Maximum Load (lbf)	Extension at Maximum Load (in)

Specimen #	Embedment Length (in)	Maximum Load (lbf)	Extension at Maximum Load (in)
1	8	5629	0.14572
2	8	2002	0.08441
3	4	2929	0.04842
4	3.5	1960	0.04845

W/C: 0.50, 28-Days Test

3-DAY TESTS, 4-IN and 8-IN EMBEDMENT LENGTH, 252°F

Specimen 1 to 4
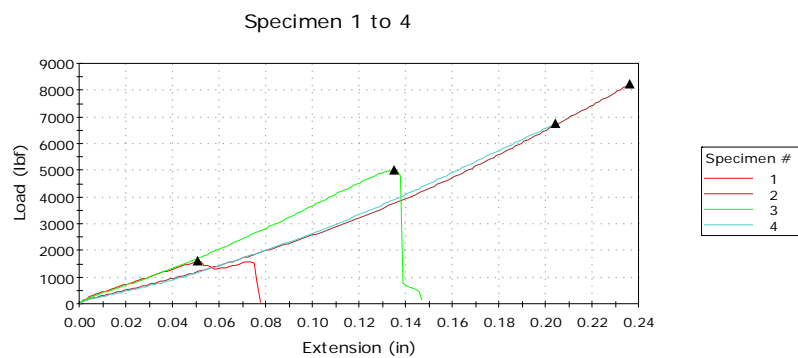
Specimen #	Embedment Length (in)	Maximum Load (lbf)	Extension at Maximum Load (in)
1	8	1618	0.05106
2	8	8230	0.23639
3	4	4209	0.11776
4	3.2	1286	0.04184

W/C: 0.40 , 3-Days Test

Specimen 1 to 4

107
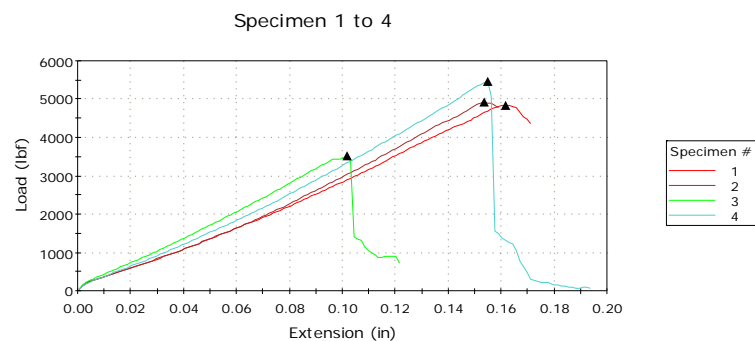
Specimen #	Embedment Length (in)	Maximum Load (lbf)	Extension at Maximum Load (in)
1	8	4840	0.16177
2	8	4918	0.15374
3	4	3868	0.10445

W/C: 0.45, 3-Days Test

Specimen 1 to 5
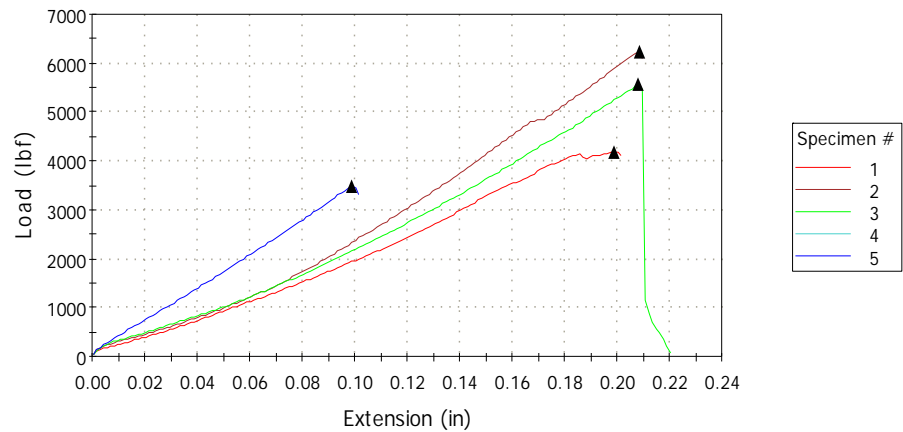
Specimen #	Embedment Length (in)	Maximum Load (lbf)	Extension at Maximum Load (in)
1	8	4179	0.19906
2	8	6246	0.20839
3	4	3508	0.10172
4	4	5460	0.15504

W/C: 0.50, 3-Days Test

10-DAY TESTS, 4-IN and 8-IN EMBEDMENT LENGTH, 252°F

Specimen 1 to 4
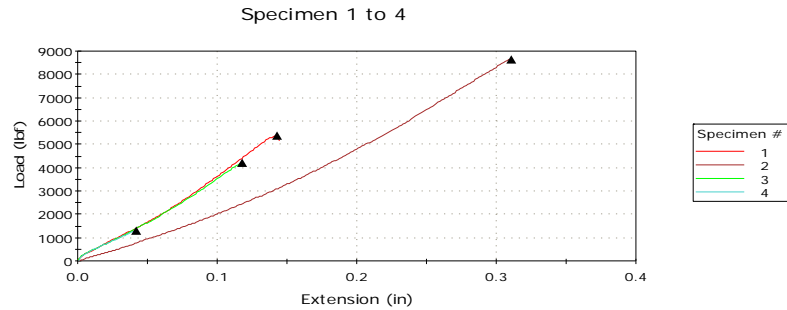
Specimen #	Embedment length (in)	Maximum Load (lbf)	Extension at Maximum Load (in)
1	8	5379	0.14307
2	8	8663	0.31041
3	4	5012	0.13508
4	4	6743	0.20439

W/C: 0.40, 10-Days Test

Specimen 1 to 3
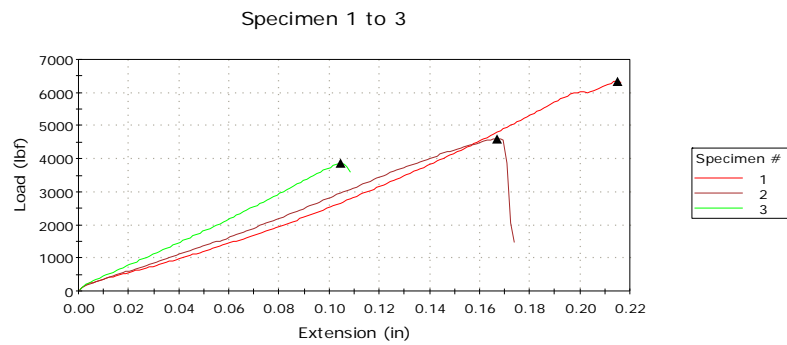
Specimen #	Embedment Length (in)	Maximum Load (lbf)	Extension at Maximum Load (in)
1	8	6343	0.21504
2	8	4606	0.16703
3	4	5559	0.20837
4	3.8	3485	0.09910

W/C: 0.45, 10-Days Test

Specimen 1 to 4
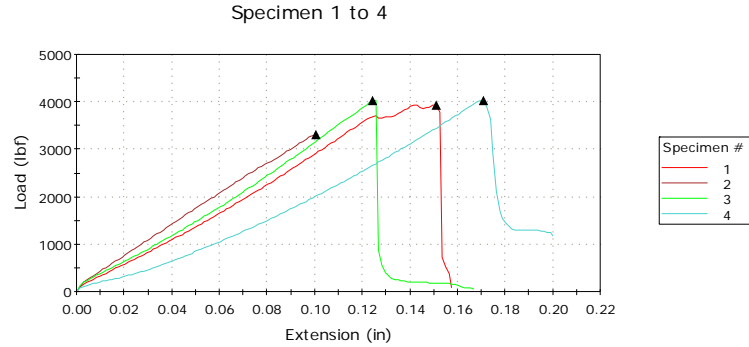
Specimen #	Embedment Length (in)	Maximum Load (lbf)	Extension at Maximum Load (in)
1	8	3938	0.15103
2	8	3309	0.10043
3	4	4029	0.12440
4	4	4026	0.17106

W/C: 0.50, 10-Days Test

28-DAY TESTS, 4-IN and 8-IN EMBEDMENT LENGTH, 252°F
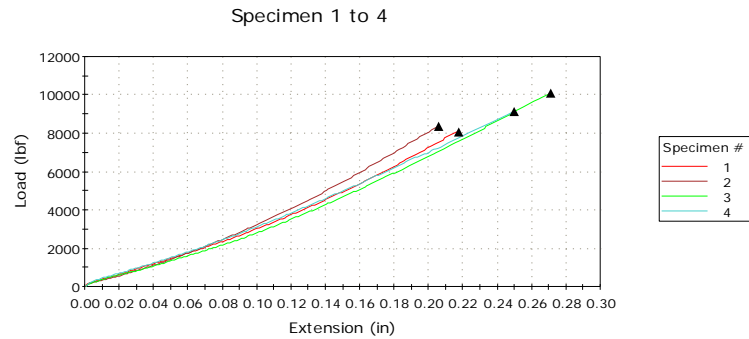
Specimen 1 to 4

Specimen #	Embedment Length (in)	Maximum Load (lbf)	Extension at Maximum Load (in)
1	8	8037	0.21772
2	8	8348	0.20573
3	4	10104	0.27108
4	4	9114	0.24973

W/C 0.40, 28 DAY TESTS

110
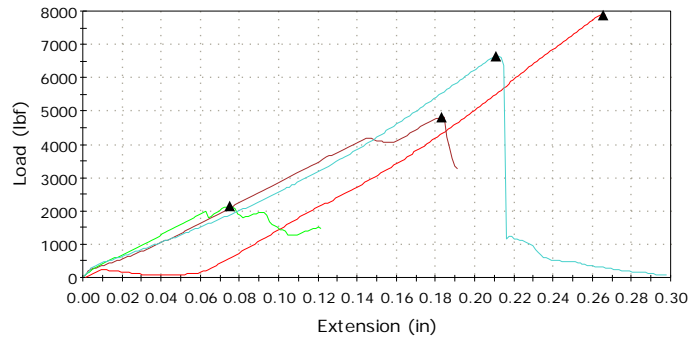
Specimen 1 to 4

Specimen #	Embedment Length (in)	Maximum Load (lbf)	Extension at Maximum Load (in)
1	8	7897	0.26525
2	8	4816	0.18303
3	3	2135	0.07510
4	4.5	6660	0.21106

W/C 0.45, 28- Day test

Specimen 1 to 4
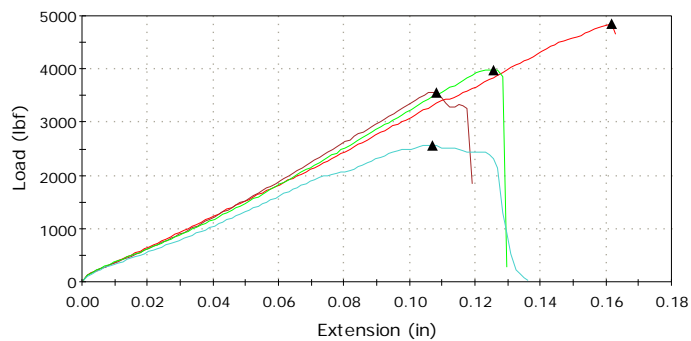
Specimen #	Embedment Length (in)	Maximum Load (lbf)	Extension at Maximum Load (in)
1	8	4848	0.16170
2	8	3569	0.10843
3	4	3989	0.12572
4	3.8	2571	0.10706

W/C 0.50, 28- Day test

APPENDIX B

CORRODED REBAR PULLOUT TEST GRAPHS

CORRODED REBAR 3 DAY PULLOUT TEST RESULTS

Specimen 1 to 8
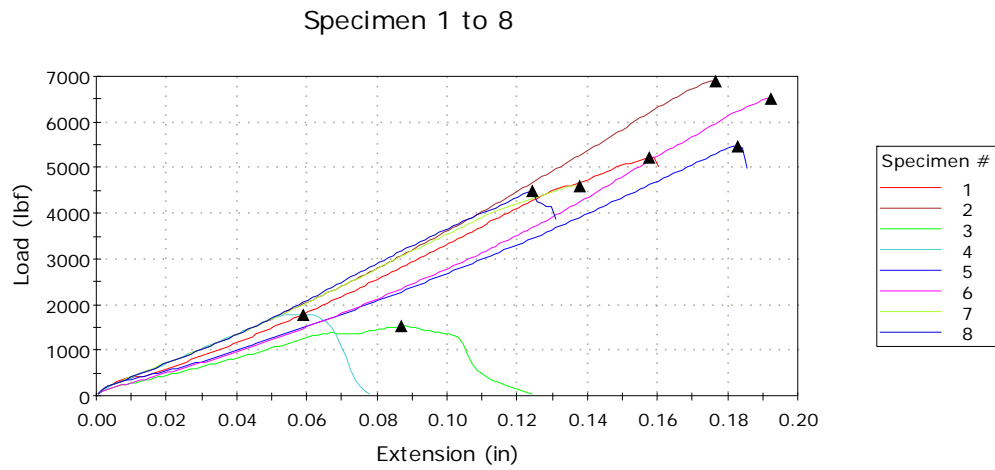
Specimen	W/C	Rebar Temperature (^{o}F)	Maximum Load (lbf)	Extension at Maximum Load (in)
1	0.40	14	5210	0.15770
2	0.40	14	6910	0.17646
3	0.50	77	1521	0.08710
4	0.50	77	1786	0.05904
5	0.40	77	5484	0.18306
6	0.40	77	6518	0.19241
7	0.40	252	4612	0.13773
8	0.40	252	4485	0.12446

Specimen 1 to 10
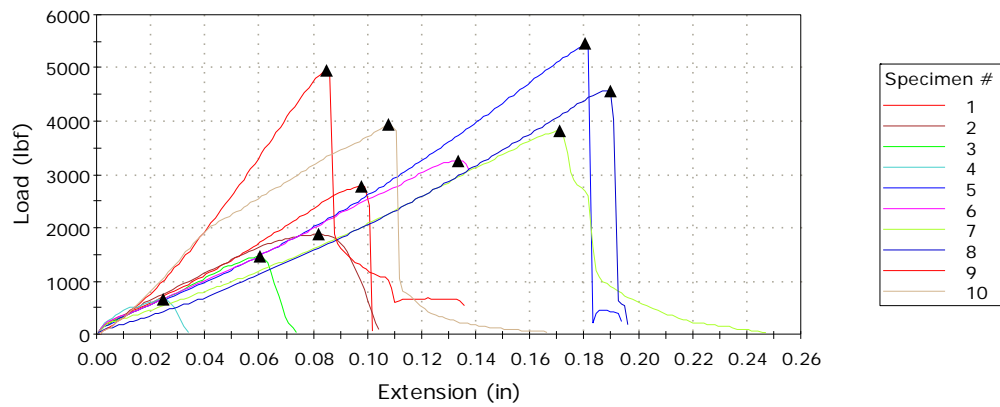
Specimen	W/C	Rebar Temperature (^{O}F)	Maximum Load (lbf)	Extension at Maximum Load (in)
1	0.50	14	2786	0.09776
2	0.50	14	1875	0.08172
3	0.50	252	1474	0.06042
4	0.50	252	651	0.02441
5	0.45	14	5449	0.18042
6	0.45	14	3261	0.13371
7	0.45	77	3828	0.17106
8	0.45	77	4579	0.18971
9	0.45	252	4953	0.08498
10	0.45	252	3927	0.10772

CORRODED REBAR 10 DAY PULLOUT TEST RESULTS

Pullout Test Results
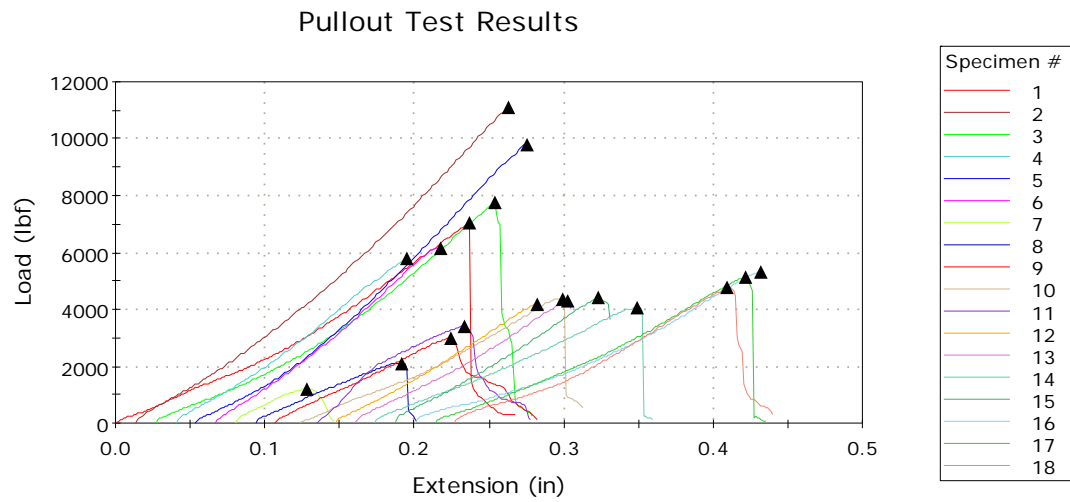
Specimen #	W/C	Rebar Temperature (^{O}F)	Maximum Load (lbf)	Extension at Maximum Load (in)
1	0.40	14	7022	0.236
2	0.40	14	11103	0.249
3	0.40	252	7744	0.227
4	0.40	252	5817	0.155
5	0.40	77	9809	0.221
6	0.40	77	6136	0.151
7	0.50	252	1190.	0.048
8	0.50	252	2118	0.097
9	0.50	77	2979	0.117
10	0.50	77	4373	0.179
11	0.50	14	3414	0.100
12	0.50	14	4179	0.135
13	0.45	252	4300	0.143
14	0.45	252	4069	0.176
15	0.45	77	4434	0.136
16	0.45	77	5339	0.232
17	0.45	14	5130	0.208
18	0.45	14	4751	0.183

CORRODED REBAR 28 DAY PULLOUT TEST RESULTS

Pullout Test Results
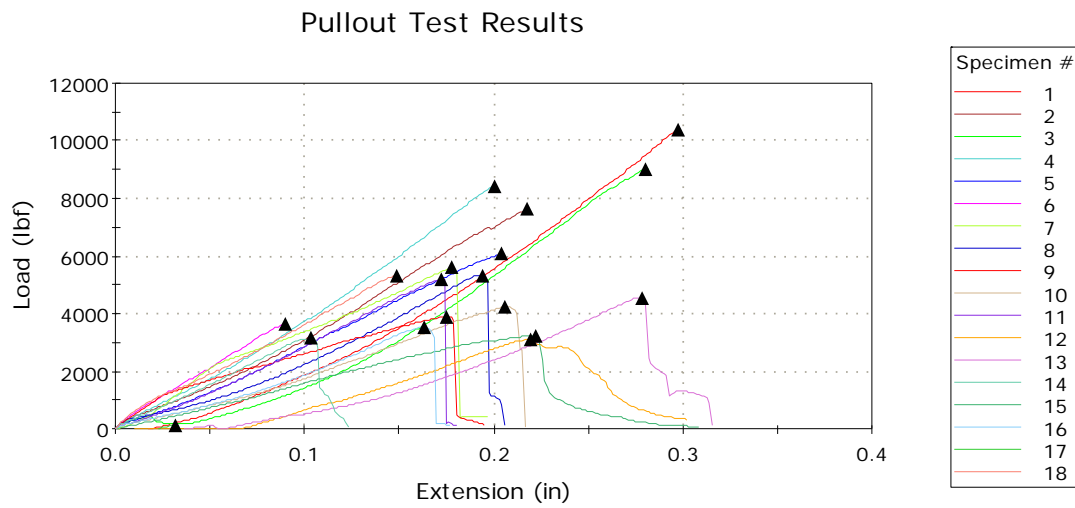
Specimen #	W/C	Rebar Temperature (^{O}F)	Maximum Load (lbf)	Extension at Maximum Load (in)
1	0.40	14	10367	0.29739
2	0.40	14	7616	0.21773
3	0.40	77	9044	0.28041
4	0.40	77	8432	0.20043
5	0.40	252	6067	0.20437
6	0.40	252	5342	0.14838
7	0.45	14	5586	0.17823
8	0.45	14	5336	0.19375
9	0.45	252	3873	0.17509
10	0.45	252	4230	0.20572
11	0.45	77	5191	0.17239
12	0.45	77	5133	0.18782
13	0.50	14	3097	0.21941
14	0.50	14	4550	0.27802
15	0.50	252	3136	0.10306
16	0.50	252	3219	0.22180
17	0.50	77	3540	0.16310
18	0.50	77	3643	0.08989

APPENDIX C

ESEM MICROGRAPHS FOR THE CORRODED REBAR TESTS AT 3-DAYS AND 10-

DAYS
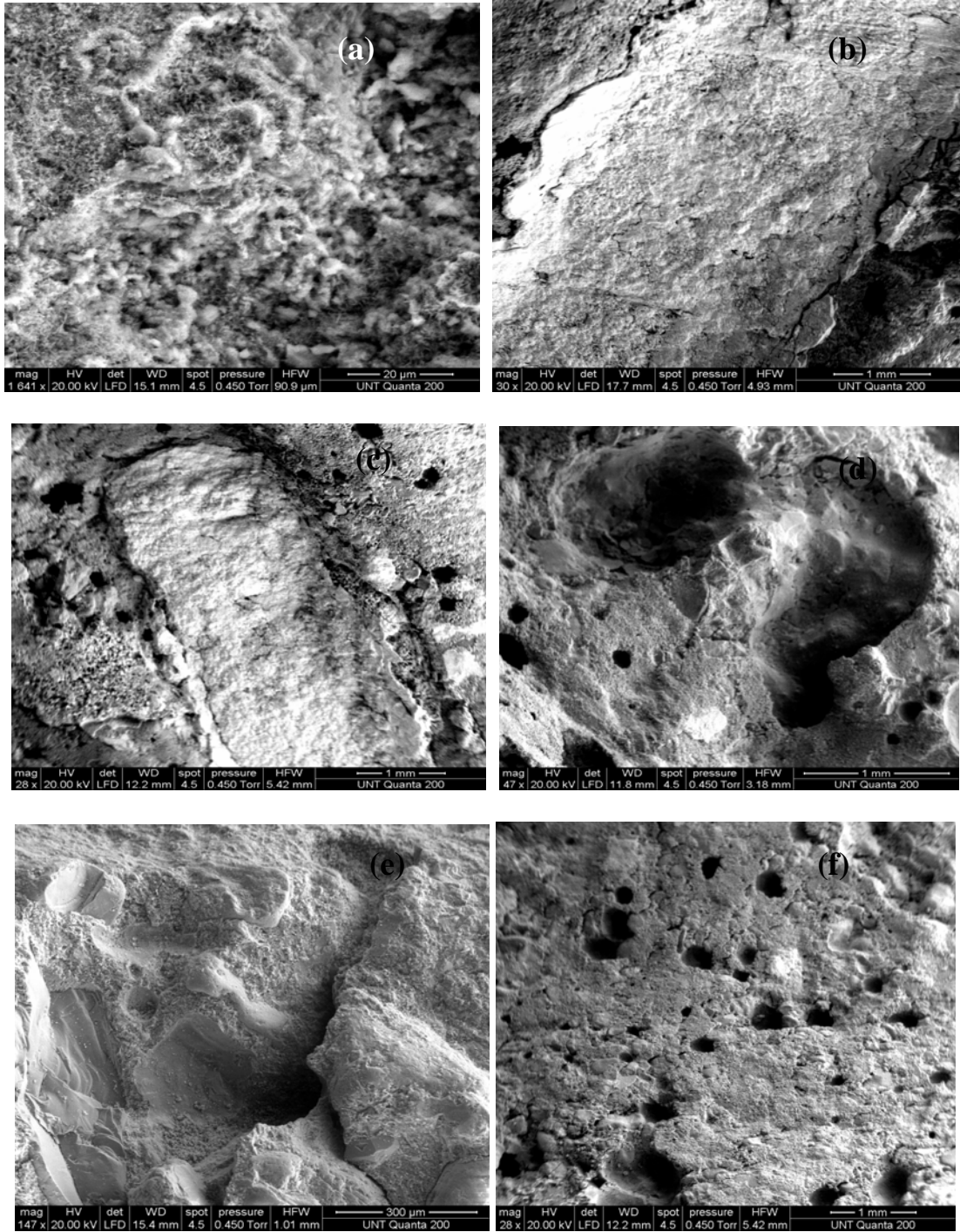
ESEM micrographs of the ITZ for corroded rebar steels at w/c 0.50 at 14°F after 3 days (a), 77°F after 3 days (b), 252°F after 3 days (c), 14°F after 10 days (d), 77°F after 10 days (e), 252°F after 10 days (f).
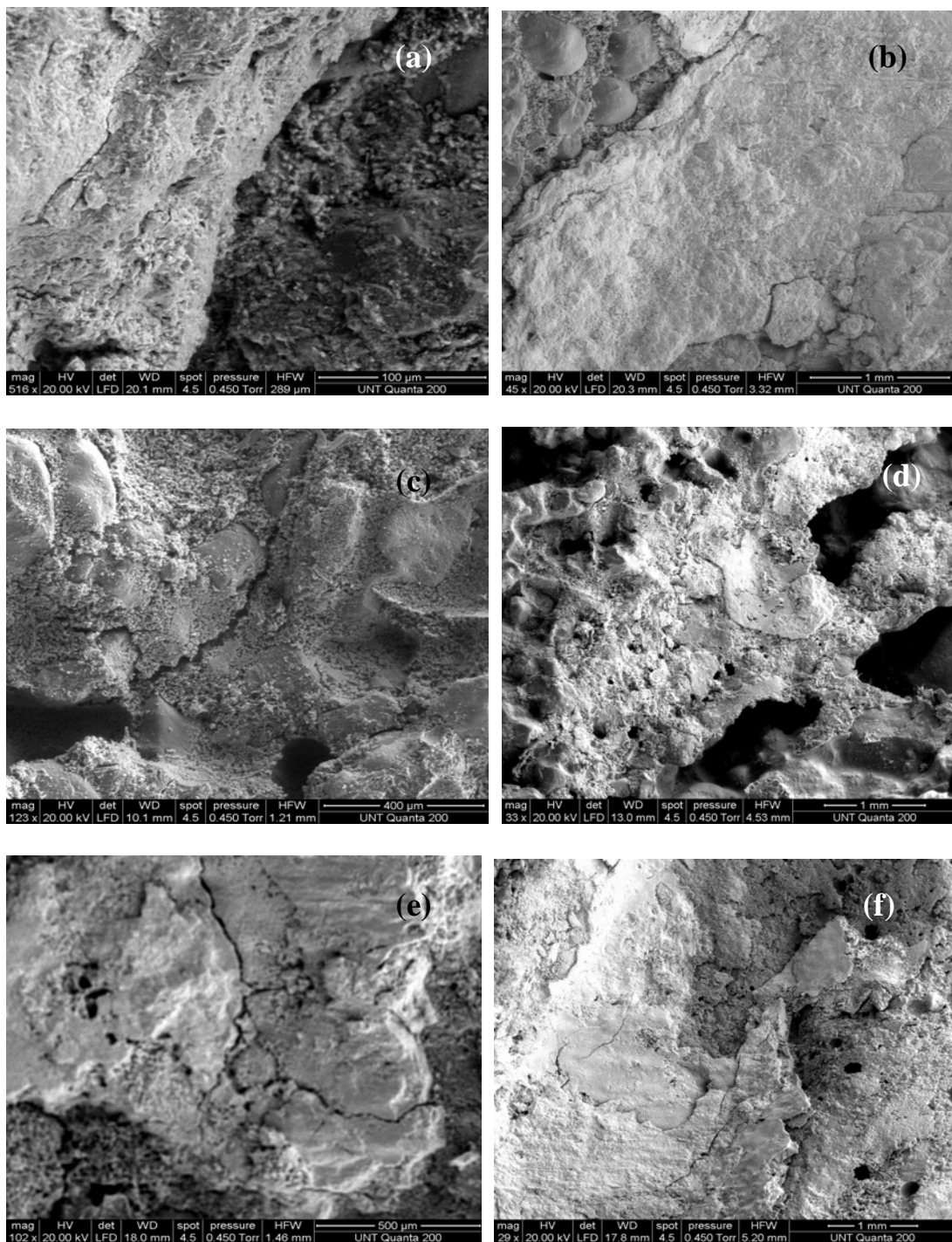
ESEM micrographs of the ITZ for corroded rebar steels at w/c 0.45 at 14°F after 3 days (a), 77°F after 3 days (b), 252°F after 3 days (c), 14°F after 10 days (d), 77°F after 10 days (e), 252°F after 10 days (f).
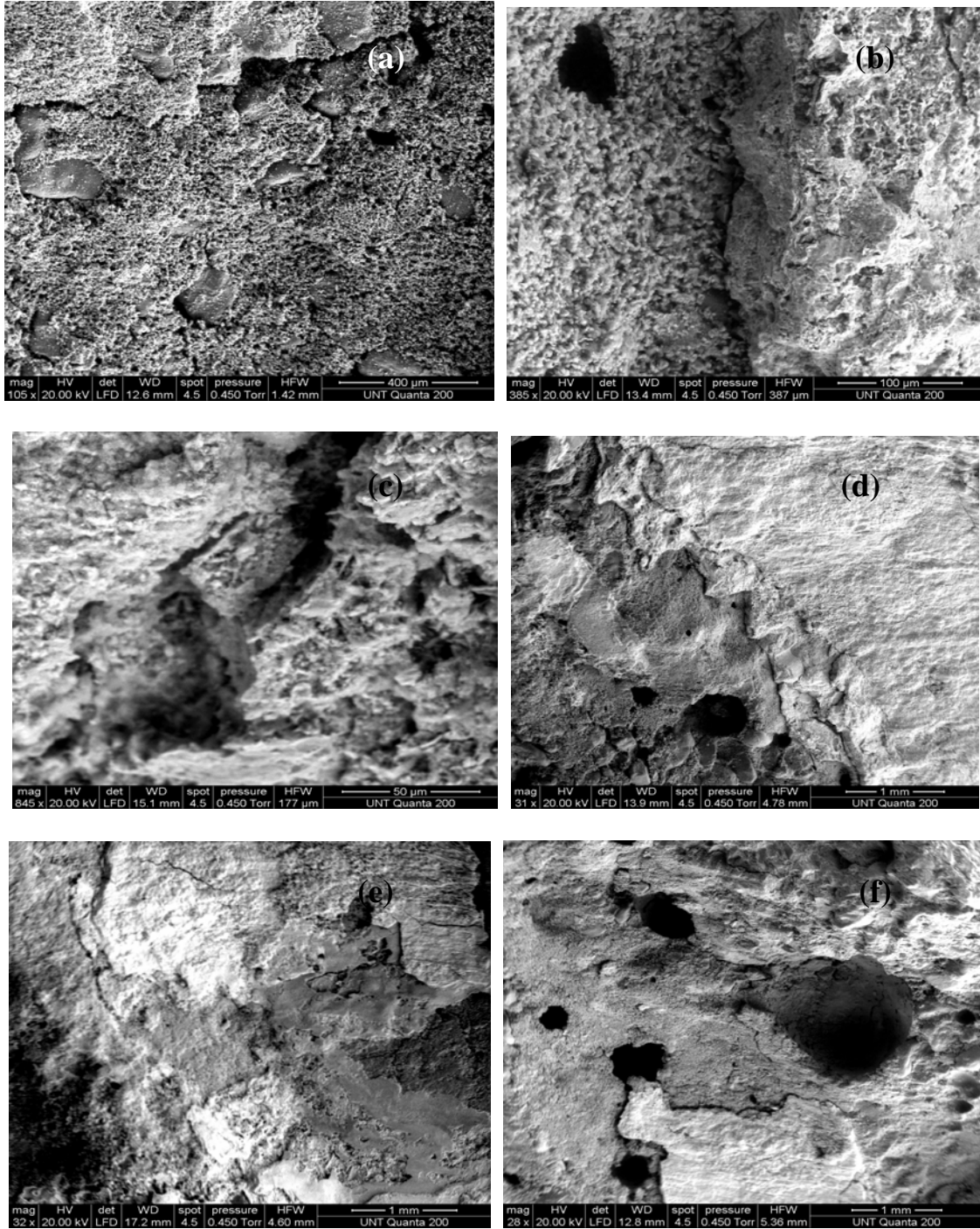
ESEM micrographs of the ITZ for corroded rebar steels at w/c 0.45 at 14°F after 3 days (a), 77°F after 3 days (b), 252°F after 3 days (c), 14°F after 10 days (d), 77°F after 10 days (e), 252°F after 10 days (f).

REFERENCES

Abbasi, Abdolkarim and Hogg, Paul J. (2005). Temperature and environmental effects on glass fiber rebar: Modulus, strength and interfacial bond strength with concrete. *Composites* 36: 394-404.

American Concrete Institute (ACI), (1999). *Aggregates for Concrete, ACI Education Bulletin E1-99*. Farmington Hills, MI: American Concrete Institute

American Society for Testing and Materials (ASTM) Standard (2001). *ASTM Standard C 192/C 192M-00: Standard Practice for Making and Curing Concrete Test Specimens in the Laboratory*. Pennsylvania: American Society for Testing and Materials.

American Society for Testing and Materials (ASTM) Standard (2001). *ASTM Standard C39/C 39M-01: Standard Test Method for compressive strength of cylindrical concrete specimens*. Pennsylvania: American Society for Testing and Materials.

American Society for Testing and Materials (ASTM) Standard (2001). *ASTM Standard A615: Standard Specification for Deformed and Plain Billet-Steel Bars for Concrete Reinforcement*. Pennsylvania: American Society for Testing and Materials.

Akcaoglu, Tulin Tokyay, Mustafa Celik, Tahir (2005). Assessing the ITZ microcracking via scanning electron microscope and its effect on the failure behavior of concrete. *Cement and Concrete Research* 35: 358-363.

Andrade, C. Merino, P. Novoa, X.R. Perez, M.C. Solar, L. (1995). Passivation of reinforcing steel in concrete. *Materials Science Forum* 192: 891-898.

Basheer, L. Basheer, P.A.M. Long, A.E. (2005). Influence of coarse aggregate on the permeation, durability and microstructure characteristics of ordinary Portland cement concrete. *Construction and Building Materials* 19: 682-690.

Batis, G. Rakanta, E. (2005). Corrosion of steel reinforcement due to atmospheric pollution. *Cement and Concrete Composites* 27: 269-275.

Bourdette, B. Ringot, E. Ollivier, J.P. (1995). Modeling of the transition zone porosity. *Cement and Concrete Research* 25 (4): 741-751.

Brundle, C.R., Evans, C.A., Jr. and Wilson, S. (1992). *Encyclopedia of Materials Characterization.* Greenwich, CT: Manning Publications.

Cha, S.W. (1999). *Modeling of Hydration Process and Analysis of Thermal and Hygral Stresses in Hardening Concrete*. PhD dissertation, Seoul National University, Seoul, Korea.

Chaallal, O. and Benmokrane, B. (1996) .Fiber-reinforced plastic rebars for concrete applications. *Composites* 27B : 245-252.

Cwirzen, Anderzej and Penttala, Vesa (2005). Aggregate-cement paste transition zone properties affecting the salt- frost damage of high performance concretes. *Cement and Concrete Research* 35: 671-679.

Diamond, Sidney (2001). Considerations in image analysis as applied to investigation of the ITZ in concrete. *Cement and Concrete Composites* 23: 71-178.

Diamond, Sidney and Huang, Jingdong (2001). The ITZ in concrete – a different view based on image analysis and SEM observations. *Cement and Concrete Composites* 23: 179-188.

Elfino, M., Ozyildirim, C., and Steele, R. (2001) *CRCP in Virginia, Lessons Learned.* Fifth International Conference on Concrete Pavement Design and Rehabilitation, Orlando, Florida, September 9-13 (pp. 451-465).

Fang Congqi, Lundgren Karin, Chen Liuguo, Zhu Chaoying, (2004). Corrosion influence on bond in reinforced concrete. *Cement and Concrete Research* 34: 2159-2167.

Giaccio, G. Rocco, Violini, C. D. Zappitelli, J. Zerbino, R. (1992). High strength concrete incorporating different coarse aggregates. *ACI Materials Journal* 89 (3): 242-246.

Huang, Y. H. (2004). *Pavement Analysis and Design.* Englewood Cliffs, NJ: Prentice Hall.

Hsu, T.T.C. Slate, F.O. Sturman, G.M. Winter, G. (1963). Microcracking of plain concrete and the shape of the stress – strain curve. *ACI Materials Journal* 60 (2): 209-224.

International Federation for Structural Concrete (2000). *Bond of reinforcement in concrete.* State of the art report, Bulletin No. 10, pp 188-215. Switzerland: International Federation for Structural Concrete.

Jeuffroy Georges and Sauterey Raymond (1996). *Cement and Concrete Pavements.* Brookfield, NJ: A.A. Balkema Publishers.

Katz, Amnon and Berman, Neta (2000). Modeling the effect of high temperature on the bond of FRP reinforcing bars to concrete. *Cement and Concrete Composites* 22: 433-443.

Kim, S. and Won, M. (2004). Horizontal cracking in continuously reinforced concrete pavements. *ACI Structural Journal* 784-791.

Kosmatka, S.H. and Panarese, W.C. (1988). *Design and Control of Concrete Mixtures* (13th ed.), Skokie, IL: Portland Cement Association.

Lianxiang Du, Elizabeth Lukefahr (2007). Summary of Thirty years of TxDOT-Funded Research on Coarse Aggregate Issues in Concrete Paving. *Proceedings of the 2007 Mid-Continent Transportation Research Symposium* Ames, Iowa.

Mehta, P.K. and Monteiro, P.J.M. (1993). *Concrete: Microstructure, Properties, and Materials* (2nd ed.). New York, NY: McGraw-Hill Companies, Inc.

Mindess, S., and Young, J.F. (1981). *Concrete*. Upper Saddle River, NJ: Prentice-Hall Inc.

Morinaga S. (1988). Prediction of service lives of corroded reinforced concrete buildings based on rate of corrosion of reinforcing steel. *Report No.23* Shimizu Corp, Japan: p.82.

Nam, Jeong-Hee (2005). *Early-age behavior of CRCP and its implications for long-term performance*. Thesis Dissertation, University of Texas.

Nemati, K.M. Monteiro, P.J.M (1998). A new method for studying stress-induced microcracks in concrete. *Journal of Materials in Civil Engineering* 10 (3): 128-134.

Prokopski, G. Halbiniak, J. (2000). Interfacial transition zone in cementitious materials. *Cement and Concrete Research* 30: 579-583.

Prokopski, G. Langier, B. (2000). Effect of water/cement ratio and silica fume addition on the fracture toughness and morphology of fractured surfaces of gravel. *Cement and Concrete Research* 30: 1427-1433.

Romagnoli, R. Batik, R.O. Vetere, V.F. Sota, J.D. Lucchini, I.T. Carbonari, R.O. (2002). The influence of the cement paste microstructure on corrosion and the adherence of reinforcing bars as a function of the water-cement ratio. *Anti-Corrosion Methods and Materials* 49 (1): 11-18

Samarai, M., Popovics, S., and Malhotra, V.M. (1983). Effect of high temperatures on the properties of hardened concrete. *Transportation Research Record No. 924* (pp 50-56). Washington, D.C: Transportation Research Board of the National Academies.

Seddelmeyer, J.D. Deshpande, P.G. Wheat, H.G. Fowler, D.W. Jirsa, J.O. (2000). Feasibility of various coatings for the protection of reinforcing steel – corrosion and bond testing. *Research Report* 4904.

Shah SP, Swartz SE, Ouyang C. (1995). *Fracture mechanics of concrete*. New York, NY: Wiley Interscience.

Shamsad, Ahmad, Al-Kutti, Walid A. Omar S. Baghabra Al-Amoudi, Mohammad Maslehuddin (2008). Compliance criteria for quality concrete. *Construction and Building Materials* 22: 1029-1036.

Simenow, P. Ahmad, S. (1999). Effect of transition zone on the elastic behavior of cement based composites. *Cement and Concrete Research* 29: 1019-1025.

Suh, Y.C., Hankins, K., and McCullough, B.F. (1992). Early-age behavior of continuously reinforced concrete pavement and calibration of the failure prediction model in the CRCP-7 Program. *Research Report 1244-3* Center for Transportation Research, University of Texas at Austin.

Tasong, W.A. Lynsdale C.J. and Cripps, J.C. (1998). Aggregate – Cement paste interface. II: Influence of aggregate physical properties. *Cement and Concrete Research* 28 (10): 1453-1465

Tasong, W.A Lynsdale, C.J. and Cripps, J.C. (1999). Aggregate – cement paste interface: Part I. Influence of aggregate geochemistry. *Cement and Concrete Research 29*: 1019-1025.

Texas Department of Transportation (2006). *Pavement Design Guide*. Austin, Texas: Texas Department of Transportation.

Tighiouart, B. Benmokrane, B. Gao, D. (1998). Investigation of bond in concrete member with fiber reinforced polymer bars, *Construction and Building Materials* 12: 453-462.

Tuuti K. (1980). Service life of structures with regard to corrosion of embedded steel. Performance of concrete in marine environment. *American Concrete Institute* 223-236.

Weyers RE. (1998). Service life model for concrete structures in chloride laden environments. *ACI Materials Journal* 95 (4): 445-453.

Zimbelman, R. (1985). A contribution to the problem of cement-aggregate bond. *Cement and Concrete Research* 15: 801-808.